NTNU – Trondheim
Norwegian University of
Science and Technology

Evaluation of predictive methods for wind turbine performance and wake development

Federico Bosio

Master's Thesis
Submission date: March 2014
Supervisor: Lars Sætran, EPT

Norwegian University of Science and Technology
Department of Energy and Process Engineering

NTNU
Norwegian University
of Science and Technology

Department of Energy
and Process Engineering

EPT-M-2013-152

MASTER THESIS

for

Student Federico Bosio

Autumn 2013

Evaluation of predictive methods for wind turbine performance and wake development
Vurdering av beregningsmetoder for vind-turbin ytelse og nedstrøms vake-utvikling

Background and objective

In a wind park the downwind wake from the rotor of an upstream wind turbine (WT) will be the incoming wind for a downwind WT. The wake from a WT contains less kinetic energy than the undisturbed wind field, and regains energy with increasing downstream distance through turbulent mixing of wake fluid with fluid from outside the wake. The mixing process takes time and distance, such that in the design of wind parks it is important to be able to predict the flow process through the WT rotor and the downstream development of the WT wakes – this in order to optimize the individual positioning of the WT wrt. maximum power output from the wind farm.

There exist both simple and complex prediction tools for the wind flow through a WT rotor and development of the WT wake – prediction tools that are used in the design and optimization of wind parks. Generally, the more complex prediction tools give more accurate predictions than the simple prediction tool – however, it is problematic to evaluate the accuracy of the prediction tools against measured full scale wind data due to limited number of measuring points (typically 1 met-mast with a few anemometers) and non-controllable boundary conditions with varying wind direction and non-stationary mean speed, varying temperature, humidity and pressure leading to changing atmospheric stability.

The following tasks are to be considered:

For this work we propose to implement Actuator Disk (with and without rotation) models for the WT rotor and calculate the WT wake using the "Open Source" computer software. For the evaluation of the results there exists a well documented experimental test case for a model WT (Krogstad and Eriksen, Ren. Energy 50 (2013) 325-333) and also another well documented test case for a so-called "Drag-disk" (Pierella and Saetran, 17th Australasian Fluid Mechanics Conference Auckland, New Zealand 5-9 December 2010) – we recommend that these cases are used for comparison and evaluation of the Actuator Disk models, and also with other theoretical models for the WT wake that the student might consider relevant.

Within 14 days of receiving the written text on the master thesis, the candidate shall submit a research plan for his project to the department.

When the thesis is evaluated, emphasis is put on processing of the results, and that they are presented in tabular and/or graphic form in a clear manner, and that they are analyzed carefully.

The thesis should be formulated as a research report with summary both in English and Norwegian, conclusion, literature references, table of contents etc. During the preparation of the text, the candidate should make an effort to produce a well-structured and easily readable report. In order to ease the evaluation of the thesis, it is important that the cross-references are correct. In the making of the report, strong emphasis should be placed on both a thorough discussion of the results and an orderly presentation.

The candidate is requested to initiate and keep close contact with his/her academic supervisor(s) throughout the working period. The candidate must follow the rules and regulations of NTNU as well as passive directions given by the Department of Energy and Process Engineering.

Risk assessment of the candidate's work shall be carried out according to the department's procedures. The risk assessment must be documented and included as part of the final report. Events related to the candidate's work adversely affecting the health, safety or security, must be documented and included as part of the final report. If the documentation on risk assessment represents a large number of pages, the full version is to be submitted electronically to the supervisor and an excerpt is included in the report.

Pursuant to "Regulations concerning the supplementary provisions to the technology study program/Master of Science" at NTNU §20, the Department reserves the permission to utilize all the results and data for teaching and research purposes as well as in future publications.

The final report is to be submitted digitally in DAIM. An executive summary of the thesis including title, student's name, supervisor's name, year, department name, and NTNU's logo and name, shall be submitted to the department as a separate pdf file. Based on an agreement with the supervisor, the final report and other material and documents may be given to the supervisor in digital format.

☐ Work to be done in lab (Water power lab, Fluids engineering lab, Thermal engineering lab)
☐ Field work

Department of Energy and Process Engineering, 14. February 2014

Olav Bolland
Department Head

Lars Sætran
Academic Supervisor

Research Advisor: Fabio Pierella

Abstract

In this project I have predicted the performance and the wake development for a model wind turbine using the actuator disc with Blade Elements Momentum (BEM) methods. The flow has been solved using OpenFOAM, an open-source CFD software, in combination with the $k-\varepsilon$ turbulent model. The results obtained have been compared with the experimental results from the wind tunnel. There is a good prediction in the wake velocity profiles whereas the kinetic turbulent energy is underestimated. Furthermore I have predicted the wake development with the simple actuator disc and with the Jensen model, methods computationally cheaper but less accurate. Finally the wind turbine models have been compared with the drag disc, a simple porous disc using for simulate the wind turbine wake. The actuator disc with BEM is fairly closer to the wind turbine than the drag disc.

Contents

List of Figures

Symbols and notations

a	Axial induction factor
a'	Tangential induction factor
A	Disk area
c	Chord length
Cl	Lift coefficient
Cd	Drag coefficient
Ct	Tangential force coefficient
Cn	Axial force coefficient
C_P	Power coefficient
C_T	Thrust coefficient
F_t	Tangential force per meter
F_n	Axial force per meter
H	Wind tunnel height
l	Turbulent length scale
$\dot{m}$	Mass flow rate
N	Number of blades
n	number of blade stations
p	Static pressure
P	Power
p_N	Force per length in tangential direction
p_T	Force per length in axial direction
r	Local radius
R	Tip radius
R_h	Hub radius
t	Thickness of the cylinder

λ_r	Local tip speed ratio
TSR	Tip speed ratio
Re	Reynolds number
T	Thrust force
U_∞	Velocity far away
U_{rel}	Relative velocity
W	Wind tunnel width
α	Angle of attack
ε	Turbulent dissipation
θ	Local pitch angle
θ_0	Blade pitch angle
θ_T	Local twist angle
k	Turbulent kinetic energy
μ_t	Eddy or turbulent viscosity
ν	Viscosity
ρ	Density
σ	Solidity of rotor
φ	Angle of the relative velocity
Ω	Angular velocity of the wind turbine rotor
ω	Angular velocity of the flow in the wake

1 Introduction

Focus of this project is to describe the wake of an horizontal axis wind turbine with a computational approach. Both industry and research have the interest to elaborate a tool which is able to predict the wake of wind turbines with reasonable accuracy and computational cost.

1.1 Historical review

Nowadays the wind energy is a topic of particular interest. In fact, wind energy is one of the oldest mechanical energy sources ever discovered. Since ancient times, the human being has taken advantage of wind energy. We know that windmills were already in use in the Greek civilization. The windmills had a big diffusion in Europe , in particular in Northern Europe, from 10^{th} or 11^{th} century. They were used for water pumping, grinding grain, sawing wood. The wind was the major energy source in Europe before the advent of industrial revolution, after which the energy from fossil fuels forced the other energy source off the market. The main advantage of fossil fuels is transportability. The water power resisted longer in the challenge against fossil fuels since some kind of transportability could be obtained by channels, although its use was significantly reduced. The wind power disappeared completely.

By the late 1960s, however, the wind energy came back as a significant source of energy. This is due to some main factors: first, because of a strong increase of the cost of fossil fuels, linked to the awareness that this energy source is not unlimited. Secondly, people started to acknowledge that many environmental problems were linked with the fuel combustion. The wind, on the other hand, is present everywhere and in many place his intensity permits an economically sustainable use. Another important role is played by the advances in technology which permitted the construction of more efficient wind turbines. These technologies were often developed in other fields and rearranged for the wind industry. Nevertheless, a much wider political action is needed in order to help the diffusion of this energy source. Important political support consists in economical help under the form of incentives to industries and funding to research, and in updating governmental regulations to allow the interconnection of wind turbines with the electrical networks (the discussion in this part was inspired by Manwell [1]).

1.2 Problem statement

Nowadays, wind turbines are arranged in large clusters. In the wind farm planning the wake effects are important, and they can account to up to 30% of a wind farm nominal energy production, as reported by Dahlberg [2]. Therefore, it is important to be able to predict the wake losses with an acceptable uncertainty, in order to make investments safer and more remunerative.

In the latest period, CFD methods have been used in order to simulate wind turbines in various flow conditions (different direction and intensity of the wind), and the most sophisticated CFD software are also able to take account of the terrain geometry .

Two options are basically possible when modeling the rotor of a wind turbine. The first is to completely resolve the blade geometry, including the boundary layer developing on the blade surface. The second is to model the rotor as a force field which induces the same momentum loss as the real turbine in the fluid flow.

The simplest of this second class of modelling approaches is the actuator disk model. In its basic version, the model is only able to reproduce an axial momentum deficit in the wake, but is not able to predict any wake rotation.

A more physically correct approach is to couple the actuator disc with a BEM model, where the force per annular rotor element is calculated from tabulated 2D airfoil data. The thrust and the tangential force, predicted with the BEM model, are the input data for a CFD software that it permits to analyze the flow around the wind turbine.

This model is able to simulate the wake rotation connected with the torque extraction by the spinning rotor. However this model is axisymmetric, hence the forces are independent of the blades position. These models can be coupled either with a steady or an unsteady flow model (steady in this work).

In a more complicated model, denominated actuator line, the blades are represented as rotating linear force field. This technique requires a considerably higher computational cost and it is inherently unsteady.

The purpose of this work is to integrate an actuator disc rotor model with BEM in a CFD solver. The chosen CFD software is the open-source OpenFOAM. The software is free of cost and the user has the possibility to implement custom models by editing the source files. In the latest OpenFOAM version (2.2.0) a library with a simple axial actuation disk model is present. Purpose of this work was to modify the library in order to couple a BEM code to the actuation disc implementation.

The results obtained from the computational approach were compared with experimental data from a model wind turbine (D=0.9 m). Wind tunnel experiments are performed in a controlled environment, therefore the inlet conditions are easily adjustable and the turbine operating conditions could be easily varied, depending on the desired test condition.

The experimental data used for comparison were acquired in 2011 at the NTNU-EPT wind tunnel, in order to organize the so-called Blind Test by Krogstad and Eriksen [3], a bench marking of state-of-the art numerical tools for the simulation of the performance and wake behind a model wind turbine.

2 Theory

As mentioned in the introduction, the core of the program is based on the actuator disk couple with a BEM approach. In this section we will give a description of the simple Actuator Disk model, required for a complete understanding of the BEM model. The model is explained in a similar fashion in different textbooks, and the following description is inspired mainly by Manwell [4], Burton [5], Martin [6].

2.1 Simple Actuator Disk (Momentum theory)

A simple one-dimensional model, but it is able, in first approximation, to simulate the power extracted from the wind by the wind turbine rotor. This model consists in modelling the wind turbine rotor as an ideal permeable disk, frictionless, inducing a pressure drop in the flow.

Let us consider a control volume, whose boundaries consist in the stream tube and in two cross-sections of this stream-tube far away from the disk, perpendicular to the main flow direction. There is no flow across the stream-tube, and the flow enters and exits from the control volume only across the two limiting cross-sections.

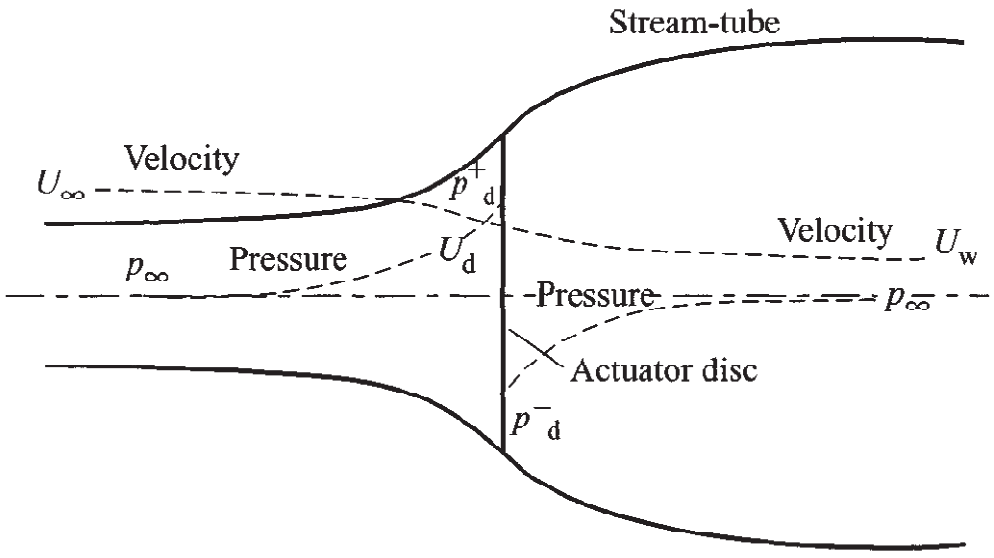

Fig.2.1 Stream-tube (Burton, T., Sharpe, D., Jenkins, N. and Bossanyi, E.(2001) Wind Energy Handbook. John Wiley & Sons, Ltd. page 43)

This model uses these assumptions (in addition to the assumption of the ideal disk):

- Incompressible fluid, $\rho = cost$
- Homogenous fluid
- Steady-state flow

According to the previous assumptions, the mass flow rate must be the same in all the cross-sections of the stream-tube:

$$\rho A_\infty U_\infty = \rho A U_d = \rho A_w U_w = \dot{m} \tag{2.1}$$

The subscript ∞ indicates the condition far away upstream, d indicates the conditions at the disk level, w indicates the conditions in the far wake.

It is common practice to introduce a, the axial flow induction factor, and to state the velocity at the disk as:

$$U_d = U_\infty(1-a) \tag{2.2}$$

If we consider the conservation of momentum law applied to the control volume:

$$T = U_\infty(\rho A U)_\infty - U_w(\rho A U)_w \tag{2.3}$$

T is the Thrust and is equal and opposite to the rate of change of momentum in the control volume; according to the mass conservation law we can write:

$$T = \dot{m}(U_\infty - U_w) \tag{2.4}$$

Or

$$T = \rho A U_d(U_\infty - U_w) = \rho A U_\infty(1-a)(U_\infty - U_w) \tag{2.5}$$

The Thrust is also expressed as the pressure difference across the actuator disk:

$$T = (p_d^+ - p_d^-)A \tag{2.6}$$

The two values of pressure across the disk are unknown but according to the assumption we can apply the Bernoulli's equation to express this pressure difference by means of other variables.

Applying the Bernoulli equation to the upstream section:

$$p_\infty + \frac{1}{2}\rho U_\infty^2 = p_d^+ + \frac{1}{2}\rho U_d^2 \tag{2.7}$$

While, for the upstream section:

$$p_d^- + \frac{1}{2}\rho U_d^2 = p_\infty + \frac{1}{2}\rho U_w^2 \tag{2.8}$$

Since the flow is unbounded, we assume that the pressure far downstream reaches the same value it had far upstream from the disc.

Hence the difference of pressure across the disk can be expressed as:

$$(p_d^+ - p_d^-) = \frac{1}{2}\rho(U_\infty^2 - U_w^2) \tag{2.9}$$

Solving equation (2.6) with equation (2.9), we obtain:

$$T = \frac{1}{2}\rho A(U_\infty^2 - U_w^2) \tag{2.10}$$

Equating the thrust from equation (2.5) and from equation (2.10), we obtain:

$$\rho A U_\infty (1-a)(U_\infty - U_w) = \frac{1}{2}\rho A(U_\infty^2 - U_w^2) \tag{2.11}$$

Solving equation (2.11) we obtain:

$$U_w = U_\infty(1-2a) \tag{2.12}$$

Now we can express the thrust only by the upstream variables and by the axial induction factor:

$$T = 2\rho A U_\infty^2 a(1-a) \tag{2.13}$$

The thrust is characterized by a non-dimensional thrust coefficient C_T:

$$C_T = \frac{T}{\frac{1}{2}\rho A U_\infty^2} \tag{2.14}$$

$$C_T = 4a(1-a) \tag{2.15}$$

Analyzing the trend of C_T we find that the maximum of C_T occurs for $a = \frac{1}{2}$; this means $U_w = 0$ as from equation (2.12). For $a > \frac{1}{2}$, U_w becomes negative: above this value the theory breaks down, and can be applied only via an empirical correction.

Furthermore we can evaluate the power extracted from the air flow:

$$P = TU_d = 2\rho A U_\infty^3 a(1-a)^2 \tag{2.16}$$

As for the thrust we can define a non-dimensional coefficient for the power: power coefficient C_P:

$$C_P = \frac{P}{\frac{1}{2}\rho A U_\infty^3} \tag{2.17}$$

$$C_P = 4a(1-a)^2 \tag{2.18}$$

From the analysis of the power coefficient expression, we find that the maximum value of C_P, known as the Betz limit, is $C_{P,max} = \frac{16}{27} = 0.593$ and occurs for $a = \frac{1}{3}$. The Betz limit is the maximum theoretically possible C_P, while in practice we always lower C_P values.

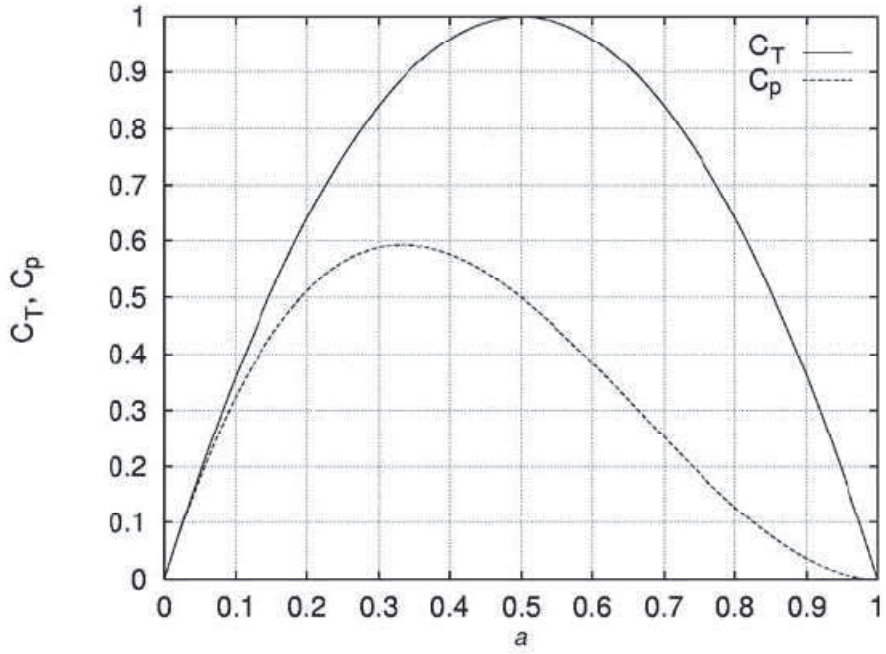

Fig.2.2 Variation of power and thrust coefficients in function of axial induction factor (Martin O. L. Hansen (2008) Aerodynamics of Wind Turbines, Second Edition. Earthscan. page 32)

2.2 Wake rotation

The previous analysis assumes only axial momentum loss, meaning that the wake is not rotating. This implies that we do not take into account the kinetic energy lost to impart a rotation to the fluid, leading to a performance overestimation. We can extend this theory taking into account the wake rotation. The flow behind the wind turbine rotates because it receives, as a reaction, the same torque the rotor experiences, but in the opposite direction. In this analysis it is assumed that the free stream flow is not rotating, while after flowing through the disk the flow has a constant rotation which does not evolve in the wake. All the rotation is given to flow across the disk. For a correct analysis, three new variables are introduced:

ω is the angular velocity of the flow in the wake

Ω is the angular velocity of the wind turbine rotor

a' is the tangential induction factor, it is defined as:

$$a' = \omega/2\Omega$$

Furthermore, we consider an annular stream tube that, at the disk, is characterized by a radius r and by a thickness dr. Therefore, all the variables are a function of the local radius, which allows the axial induction factor a and the tangential induction factor a' to vary across the rotor. The cross section area of the annular stream tube is equal to $2\pi r dr$.

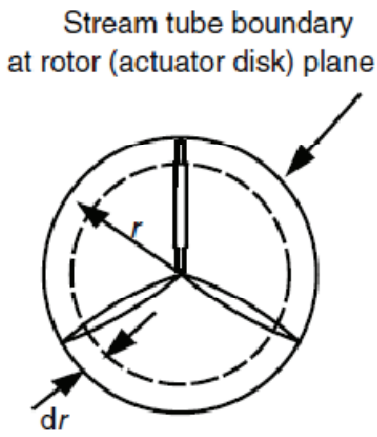

Fig.2.3 Annular stream tube (Manwell, J. F., McGowan, J. G. and Rogers, A. L. (2009) Wind Energy Explained: Theory, Design and Application, Second Edition. John Wiley & Sons, Ltd. page 97)

Expression (2.13) can be extended at the case with rotation with the only difference that the area is differential so also the thrust is differential:

$$dT = 2a(1-a)\rho U_\infty^2 dA = 2a(1-a)\rho U_\infty^2 2\pi r dr \tag{2.19}$$

We can also obtain a relation for the thrust acting on an annular element dT, by considering a control volume that rotates with the same angular velocity of the blades. For a reference system moving with the blades the difference of pressure across the disk is equal to difference of kinetic energy across the disk, so we can write:

$$(p_d^+ - p_d^-) = \rho(\Omega - \frac{1}{2}\omega)\omega r^2 \tag{2.20}$$

Since the flow, when flowing through the disc, suffers an increase in its relative rotational speed from Ω to $\Omega + \omega$, the dT can be expressed as:

$$dT = (p_d^+ - p_d^-)dA = \rho(\Omega - \frac{1}{2}\omega)\omega r^2 2\pi r dr \tag{2.21}$$

Using the tangential induction factor we have:

$$dT = 2a'(1-a')\rho\Omega^2 r^2 2\pi r dr \tag{2.22}$$

Equaling the expression (2.19) and (2.22) we obtain:

$$\frac{a(1-a)}{a'(1+a')} = \frac{\Omega^2 r^2}{U_\infty^2} = \lambda_r^2 \tag{2.23}$$

Where λ_r is the local speed ratio. In this expression the two induction factors and the radius are linked together, so for a fixed radius a and a' are dependent on each other.

By taking the wake rotation into account, we can also evaluate the torque. Applying the conservation of angular momentum we obtain the torque due to the infinitesimal annular cross section area:

$$dQ = d\dot{m}\, wr\, r = 2a'(1-a)\rho U_\infty \Omega r^2 2\pi r dr \tag{2.24}$$

By knowing the torque, it is easy to obtain the relation for the power extracted from the flow:

$$dP = \Omega dQ \tag{2.25}$$

Substituting dQ in (2.25), expressing a' in function of a and λ_r, and finally integrating along the radius we can obtain the power extracted in function of a. With mathematical analysis we can evaluate the distribution of a that permits to achieve the maximum value of the power coefficient.

An important parameter for the wind turbine is the tip speed ratio TSR, defined as:

$$TSR = \Omega R/U \tag{2.26}$$

Where R is the tip radius. This parameter has a relevant influence on the behavior of machine, and physically it indicates how fast the turbine is rotating with respect to the incoming flow. We can estimated the $C_{P,max}$ in function of TSR, see Fig.2.4.

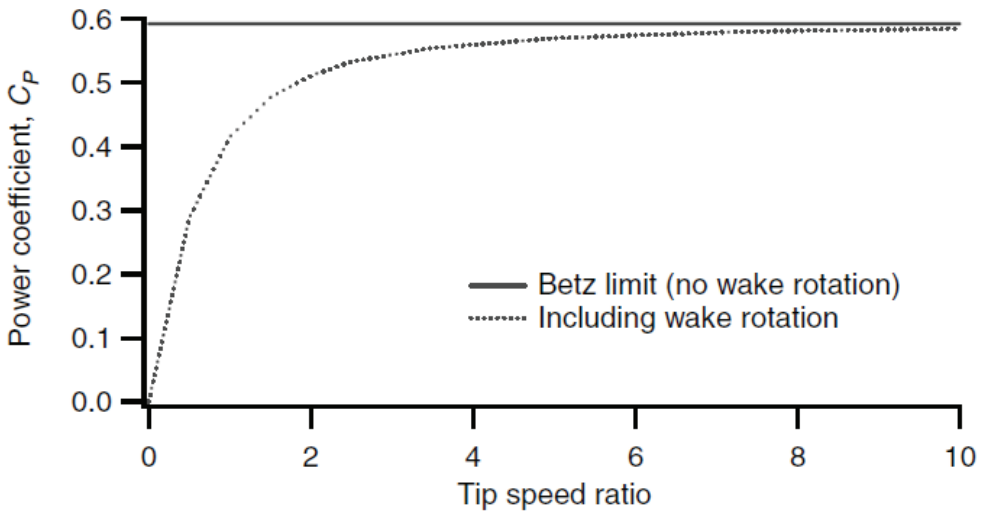

Fig.2.4 Maximum power coefficient in function of tip speed ratio (Manwell, J. F., McGowan, J. G. and Rogers, A. L. (2009) Wind Energy Explained: Theory, Design and Application, Second Edition. John Wiley & Sons, Ltd, page 100)

From Fig.2.4 we can notice that there is a strong influence of TSR and the Betz limit represent the asymptote value.

2.3 Blade Element Momentum (BEM) theory

This theory permits to evaluate the steady load acting on the blades and to consequently estimate the thrust, the torque and the power for different wind conditions and angular

velocities of the rotor, only by knowing the geometry of the blades. The BEM theory is a steady model, hence it is not possible provide the load fluctuation due to the blades position. This method uses annular stream tube as the momentum theory, but the ring thickness is finite; Applying the conservation of momentum we have seen that we can express the thrust dT (2.19) and the torque dQ (2.24), acting on the annular tube, as a function of the induction factors. An optimization analysis can evaluate which airfoil distribution along the radius allows to obtain the maximum power coefficient, but it is not possible evaluate the performance of a generic rotor working in generic condition because we don't know the induction factors distribution. The BEM model adds information about the geometry and also estimate the dT and the dQ with an aerodynamic analysis of the blade elements that sweep out the annular ring. Equating the dT and the dQ obtained via an aerodynamic analysis with those obtained via momentum analysis we can estimate the induction factors. This is an iterative process that converges when the induction factor does not change over successive iterations.

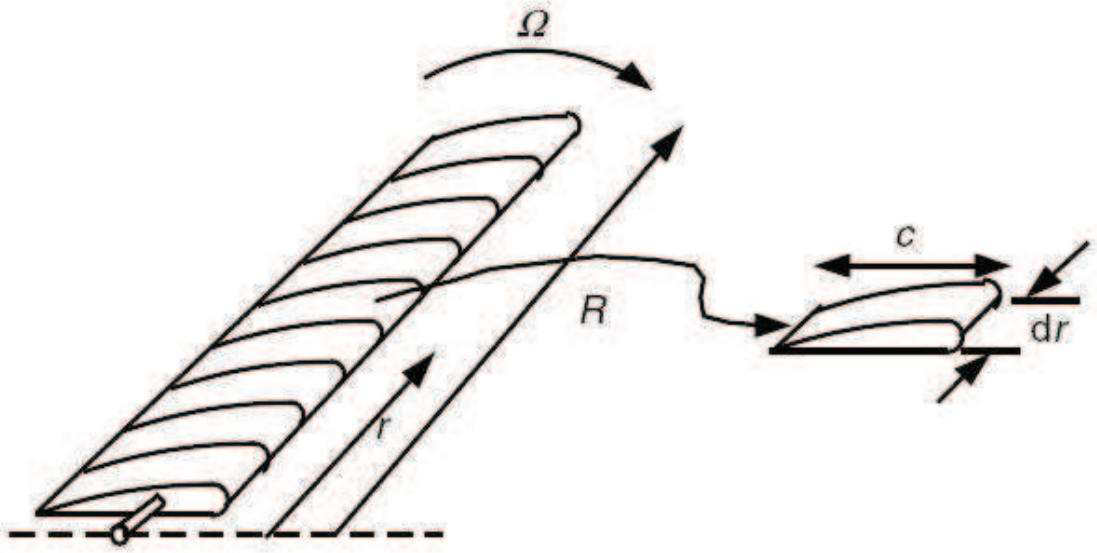

Fig 2.5 Blade elements (Manwell, J. F., McGowan, J. G. and Rogers, A. L. (2009) Wind Energy Explained: Theory, Design and Application, Second Edition. John Wiley & Sons, Ltd. page 119)

This model is based on these assumptions:

- There is not radial dependency, so every element does not influence other elements and it is not influenced by other elements
- The force acting on the blade element is spread on the annular ring swept out by the element

The force acting on the profile is the vector sum of lift, the force perpendicular to the relative velocity and drag, the force parallel to the relative velocity. The relative velocity is the vector sum of the axial velocity $U_\infty(1-a)$, at the disk level, and the tangential force $\Omega r(1+a')$, composed by the velocity of the blade element and the induced angular velocity.

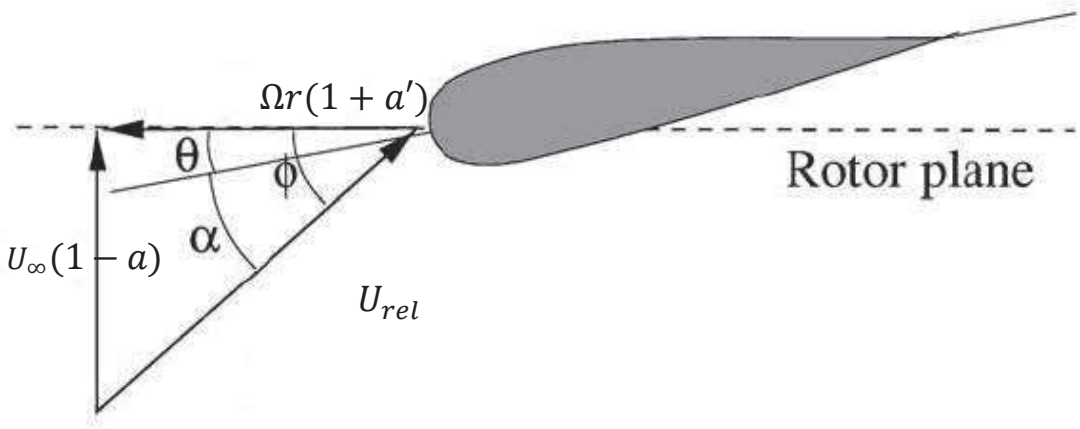

Fig 2.6 Velocities and angles at rotor plane (Martin O. L. Hansen (2008) Aerodynamics of Wind Turbines, Second Edition. Earthscan. page 47)

In the figure we can observe the velocities and the angles. The angle θ is the local pitch angle, defined as the sum between the blade pitch angle θ_0 and the local twist angle θ_T. φ is the angle between the rotor plane and the relative velocity. The angle of attack α is given by:

$$\alpha = \varphi - \theta \tag{2.27}$$

From the picture is easy to link the φ angle with the velocities:

$$\tan\varphi = \frac{(1-a)U_\infty}{(1+a')\Omega r} \tag{2.28}$$

$$U_{rel}\sin\varphi = (1-a)U_\infty \tag{2.29}$$

$$U_{rel}\cos\varphi = (1+a')\Omega r \tag{2.30}$$

The lift L and the drag D (force per length) can be evaluated with this expression:

$$L = \frac{1}{2}\rho U_{rel}^2 c C_l \tag{2.31}$$

$$D = \frac{1}{2}\rho U_{rel}^2 c C_d \tag{2.32}$$

Where C_l is the lift coefficient and C_d is the drag coefficient. Both are function of the angle of attack.

We can project the parallel and perpendicular forces to the rotor plane:

$$p_N = L\ \cos\varphi + D\ \sin\varphi \tag{2.33}$$

$$p_T = L\ \sin\varphi - D\ \cos\varphi \tag{2.34}$$

If we can express p_N and p_T as:

$$p_N = \frac{1}{2}\rho U_{rel}^2 c C_n \tag{2.35}$$

$$p_T = \frac{1}{2}\rho U_{rel}^2 c C_t \tag{2.36}$$

And then, if we divided (2.33) and (2.34) for $\frac{1}{2}\rho U_{rel}^2 c$ we obtain:

$$C_n = C_l \cos\varphi + C_d \sin\varphi \tag{2.37}$$

$$C_t = C_l \sin\varphi - C_d \cos\varphi \tag{2.38}$$

Knowing p_N and p_T we can evaluate the thrust dT and the torque dQ acting on this ring:

$$dT = N p_N dr \tag{2.39}$$

$$dQ = r N p_T dr \tag{2.40}$$

Equating the equation (2.39) with (2.19), we can find an expression for a:

$$a = \frac{1}{\frac{4\sin^2\varphi}{\sigma C_n} + 1} \tag{2.41}$$

Equating the equation (2.40) with (2.24), we can find an expression for a':

$$a' = \frac{1}{\frac{4\sin\varphi\cos\varphi}{\sigma C_t} - 1} \tag{2.42}$$

Where $\sigma$is the solidity and it's defined as:

$$\sigma(r) = \frac{c(r)N}{2\pi r} \tag{2.43}$$

The BEM algorithm consist in:

1. Give a guess value to a and to a'
2. Compute φ with equation (2.28)
3. Compute α with equation (2.27)
4. Compute C_l and C_d (usually they are read from table)
5. Compute C_n and C_t with equations (2.37) and (2.38)
6. Compute a and a' with equations (2.42) and (2.43)
7. Compare the new values of a and a' with those of previous iteration, if the difference is greater than the admissible tolerance it's need to return to point 2
8. Compute the thrust and the torque acting on the ring with the equation (2.39) and (2.40)

This algorithm must be applied for all the annular rings in order to obtain the total thrust T and the total torque Q. Knowing the torque we can calculate the power:

$$P = Q\Omega \tag{2.44}$$

In the end we can evaluate thrust and power coefficient with equations (2.14) and (2.17).

2.3.1 Tip loss factor

The difference of pressure between the two disk faces induces a flow around the tip. The effect is a lift and drag reduction. This effect is very strong on the tip, while it decreases closer to the rotor center. Furthermore, this effect is more important if the number of blades is lower. There are many methods to take this effect into account. In the current work, the Prandtl's tip loss factor correction was used. This method consist to modify the equation (2.19) and (2.24) including a correction factor F:

$$dT = 2a(1-a)\rho U_\infty^2 F 2\pi r dr \tag{2.45}$$

And:

$$dQ = 2a'(1-a)\rho U_\infty \Omega r^2 F 2\pi r dr \tag{2.46}$$

Where F is calculated as:

$$F = \frac{2}{\pi}\cos^{-1}\left[\exp\left(-\frac{N\,(R-1)}{2r\sin\varphi}\right)\right] \tag{2.47}$$

The change of equation (2.19) and (2.24) implies the change of the expressions (2.41) and (2.42) in:

$$a = \frac{1}{\frac{4F\sin^2\varphi}{\sigma C_n} + 1} \tag{2.48}$$

And:

$$a' = \frac{1}{\frac{4F\sin\varphi\cos\varphi}{\sigma C_t} - 1} \tag{2.49}$$

Hence, in the BEM algorithm ,we must use expressions (2.48) and (2.49) instead of (2.41) and (2.42).

2.3.2 High value of a

As we have previously observed, the momentum theory is unable to predict the behavior of a wind turbine for large value of axial induction factor. Many empiric models exist, which describe the thrust coefficient C_T as a function of a, for high values of the axial induction. Probably one of the most famous is the method by Glauert:

$$C_T = 4a(1-a)F \qquad a \leq \frac{1}{3} \tag{2.50}$$

$$C_T = 4a\left[1 - \frac{1}{4}(5-3a)a\right]F \qquad a \geq \frac{1}{3} \tag{2.51}$$

However, in this work, the method illustrated by Martin [7] was used:

$$C_T = 4a(1-a)F \qquad \text{If } a \leq a_c \tag{2.53}$$

$$C_T = 4[{a_c}^2 + (1-2a_c)a]F \qquad \text{If } a \geq a_c \tag{2.54}$$

Where a_c assumes the value of 0.2. This implies that the expression (2.48) is modified as follows:

If $a \leq a_c$

$$a = \frac{1}{\frac{4F\sin^2\varphi}{\sigma C_n} + 1} \tag{2.55}$$

If $a \geq a_c$

$$a = \frac{1}{2}\left[2 + K(1-2a_c) - \sqrt{(K(1-2a_c)^2 + 4(K{a_c}^2 - 1)}\right] \tag{2.56}$$

Where:

$$K = \frac{F\sin^2\varphi}{\sigma C_n} \tag{2.57}$$

Therefore, in the BEM algorithm we must use expression (2.48) instead of (2.41) to evaluate a and if $a \geq a_c$ recalculate a via expression (2.56).

2.4 Turbulence

From experimental observations we know that the flow behind a wind turbine is turbulent, exception made for the region right behind the rotor disk, characterized by an ordered vortex structure. The actuator disk model is not able to correctly represent the vortex structure behind a wind turbine, since the axisymmetric model cannot reproduce the tip vortices shed by the blade extremities. For this reason, the flow will be always

treated as turbulent, and we do not expect the actuator disc to output very precise predictions close to the turbine disk. Further downstream, after the vortex structure breakdown, the accuracy of the model increases.

For this reason, the CFD solver must be couple with a turbulence model. In this section, we will give a simple description of the turbulence closure problem, with particular attention to the $k-\varepsilon$ model, which was employed for our calculations. The description is based on the text book by Versteeg [8].

A turbulent flow is characterized by a high value of Reynolds number. The laminar flow pattern breaks down into a more chaotic flow, intrinsically unsteady, which means that the flow proprieties (velocity and pressure for an incompressible flow) vary in a random way. The turbulent flow is dominated by turbulent vortices, the so called "eddies", whose size span covers a wide range of length scales. The largest eddies extract energy from the mean flow (this is called vortex stretching), then the energy is transmitted down to progressively smaller and smaller eddy, finally the smallest eddies dissipate energy for viscous action, and convert kinetic energy into thermal energy. This mechanism is called energy cascade. The smallest scale (called Kolmogorov scale) is characterized by Reynolds number equal to 1. The presence of eddies of different scales, that interacts with each other, improve the heat, mass and momentum exchange and induce a better mixing.

Since turbulence is a random process we can use a statistical approach. Following the Reynolds decomposition, we can decompose the flow proprieties in two parts: a steady mean value and a fluctuating value:

$$\boldsymbol{u} = \boldsymbol{U} + \boldsymbol{u}'$$

$$p = P + p'$$

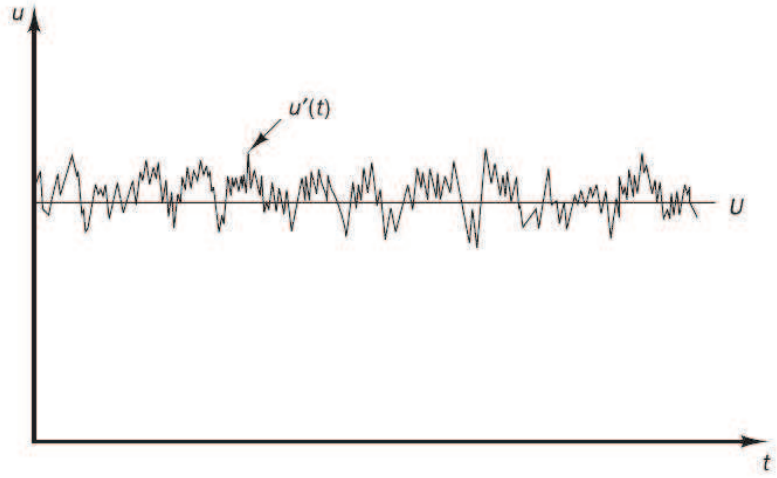

Fig.2.7 example of u profile in a turbulent flow (Versteeg, H K and Malalasekera, W (2007) An Introduction to Computational Fluid Dynamics, the finite volume method, Second Edition. Pearson Education Limited)

If we substitute, in the conservation equation, the decomposed flow proprieties we obtain the Reynolds-averaged Navier-Stokes equations:

$$div\,\boldsymbol{U} = 0 \tag{2.58}$$

$$\frac{\partial U}{\partial t} + div\,(U\boldsymbol{U}) = -\frac{1}{\rho}\frac{\partial P}{\partial x} + div\left(grad(V)\right) + \frac{1}{\rho}\left[\frac{\partial(-\rho\overline{u'^2})}{\partial x} + \frac{\partial(-\rho\overline{u'v'})}{\partial y} + \frac{\partial(-\rho\overline{u'w'})}{\partial z}\right] \tag{2.59}$$

$$\frac{\partial V}{\partial t} + div\,(V\boldsymbol{U}) = -\frac{1}{\rho}\frac{\partial P}{\partial y} + div\left(grad(V)\right) + \frac{1}{\rho}\left[\frac{\partial(-\rho\overline{u'v'})}{\partial x} + \frac{\partial(-\rho\overline{v'^2})}{\partial y} + \frac{\partial(-\rho\overline{v'w'})}{\partial z}\right] \tag{2.60}$$

$$\frac{\partial W}{\partial t} + div\,(W\boldsymbol{U}) = -\frac{1}{\rho}\frac{\partial P}{\partial z} + div\left(grad(V)\right) + \frac{1}{\rho}\left[\frac{\partial(-\rho\overline{w'v'})}{\partial x} + \frac{\partial(-\rho\overline{w'v'})}{\partial y} + \frac{\partial(-\rho\overline{w'^2})}{\partial z}\right] \tag{2.61}$$

The structure of these equations is very similar to the Navier-Stokes equation but the three momentum equations have extra terms, depending on the product of the fluctuating velocities. These terms are called Reynolds stresses, and represent the average momentum flux due to the turbulent velocity fluctuations:

$$\tau_{ij} = -\rho\overline{u'_\iota u'_j}$$

The methods that are based on the averaged Reynolds Equations are called RANS. The aim of these methods is to describe the flow by the resolution of a mean equation, which is, as we have seen, dependent on the turbulent part. This approach is especially appropriate for our problem, which will be treated as steady. As previously noted, equations (2.59), (2.60), (2.61) introduce new unknown turbulent terms, which have to be modeled. The task of modeling the turbulent quantities is denominated "turbulence closure" problem.

Most turbulence closure methods are based on the analogy between the viscous stress and the Reynolds stress. The Boussinesq assumption states that:

$$\tau_{ij} = \mu_t\left(\frac{\partial U_i}{\partial x_j} + \frac{\partial U_j}{\partial x_i}\right) - \frac{2}{3}\rho k\delta_{ij} \tag{2.62}$$

Where μ_t is the eddy viscosity and k is the turbulent kinetic energy and it's defined as:

$$k = \frac{1}{2}\left(\overline{u'^2} + \overline{v'^2} + \overline{w'^2}\right) \tag{2.63}$$

In other words, equation (2.62) states that the turbulent stresses are directly proportional to the gradient of the mean flow. With the additional assumption that the turbulent viscosity is isotropic, our system has got four equation and six unknowns. One of the most famous and validated model of this type is the $k-\varepsilon$ model, which introduces two extra transport equations for the turbulence closure.

2.4.1 $k-\varepsilon$ model

This model introduces an extra transport equation for k:

$$\frac{\partial(\rho k)}{\partial t} + div\,(\rho k \boldsymbol{U}) = div\left[\frac{\mu_t}{\sigma_k} grad\ k\right] + 2\mu_t S_{ij}.S_{ij} - \rho\varepsilon \tag{2.64}$$

Where S_{ij} are the mean components of the rate of deformation. Then this model introduces another extra transport equation for ε, the rate of dissipation of turbulent energy per unit mass:

$$\frac{\partial(\rho\varepsilon)}{\partial t} + div\,(\rho\varepsilon \boldsymbol{U}) = div\left[\frac{\mu_t}{\sigma_\varepsilon} grad\ \varepsilon\right] + 2C_{1\varepsilon}\frac{\varepsilon}{k}\mu_t S_{ij}.S_{ij} - C_{2\varepsilon}\rho\frac{\varepsilon^2}{k} \tag{2.65}$$

μ_t is linked to k and ε through the expression:

$$\mu_t = \rho C_\mu \frac{k^2}{\varepsilon} \tag{2.66}$$

In (2.64), (2.65) and (2.66) five constants appear, whose values are obtained by empirical fitting. The following standard values have been proven to give good results for many kinds of turbulent flows:

$$C_\mu = 0.09,\ \ \sigma_k = 1.00,\ \ \sigma_\varepsilon = 1.30,\ \ C_{1\varepsilon} = 1.44,\ \ C_{2\varepsilon} = 1.92$$

3 Methodology

In this section, the proposed BEM implementation in OpenFOAM will be explained. First, we will provide a simple description of the CFD software (OpenFOAM) and of the simple axial actuator disc library that was later modified to include the BEM. Secondly, we will illustrate the BEM implementation procedure. Then the test case geometry and operation conditions will be described. Finally will be described the drag disc and the Jensen model.

3.1 OpenFOAM

OpenFOAM (Open Field Operation and Manipulation) is a free, open-source code written in C++, dedicated to the solution of all continuum mechanics problems but especially for computational fluid dynamics (CFD). This software has a good diffusion especially in academic organizations. For the post-processing analysis and the visualization of simulations Paraview was used. These information are reported on the OpenFOAM documentation. The OpenFOAM version used for this work is version 2.2.0, while the simpleFoam steady-state incompressible solver was used to solve the Reynolds-Averaged N-S equations.

3.2 The original Actuator Disk

OpenFOAM 2.2.0 contains a built-in axial actuator disk model. This library is called actuationDiskSource. In this implementation, the user needs to supply:

- The orientation of the disk
- The disk area
- The power and thrust coefficient of the modeled turbine
- The point inside the domain where the upstream velocity is sampled

The code begins by evaluating the axial induction factor a as:

$$a = 1 - \frac{C_P}{C_T} \tag{3.1}$$

This relation is obtained equaling the equation (2.15) and (2.18).

After this, the thrust coefficient is recalculated via equation (2.15) and the total thrust acting on the disk is computed.

The disk is defined as a geometrical volume, by its center, radius and thickness. Center coordinates, radius and thickness are input variable. The computational cells whose center is inside the disk volume are considered to be part of the actuator disc. Each one

of this cells is then assigned a point force, equal to the total thrust force multiplied by the ratio between the single cell volume and the total volume of all the cells inside the disk.

3.3 The modified Actuator Disk

In this work, the aforementioned actuationDiskSource library was improved by including a BEM disk model. A new simpleFoamAD solver was implemented, which was able to call the new library, called actuationDiskSourceBEM. The code is able to calculate a distributed force across the rotor disk by making use of the BEM theory, as described in 2.3. In this section, we will illustrate how the software works and the solutions adopted for the critical parts in the software.

As a first step, the user has to supply:

- The orientation of the disk
- The number of elements in which the blade is divided (n)
- The number of blades (N)
- The Tip Speed Ratio (TSR)
- The thickness of the disk (t)
- Radius where airfoil part starts (R_s)
- Radius where cylindrical part ends (R_E)
- The characteristic of the blade: radius, chord, local pitch angle (r, c, θ)
- The airfoil proprieties: α, C_l, C_d
- The aerodynamic cylinder properties (we consider them independent from α): C_l, C_d
- The point inside the domain where the upstream velocity is estimated

The radius where the airfoil part starts is at R_s while the radius where the cylindrical part ends is at R_E. This is because the blades are usually structured to have a supporting cylindrical part which is used to connect the blade to the hub.

The code starts by evaluating the angular velocity Ω as:

$$\Omega = \frac{TSR\ U_\infty}{R} \tag{3.2}$$

After that, the code defines the blade elements. Their number, as seen from the list above, is an input, and they are evenly spaced along the blade. The correspondent chord and local pitch angle of every blade station is evaluated through interpolation of the values provided by the user.

Through the BEM algorithm (from step 1 to 7) with the Prandtl's tip loss factor and the correction for high value of a, the code evaluates for every blade station the induction factors a and a'. Before step 4 the code evaluates the aerodynamic properties of the

airfoil at the current blade element. By comparing the local radius value with R_s and R_E, the program uses either the aerodynamic characteristics of the airfoil, or of the cylinder, or a blend of the two. Furthermore it is important to note that a relaxation factor was introduced for the calculation of a and a', which means that a blend of the old and the new value of a and a' is fed to the next iteration, to avoid the calculation loop becoming unstable.

By the knowledge of φ, a and a', we can estimate the relative velocity U_{rel} with equation (2.29), then we can calculate the coefficient C_n and C_t with the equations (2.37) and (2.38), and at last the force per length in tangential direction p_N and the force per length in axial direction p_T with relations (2.35) and (2.36).

The axial thrust and the tangential force acting on the annular ring is obtained by integrating the relations (2.39) and (2.40). In order to minimize integration errors, the code considers that p_N and p_T vary in linear way:

$$p_T = A(r - r_{i-1}) + B \tag{3.3}$$

With:

$$A = \frac{p_{T,i} - p_{T,i-1}}{(r_i - r_{i-1})} \tag{3.4}$$

$$B = \frac{p_{T,i-1} r_i - p_{T,i} r_{i-1}}{(r_i - r_{i-1})} \tag{3.5}$$

And:

$$p_N = C(r - r_{i-1}) + D \tag{3.6}$$

With:

$$C = \frac{p_{N,i} - p_{N,i-1}}{(r_i - r_{i-1})} \tag{3.7}$$

$$D = \frac{p_{N,i-1} r_i - p_{N,i} r_{i-1}}{(r_i - r_{i-1})} \tag{3.8}$$

The index i and $i - 1$ indicate the two blade stations that contain the i^{th} annular ring.

Substituting the relations (2.69) and (2.72) in the equation (2.40), (2.39) and integrating we obtain:

$$T_i = \frac{1}{2}C({r_i}^2 - {r_{i-1}}^2) + D(r_i - r_{i-1}) \tag{3.9}$$

$$Q_i = \frac{1}{3}A({r_i}^3 - {r_{i-1}}^3) + \frac{1}{2}B({r_i}^2 - {r_{i-1}}^2) \tag{3.10}$$

They represent the axial thrust and the torque acting on the annular ring taken into consideration. We have also to evaluate the tangential force, found by integrating the following equation:

$$dN = Np_T dr \tag{3.11}$$

The result is:

$$N_i = \frac{1}{2}A({r_i}^2 - {r_{i-1}}^2) + B(r_i - r_{i-1}) \tag{3.12}$$

Summing the axial thrust and the torque for every annular ring we obtain the axial thrust and the torque acting on the disk. With relation (2.44) we can obtain the power and with relations (2.14) and (2.17) we can calculate the thrust and power coefficient.

3.3.1 Force distribution

When the BEM iteration is completed, we know the axial and tangential force which is acting on every annular ring. A criterion to divide the total force among the cells in the annular ring is then needed.

In a first version, the code simply divided the force among the cells whose cell center was inside the annular ring. This method had two major drawbacks. First, counting the cells when the simulation was executed in parallel resulted to be problematic. Second, this method caused strong force discontinuities between two consecutive annular rings. This is due to the presence of cells whose volume is shared between two adjacent annular rings but the cell is assigned the force by the ring which contains its cell center. This discontinuity results into a jeopardized velocity pattern close to the disk surface.

In the final version, a different force distribution method was chosen, to avoid the two previously mentioned problems. The code calculates the volume of the ring:

$$Vol_{ring} = \pi({r_i}^2 - {r_{i-1}}^2)t \tag{3.13}$$

Then it calculates a correction factor to account for the difference between the geometric volume of the geometrical boundaries of the cylindrical area defining the actuator disc and the sum of the volumes of the cells inside the actuator disc volume:

$$corr = \frac{\pi R^2 t}{V} \tag{3.14}$$

where V is the sum of all cells volumes whose cell centers fall inside the disk volume.

The forces assigned to the cells are:

$$f_{t,i} = \frac{T_i}{\left(\frac{Vol\ ring}{Vcell \cdot corr}\right)} \bar{d} \tag{3.15}$$

$$n_{t,i} = \frac{N_i}{\left(\frac{Vol\ ring}{Vcell \cdot corr}\right)} \bar{n} \tag{3.16}$$

Where $\bar{d}$ is a unit vector normal to the disk and $\bar{n}$ is a unit vector that lies on the disk plane and is perpendicular to the vector that defines the position of the cell center with respect to the disc center.

3.3.2 TSR constant and Ω constant

Since U_∞ is taken from a point upstream of the disk inside the domain, it changes for every solver iteration, even though very slightly. For this reason, relation (3.2) becomes unclear. For this reason two different implementations of the actuation disc library were attempted:

- TSR constant
- Ω constant

In the first implementation, for every solver step the code inserts in the relation (3.2) the U_∞ extrapolated from a point inside the domain, to calculate Ω. The rotational speed of the turbine will therefore vary according to the U_{ref} in order to keep the TSR constant. The velocity triangles will therefore be constant, and the power and thrust coefficients will also be constant throughout the solver iterations.

In the second implementation, the code estimates Ω via relation (3.2) only for the first time step. In the following time steps, the code keeps Ω constant. Hence, for every time step, the TSR varies and the power and thrust coefficients are not constant throughout the different iterations needed for the code to converge.

In the result section we will note that these two different implementations generate very little changes in the results.

3.4 Cases analyzed

For the validation of the code, I used the same test cases analyzed in the Blind Test by Krogstad and Eriksen [9].

The test cases are:

- TSR=6
- TSR=3
- TSR=10

In this section I illustrate the geometry, boundary condition and initial condition of cases tested with my code.

3.4.1 Domain geometry

The domain has roughly the same dimension of the test section of the wind tunnel. The length of the interval is:

$$x = 14\ m$$

The cross section has rectangular shape, and the height of the wind tunnel is slightly diverging in order to the static pressure constant in the test section. This is neglected in the current computational domain:

Height H:

$$y = 1.81\ m$$

Width W:

$$z = 2.72\ m$$

An actuator disk has theoretically zero thickness but, when implemented in finite volume CFD code, it must have a thickness in order to identify the cells to which the force needs to be assigned to, meaning that the actuator disk is practically a cylinder. The radius of the disk is equal to the tip radius of the rotor. We have studied the sensitivity of the simulations with respect to two different thicknesses of the cylinder:

- $t = 5\ cm$
- $t = 10\ cm$

The disk was positioned on the absolute coordinates:

$$x = 4\ m$$

$$y = 0.905\ m$$

$$z = 1.36\ m$$

Hence the disk center is placed exactly in the cross-section center, we expect that the wake will be symmetric with respect to the two planes. In the experimental tests, the turbine center was placed at:

$$y = 0.817\ m$$

Nacelles and tower are neglected.

3.4.2 Mesh

The mesh is constrained by the number of blade elements. To avoid a bad distribution of the force, the mesh dimension needs to be equal or smaller than the distance between two consecutive annular rings. The cases analyzed have 20 or 30 blade stations. With 20 blade stations and considering a tip radius of $0.447\ m$, the maximum mesh cell size can be $2.2\ cm$. With 30 blade elements the maximum cell size is about $1.5\ cm$. To avoid using a fine mesh in the whole domain, the mesh was refined only inside the cylinder. The refinement was performed by dividing the hexahedral cell elements into 8 smaller cells. In table 3.1 the different mesh configurations are summarized.

Table 3.3.1 Different mesh configurations

Number of blade stations	Dimension of the cell out of the cylinder
20	$4\ cm$ $3\ cm$ $2\ cm$
30	$2\ cm$ $1.5\ cm$

3.4.3 Blade geometry and airfoil aerodynamic characteristic

The tip Radius of the blade is, as mentioned above, $R = 0.447\ m$. The characteristic of the blade (chord and local pitch angle) are reported in the Table 3.3.2.

Table 3.3.2 Definitions of chord length and local pitch angle as a function of blade radius(Pierella, F, Eriksen, PE, Sætran, L Krogstad , P-Å Invitation to the 2012 "Blind test 2" Workshop Calculations for two wind turbines in line. Department of Energy and Process Engineering, NTNU)

radius r [m]	chord c [m]	local pitch angle θ [deg]
0.0075	0.0135	120
0.0225	0.0135	120
0.049	0.0135	120
0.055	0.0495	38
0.0675	0.081433	37.055
0.0825	0.080111	32.544
0.0975	0.077012	28.677
0.1125	0.073126	25.262
0.1275	0.069008	22.43
0.1425	0.064952	19.988
0.1575	0.061102	18.034
0.1725	0.05752	16.349
0.1875	0.054223	14.663
0.2025	0.051204	13.067
0.2175	0.048447	11.829
0.2325	0.045931	10.753
0.2475	0.043632	9.8177
0.2625	0.041529	8.8827
0.2775	0.039601	7.9877
0.2925	0.037831	7.2527
0.3075	0.036201	6.565
0.3225	0.034697	5.9187
0.3375	0.033306	5.3045
0.3525	0.032017	4.7185
0.3675	0.030819	4.1316
0.3825	0.029704	3.5439
0.3975	0.028664	2.9433
0.4125	0.027691	2.2185
0.4275	0.02678	1.097
0.4425	0.025926	-0.71674

The first three radiuses correspond to the part of the blade which is shaped as a circular cylinder. This part consists in the connection between the hub and the blade. In this blade section, the aerodynamic performance of the cylindrical airfoil is:

$$C_l = 0$$

$$C_d = 0.5$$

Both parameters are constant and independent from α.

The airfoil used all along the span is the 14% thick NREL S826. It has been designed to be used near the tip as reported in the Blind Test by Krogstad and Eriksen [10]. The blades were machined in aluminium, resulting in enough stiffness in order to neglect any aeroelastic effect.

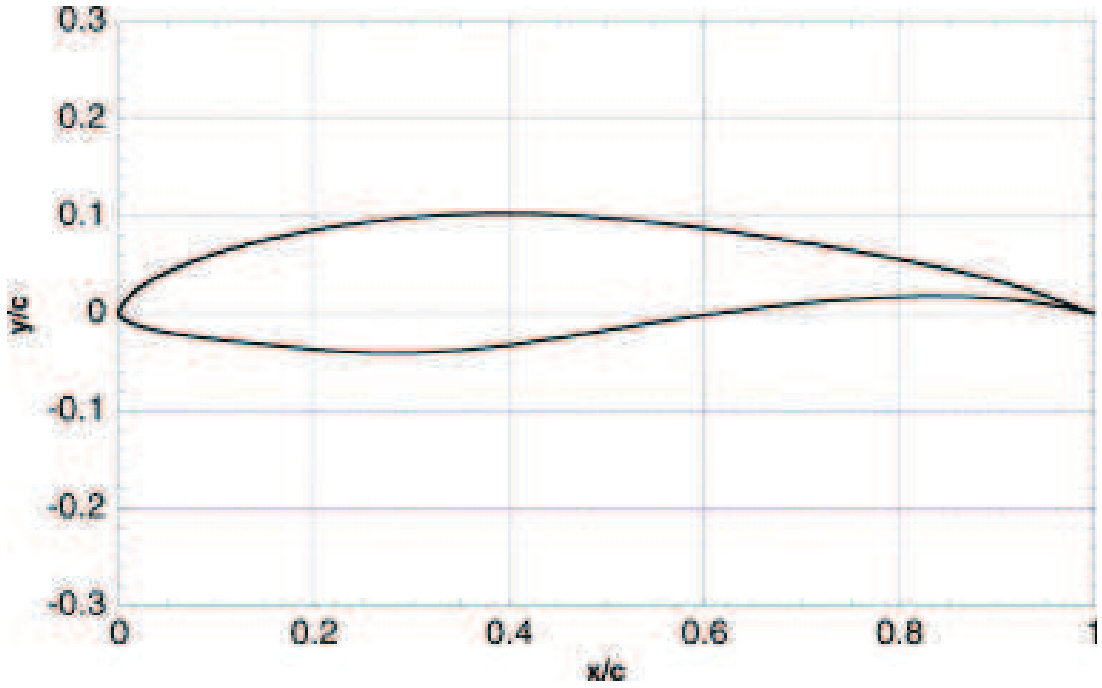

Fig.3.1 NEREL S826 airfoil (Krogstad , P-Å and Eriksen, PE (2012) "Blind test" calculations of the performance and wake development for a model wind turbine. Renewable energy, 50 (2013), pp 325-333)

As reported by Sarmast and Mikkelsen [11], at low Reynolds numbers, the aerodynamic behavior of the airfoil is strongly Reynolds dependent. The airfoil shows signs of post stall and before stall hysteresis in particular for very low Reynolds $Re = 4 \cdot 10^4$. The hysteresis is not present, for low and medium Reynolds $Re = 6 \cdot 10^4$ and $Re = 8 \cdot 10^4$ the hysteresis appears before and after stall, for high Reynolds the hysteresis compares only after stall.

Depending on the rotational regime of the turbine, the blade sections experience different local Reynolds numbers and therefore have different aerodynamic behaviors. In order to simplify the software algorithm, the C_l and C_d curve for $Re = 1.2 \cdot 10^5$ was chosen to be representative of the whole blade. The choice is motivated by the fact that this Reynolds number is relative to the blade tip at design condition, which gives the most significant contribution in terms of extracted power. The aerodynamic characteristic are obtained experimentally by Sarmast and Mikkelsen [12].

In Fig.3.2 and Fig.3.3 the experimental aerodynamic characteristics for $Re = 1.2 \cdot 10^5$ are reported.

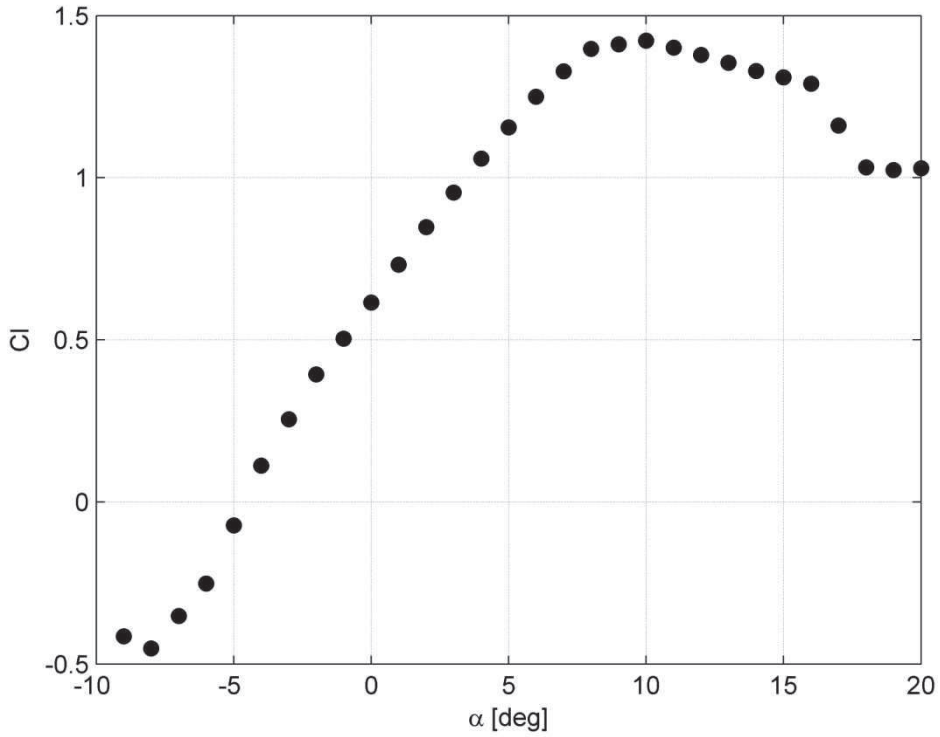

Fig.3.2 Cl-α Re=1.2exp5 NRELS826 airfoil

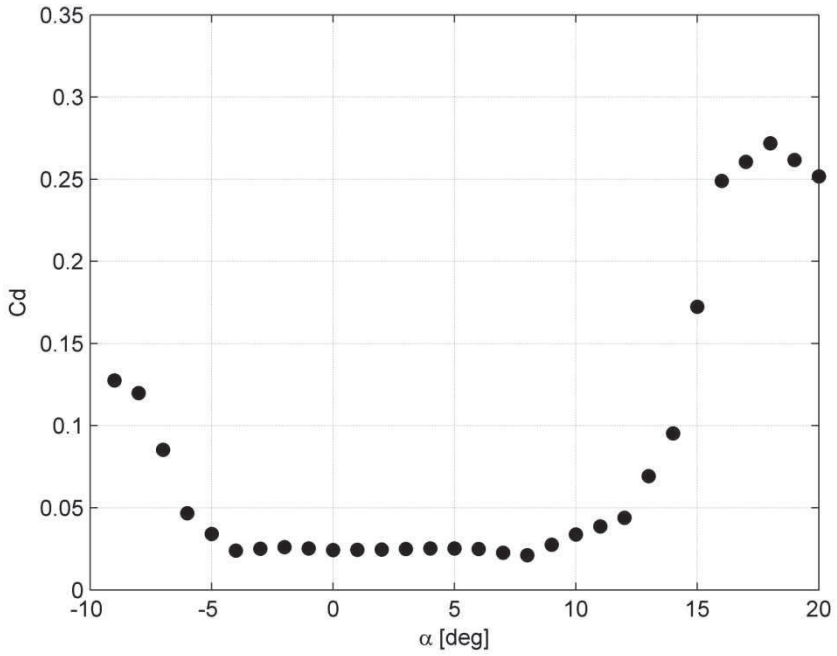

Fig.3.3 Cd-α Re=1.2exp5 NRELS826 airfoil

We expect that, at design condition and for all the blade stations, the airfoil works in the range $\alpha = -5° \div +5°$ where the drag coefficient is low and almost constant. At off-design conditions, the angle of attack can exceed these limits, therefore the aerodynamic

were extrapolated for a wider range via the AirFoilPreptool $\alpha = -180° \div +180°$, by Hansen, Windward Engineering, May, 2004, version 2.0.

In Fig.3.4 and Fig.3.5 the extrapolated aerodynamic characteristic are reported.

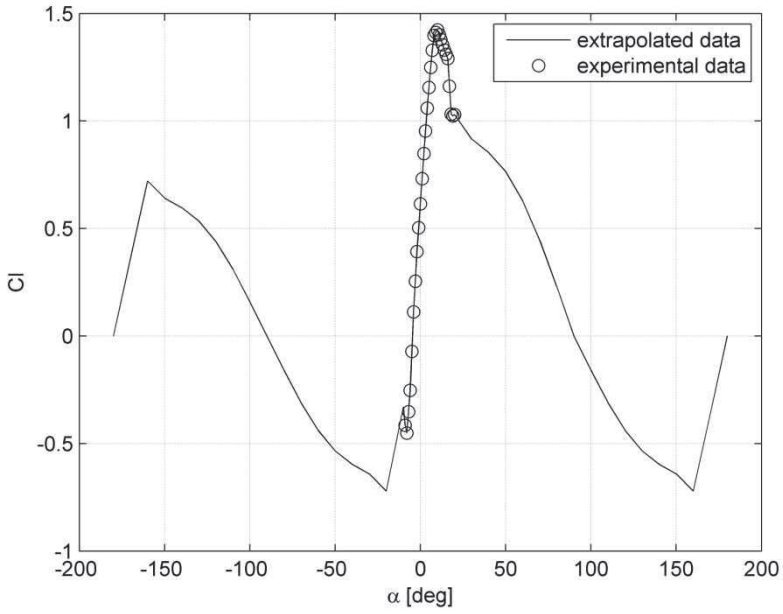

Fig.3.4 Cl-α Re=1.2exp5 NRELS826 airfoil extrapolated

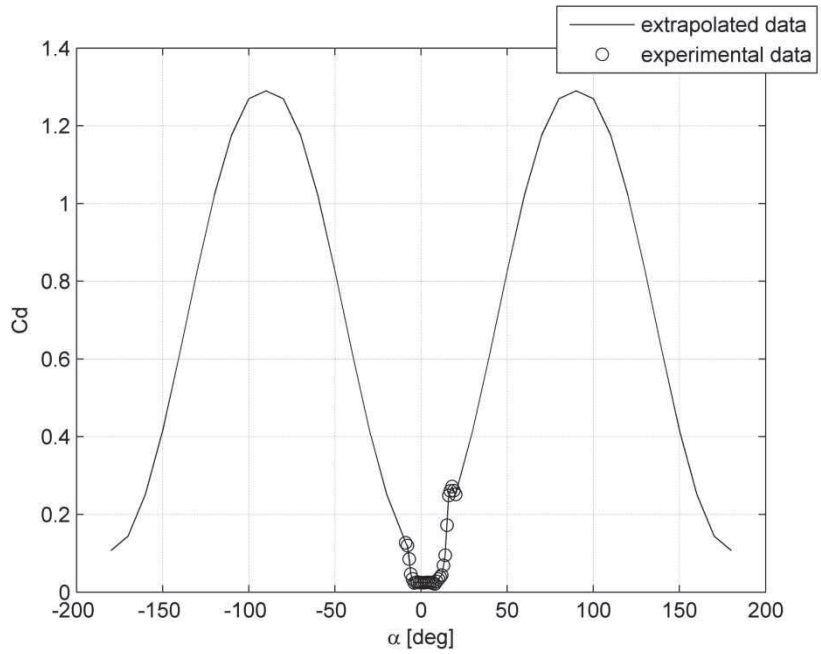

Fig.3.5 Cd-α Re=1.2exp5 NRELS826 airfoil extrapolated

At the blade root, there is a smooth transition between the circular cylinder and the section with the s826 airfoil. The aerodynamic characteristic in this region were estimated by means of a linear interpolation between the airfoil characteristic and the cylinder $C_l - C_D$.

3.4.4 Working condition

The TSR defines the working condition of the wind turbine. The model turbine is designed to have optimum efficiency at TSR=6. The performance and the wake of the turbine were also evaluated in off-design conditions, TSR=3 and TSR=10. Considering that the inlet speed remain the same for all the cases, a different TSR implies a different angular velocity Ω.

3.4.5 Boundary conditions and initial condition

The CFD software needs, as an input, the definition of the boundary conditions and initial conditions for the flow variables which for a steady-state solution of an incompressible turbulent flow with a $k-\varepsilon$ turbulence closure technique are: speed U, pressure p, turbulent kinetic energy k, turbulent dissipation ε, eddy viscosity μ_t. The domain boundaries are the inlet section, the wind tunnel walls (ground, top, sides), and the outlet section.

Table 3.3.3 U and p boundary and initial condition

	U	p
Inlet	fixed value of (10 0 0) m/s	absence of gradient
Outlet	absence of gradient	fixed value 0 m^2/s^2
Ground wall	fixed value of (0 0 0) m/s	absence of gradient
Top wall	fixed value of (0 0 0) m/s	absence of gradient
sides wall	fixed value of (0 0 0) m/s	absence of gradient
internal field (initial condition)	(10 0 0) m/s	0 m^2/s^2

For the definition of the turbulent kinetic energy inlet boundary and initial conditions the following relation by Versteeg and Malalasekera [13] was used:

$$k = \frac{3}{2}(U_{ref}T_i)^2 \tag{3.17}$$

Where $U_{ref} = 10m/s$ is the reference speed and $T_i = 0.3$ % is the turbulence intensity at the inlet section of the NTNU wind tunnel.

For what concerns the turbulent dissipation:

$$\varepsilon = {C_\mu}^{3/4}\frac{k^{3/2}}{l} \tag{3.18}$$

Where l is the length scale representative of the large-scale turbulence.

The value of μ_t is evaluated with the relation (2.66).

The simulations were run with two values of l:

- $l = 0.7L$ where L is an characteristic length of the equipment, for our case I used the equivalent diameter of the wind tunnel cross section

$$L = 2\sqrt{\frac{W \cdot H}{\pi}} = 2.48756 \tag{3.19}$$

- $l = 0.035\ m$ experimental, reported in the Blind test 3 by Krogstad and Sætran [14]

The boundary conditions for the turbulent quantities and the initial condition for the cases with l calculated as from equation (3.19)

Table 3.3.4 k,ε,μ_t boundary and initial condition, l calculated

	k	ε	μ_t
Inlet	fixed value 0.00135 m^2/s^2	fixed value 4.6807exp(-6) m^2/s^3	calculated from k and ε fixed value 0.0350427956 m^2/s^3
Outlet	absence of gradient	absence of gradient	calculated from k and ε
Ground wall	wall function that openFoam calls kqRWallFunction	wall function that openFoam calls epsilonWallFunction	wall function that openFoam calls nutkWallFunction
Top wall	wall function that openFoam calls kqRWallFunction	wall function that openFoam calls epsilonWallFunction	wall function that openFoam calls nutkWallFunction
sides wall	wall function that openFoam calls kqRWallFunction	wall function that openFoam calls epsilonWallFunction	wall function that openFoam calls nutkWallFunction
internal field (initial condition)	0.00135 m^2/s^2	4.6807exp(-6) m^2/s^3	0.0350427956 m^2/s^3

The boundary conditions and the initial conditions for the cases with the experimental value of $l$are reported in the Table 3.3.5

Table 3.3.5 k,ε,μ_t boundary and initial condition, l experimental

	k	ε	μ_t
Inlet	fixed value 0.00135 m^2/s^2	fixed value 0.0002328705 m^2/s^3	calculated from k and ε fixed value 0.0007043614 m^2/s^3
Outlet	absence of gradient	absence of gradient	calculated from k and ε
Ground wall	wall function that openFoam calls kqRWallFunction	wall function that openFoam calls epsilonWallFunction	wall function that openFoam calls nutkWallFunction
Top wall	wall function that openFoam calls kqRWallFunction	wall function that openFoam calls epsilonWallFunction	wall function that openFoam calls nutkWallFunction
sides wall	wall function that openFoam calls kqRWallFunction	wall function that openFoam calls epsilonWallFunction	wall function that openFoam calls nutkWallFunction
internal field (initial condition)	0.00135 m^2/s^2	0.0002328705 m^2/s^3	0.0007043614 m^2/s^3

It is possible to observe that the inlet condition for turbulent viscosity is very different for the two different values of the integral length scale. If we use equation (3.19), the turbulent viscosity is 20 times higher than the experimental value, likely leading to a considerable overestimation of the turbulent spreading rate of the wake.

3.5 Drag Disc

The Drag Disc is a circular grid and it is used to experimentally simulate a turbine. The disc induces a momentum loss in the flow, and if properly designed its wake can simulate the wake of a wind turbine. The characteristics of the disc wake are different in many ways from the ones of a turbine, especially for what concerns turbulence production and the wake recovery rate.

The experimental results from Pierella and Sætran [15] on a drag disc with a regular mesh made up of square section cylinders were used in order to provide an additional validation dataset to the code.

The porous disc had an external diameter of $D = 80\ cm$, and a porosity (defined as open area over total disc area) of 55%. This porosity led to a thrust coefficient of $C_T = 0.82$, constant for the tested inflow velocities 8.5 m/s and 11 m/s.

3.6 Jensen Model

The Jensen model is a simple algebraic model used to predict the wake behind a wind turbine. The main vantage of this model is the very low computational cost, in fact it does not solve the turbulent field. The details of this model is reported by Jensen [16] and Choi and Shan [17].

In this model it is assumed a linear variation of the wake radius:

$$r_w = R + \alpha\, x \tag{3.20}$$

Where r_w is wake radius at the distance x from the rotor. The coefficient α is assumed equal to 0.1. Considering a constant value of the velocity in the cross section of the wake, evaluating the velocity behind the rotor with the relation (2.12), with a momentum balance we obtain:

$$U = U_\infty \left(1 - 2a \left(\frac{R}{R + \alpha\, x}\right)^2\right) \tag{3.21}$$

And using relation (2.15) we can express the velocity U in function of C_T and we obtain:

$$U = U_\infty \left(1 - \left(1 - \sqrt{1 - C_T}\right) \left(\frac{R}{R + \alpha\, x}\right)^2\right) \tag{3.22}$$

The Jensen model has a large diffusion among the companies, and it is often used to design wind farms, after having been calibrated via an as big as possible experimental database in order to select the correct parameters.

4 Results

In this section we will illustrate the results obtained and validate them against the wind tunnel experimental data. Most of the computations are performed with the program version with constant TRS, while the constant rotational velocity results were only compared with the constant TSR computations.

First, a parametric study on the number of elements necessary to resolve the rotor disc was performed. The influence of the turbulent boundary condition and of the disk thickness was analyzed with the coarser mesh. The finer mesh, with 30 cells per rotor radius, was employed to produce the final results both for on-design and off-design conditions. After that, the results on a horizontal and a vertical diagonal will be compared. Then the results obtained from a simple actuator disk were compared with the version coupled with BEM. Finally, the actuator discs were compared with the porous disc and the simple Jensen model.

4.1 C_P and C_T

Before implementing the BEM on the actuator disc, it was deemed important to validate the BEM algorithm. Furthermore, we can calibrate how many blade stations are needed in order to correctly model the rotor. The following plots show the dependency of the C_P and C_T on the number of blade stations.

4.1.1 TSR=6

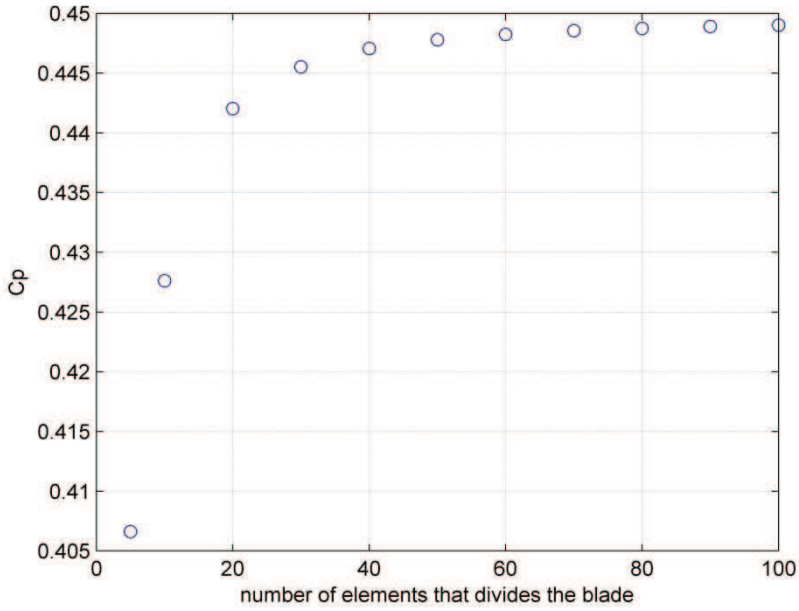

Fig.4.1 Cp-blade stations TSR 6

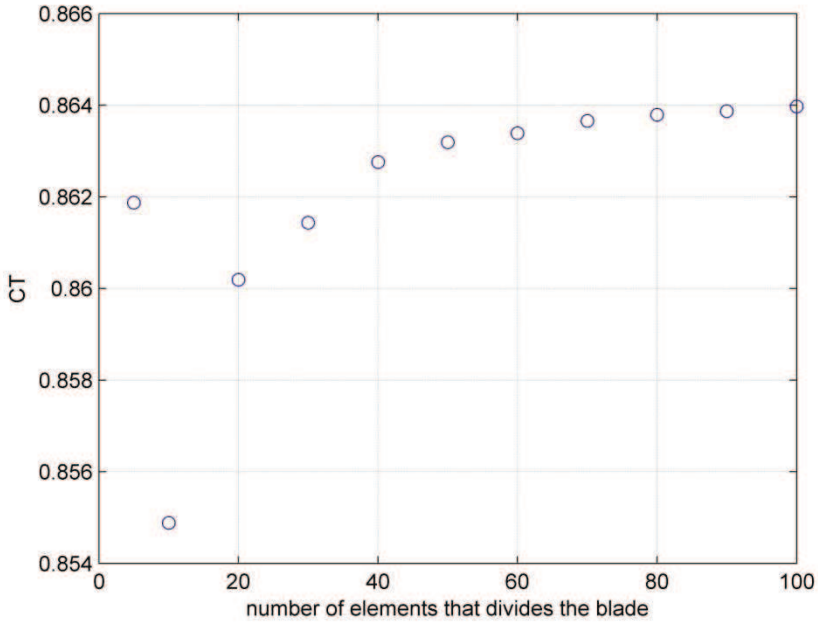

Fig.4.2 CT-blade stations TSR=6

From Fig.4.1 and Fig.4.2 we can note that, at design conditions, the C_P and C_T have an asymptotic behavior for increasing number of blade elements. If we take as the asymptotic value the results obtained with 100 blade elements, we can estimate the errors committed by choosing a smaller number of elements, namely 20 or 30 elements for the current work.

Table4.1 Discretizazion blade error at TSR=6

	C_P	C_T
20 elements	1.56 %	0.44 %
30 elements	0.78 %	0.29 %

4.1.2 Off-design conditions. TSR=3

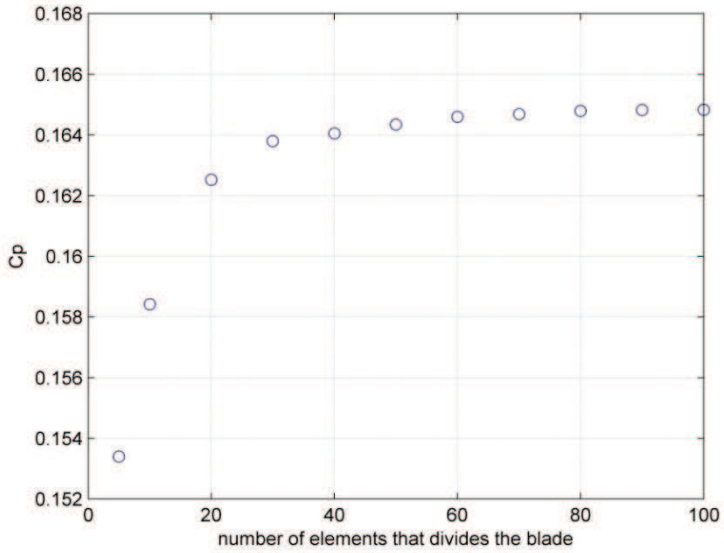

Fig.4.3 Cp-blade stations TSR=3

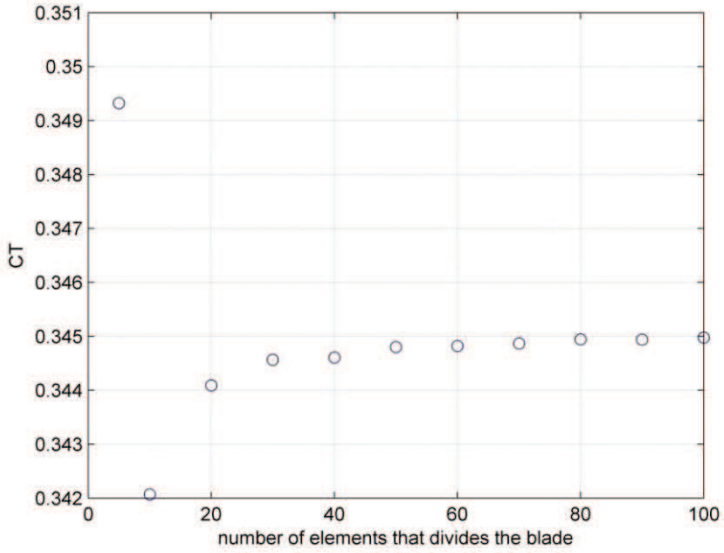

Fig.4.4 CT-blade stations TSR=3

From Fig.4.3 and Fig.4.4 we can note that at off-design conditions (TSR=3), C_P and C_T have also an asymptotic behavior. In table 4.2 the errors as a function of the number of blade elements are listed, taking the asymptotic value as the result obtained with 100 blade elements.

Table 4.2 Discretizazion blade error at TSR=3

	C_P	C_T
20 elements	1.39 %	0.25 %
30 elements	0.62 %	0.11 %

4.1.3 Off-design conditions. TSR=10

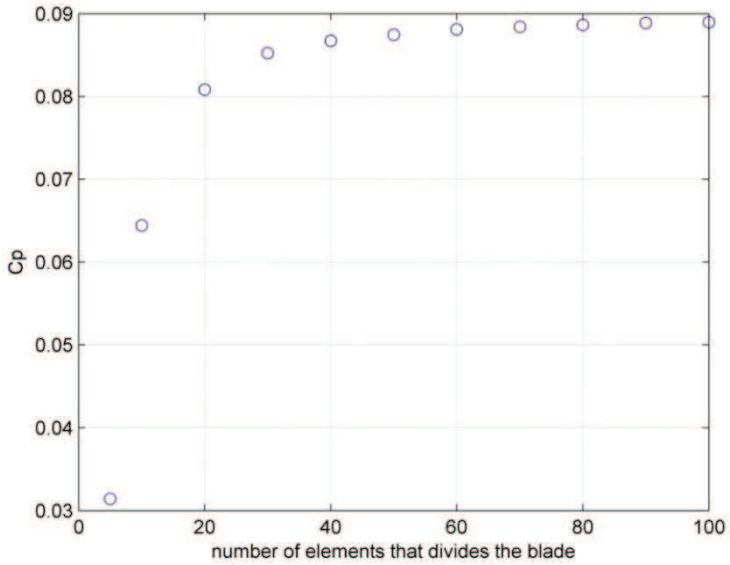

Fig.4.5 Cp-blade stations TSR=10

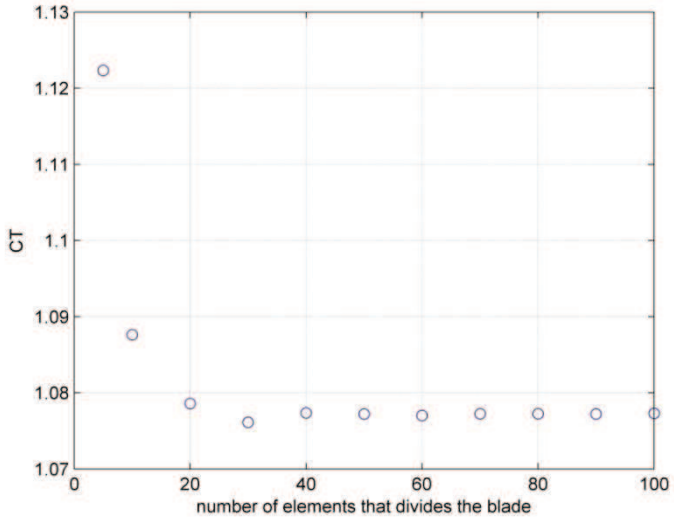

Fig.4.6 CT-blade stations TSR=10

From Fig.4.5 and Fig.4.6 we can observe the behavior for TSR=10. In table 4.3, the errors for 20 and 30 elements are listed:

Table 4.3 Discretizazion blade error at TSR=10

	C_P	C_T
20 elements	9.15 %	0.12 %
30 elements	4.20 %	0.11 %

By observing the percentage errors, we can note that at on-design conditions the error linked with the C_T is in all cases less than 0.5 %. This error is the most significant for our analysis because the C_T is linked with the axial force that the disk exerts on the flow, thus defining the wake velocity deficit and shape. At on-design conditions, the error linked with C_P is less than 1 % when using 30 blade elements, and anyway less than 2 % when employing 20 elements. The maximum error on the $C_P$is for TSR=10. To have an error below the 5 % threshold, we must use 30 elements.

Using more than 30 elements would allow more accurate results. Anyway, this would imply a higher mesh refinement inside the actuator disk and a higher total cells number, which would require an unrealistically high computational cost.

According to the previous observations we can consider 30 elements enough in order to have an adequate accuracy in all our simulations, both on-design and off-design. Since sensitivity analysis to different parameters is run at on-design conditions, using 20 cells is a good compromise between accuracy and computational cost.

The Fig.4.7 and Fig.4.8 show the C_P and C_T as a function of TSR, compared with the experimental results by Krogstad and Eriksen [18]. In this analysis, the blade is divided in 30 elements.

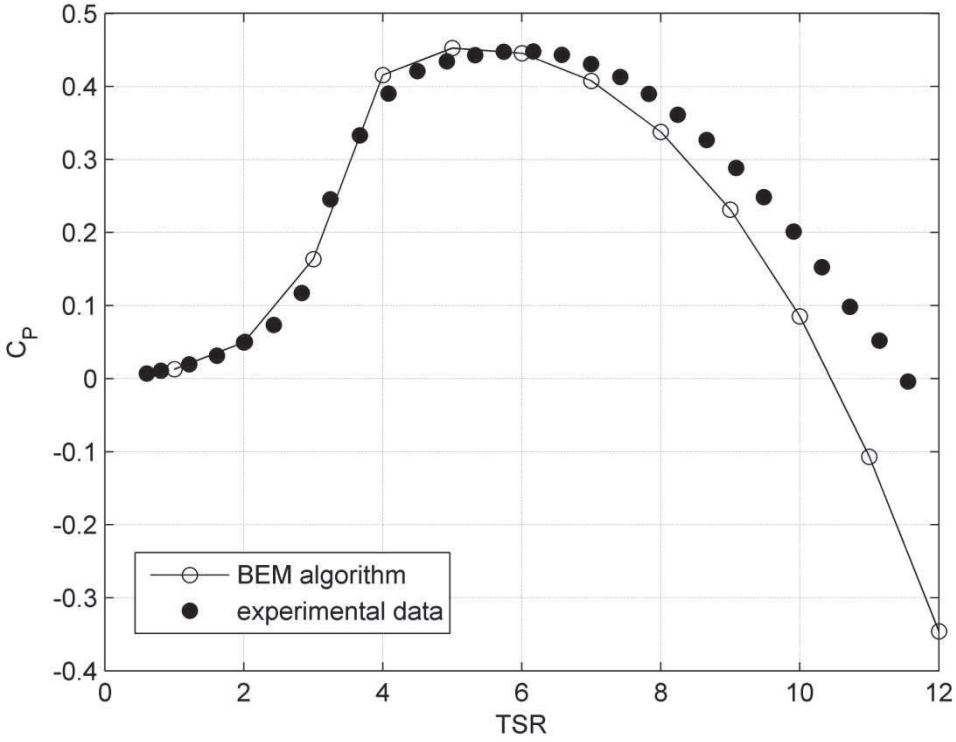

Fig.4.7 Power coefficient in function of TSR

From Fig.4.7 we can note that the agreement is very good around on-design conditions and for low TSR numbers. However, for high TSR, the BEM algorithm diverges from the experimental data and already around TSR=10 the error is not negligible. Another incongruence is the TSR for which optimum efficiency is achieved: the turbine is in fact designed for TSR=6, but the BEM algorithm predicts a maximum around TSR=5.

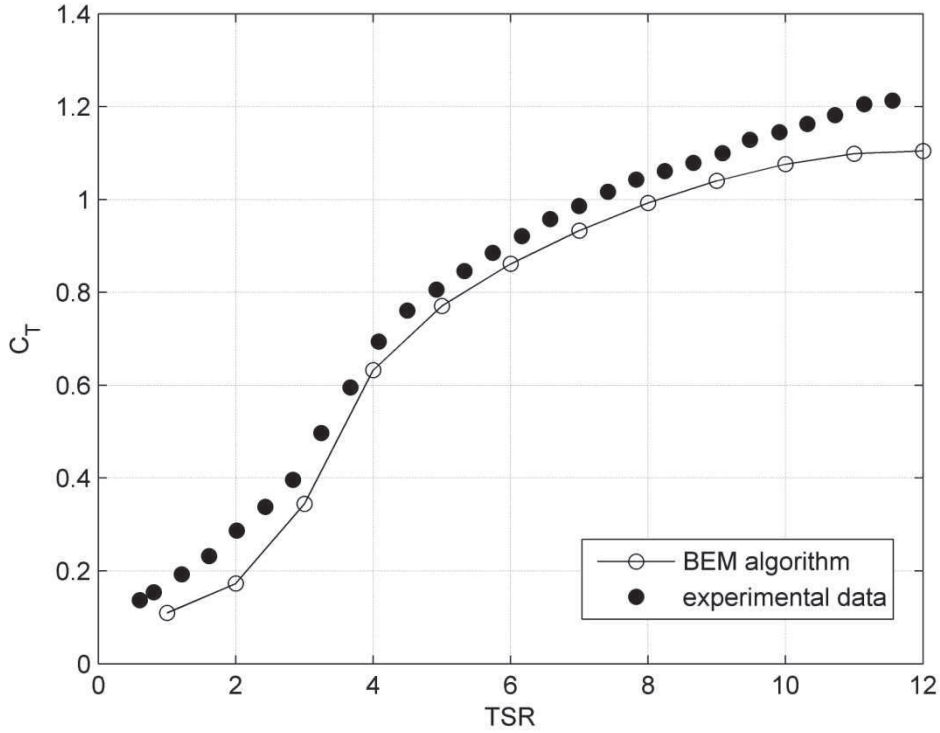

Fig.4.8 Thrust coefficient in function of TSR

From Fig.4.8 we note that the agreement of the thrust coefficient is quite good almost everywhere, even though there seems to be a constant offset of around 0.05 between the two curves. Only for very high TSR the two data series start to diverge significantly. The matching is particularly good close to the design TSR.

4.2 The blade discretized by 20 elements

All the following results are computed considering 20 elements in the blade span. The turbine is always running at on-design conditions, TSR=6.

4.2.1 Mesh dependence

First we need to analyze the mesh independency, in order to choose a mesh which is fine enough to accurately describe the problem with a not excessive computational cost. We carried out the analysis for two different values of the inlet turbulent length scale, as illustrated in the methodology section: $l = 1.7413\, m$ calculated, $l = 0.035\, m$ experimental. The variables of interest are plotted along a line passing through the disk center having the same orientation of the normal disk axis and along a horizontal line at a downstream distance of 3 rotor diameters.

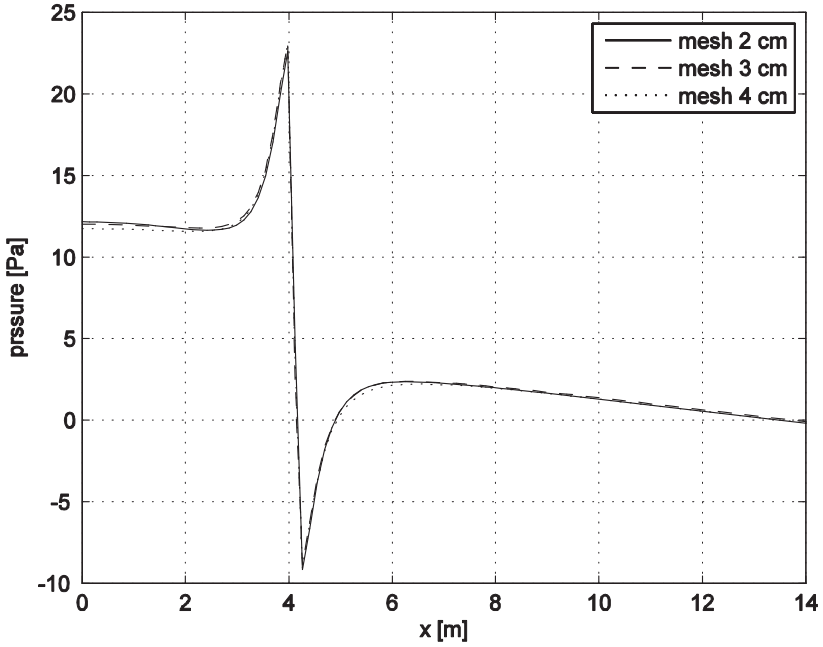

Fig.4.9 Pressure profiles along the centerline, mesh dependence, n 20, $l = 1.7413\ m$ (calculated)

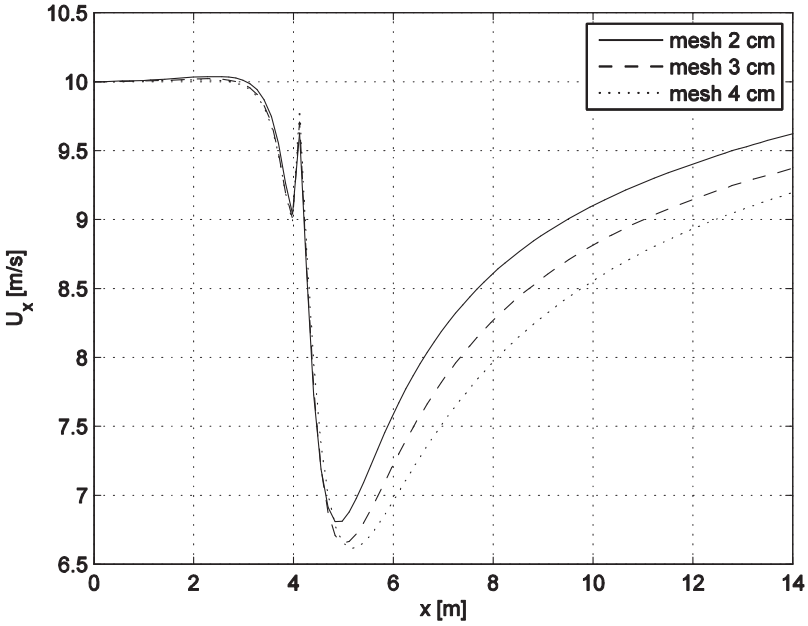

Fig.4.10 Axial speed profiles along the centerline, $l = 1.7413\ m$ (calculated)

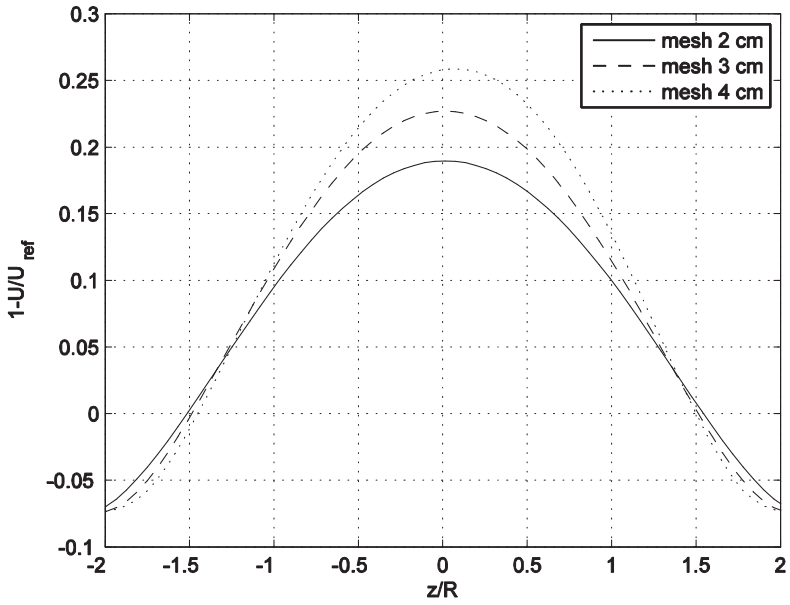

Fig.4.11 Mean velocity profiles along a horizontal line X/D=3,mesh dependence, n 20,$l = 1.7413\ m$ (calculated)

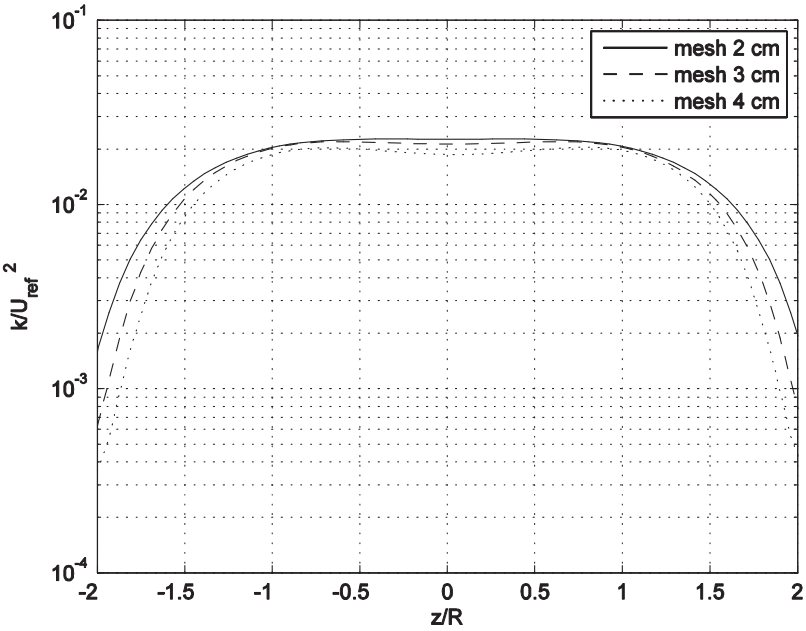

Fig.4.12 Turbulent kinetic energy profiles along a horizontal line X/D=3,mesh dependence, n 20,$l = 1.7413\ m$ (calculated)

From Fig.4.9, Fig.4.10, Fig.4.11, Fig.4.12 we can notice a strong mesh dependence if we use $l = 1.7413\ m$, except for what concerns the pressure values. For this reason, in the following analyses, the simulations with 20 blade elements will be run with a mesh of 2 cm.

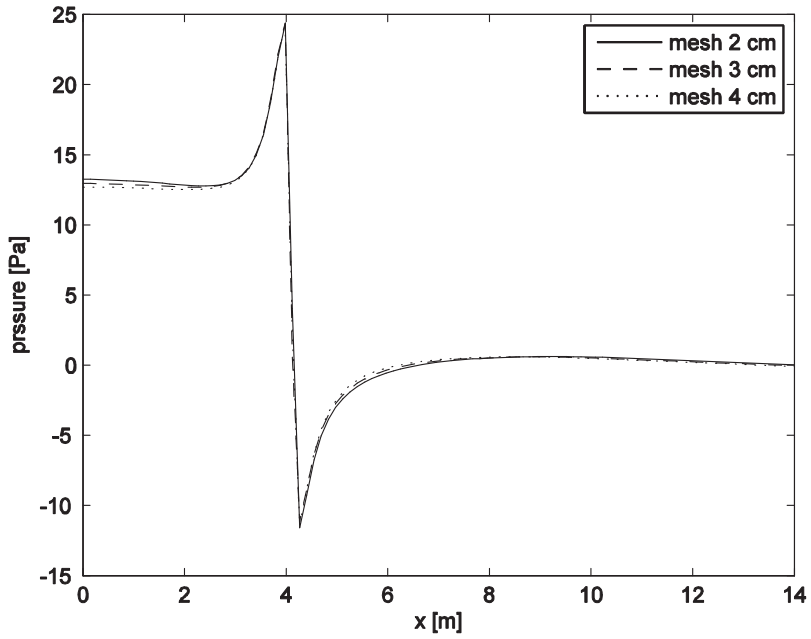

Fig.4.13 Pressure profiles along the centerline, mesh dependence, n 20, $l = 0.035\ m$ (experimental)

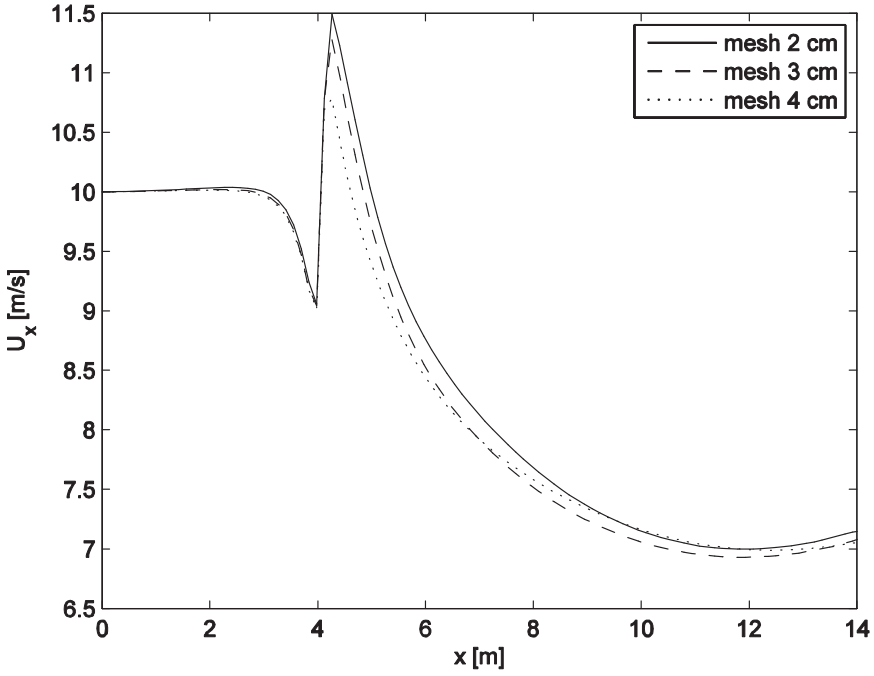

Fig.4.14 Axial speed profiles along the centreline, mesh dependence, n 20, $l = 0.035\ m$ (experimental)

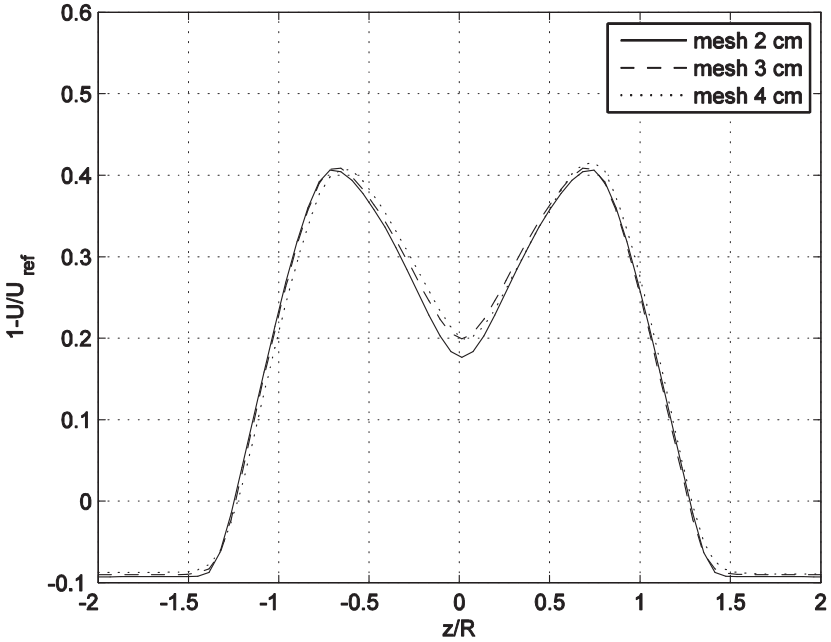

Fig.4.15 Mean velocity profiles along a horizontal line X/D=3, mesh dependence, n 20, $l = 0.035\ m$ (experimental)

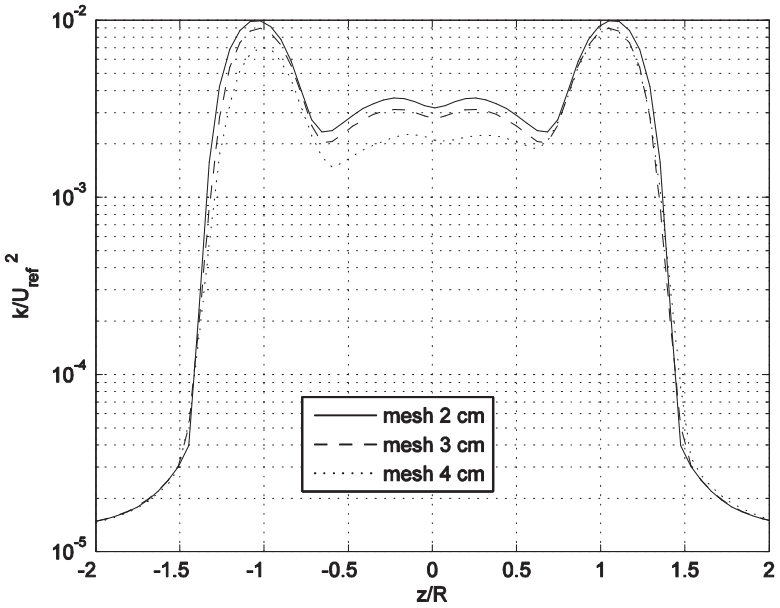

Fig.4.16 Turbulent kinetic energy profiles along a horizontal line X/D=3, mesh dependence, n 20, $l = 0.035\ m$ (experimental)

With the experimental value of the turbulent length scale ($l = 0.035\ m$) the mesh dependence is less strong. The mean velocity profiles in the wake, the most important parameter for our analysis, shows that a 3cm mesh is accurate enough. We can also note that a coarse mesh (4 cm) produces non-symmetric profiles in the wake (Fig.4.15 and

Fig.4.16). This is not acceptable since the analyzed cases are symmetric in geometry and boundary conditions. This problem is probably due to numerical errors.

4.2.2 Turbulent boundary condition influence

In the following plots, we compared the experimental data from the wind tunnel measurements with the result obtained with two different turbulent length scales, as illustrated in the section 3.4.5: $l = 1.7413\, m$ calculated from equivalent diameter, $l = 0.035\, m$ experimental. The mesh used for both cases is the same, with a cell size of 2 cm, since it is important that the cases differ only for the turbulent boundary condition. We have previously observed in section 4.2.1 that the case with the turbulent length scale (TLS) calculated by relation (3.19) does not reach an asymptotic condition for the analyzed meshes, while a 2 cm mesh guarantees mesh independency for the case with the experimental turbulent length scale.

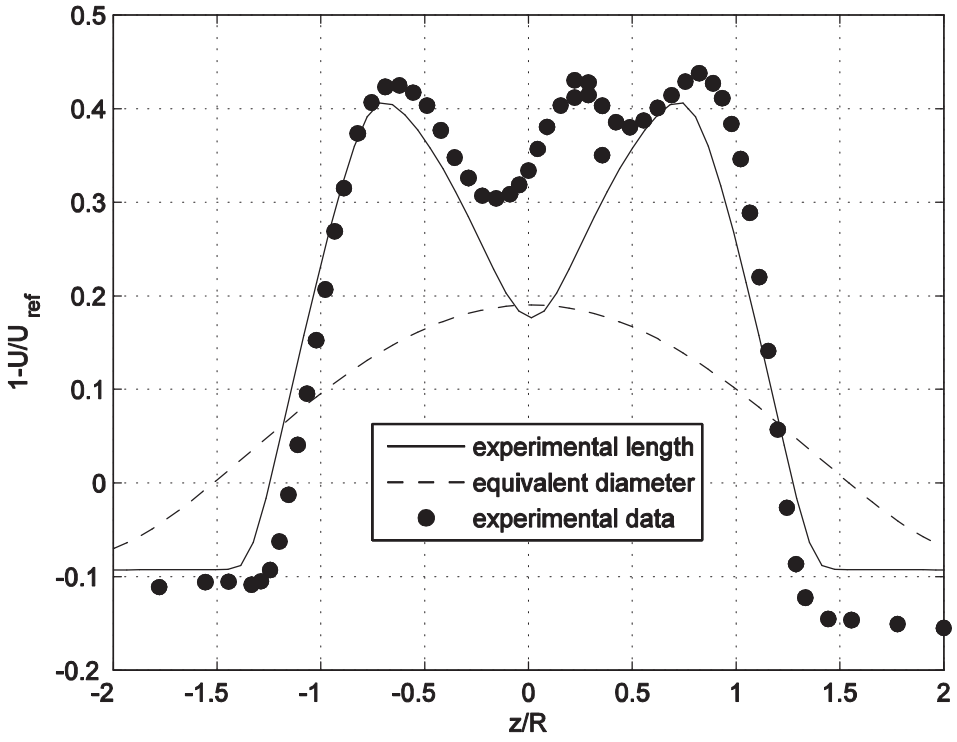

Fig.4.17 Mean velocity profiles along a horizontal line X/D=3, l dependence

The agreement between the profile with experimental TLS and the wind tunnel data is very good. Obviously the peak at $z/R \approx 0.3$ cannot be reproduced since it is due to the presence of the nacelle and the tower, as reported by Krogstad and Eriksen [19]. The dip in the centerline, observable both for the experimental and numerical data, is due to flow acceleration: the blades do not extend to the disk center, therefore no energy extraction is possible in that zone. This dip is deeper in the simulation with experimental TLS, since we did not include the nacelle in the model. The flow acceleration due to solid blockage causes negative values of the velocity profile for $|z/R| > 1.2$. This acceleration is a consequence of mass conservation in the closed

wind tunnel section, and to the steady treatment of the problem. Therefore, the velocity deficit due to the presence of the disk must be balanced by a flow speed-up around the disk. The average velocity must remain the same in all the cross sections.

On the other hand, the velocity profile obtained with the calculated TLS is completely different. The high value of the turbulent length scale causes an immediate diffusion of the wake, which reaches a Gaussian shape immediately after the rotor.

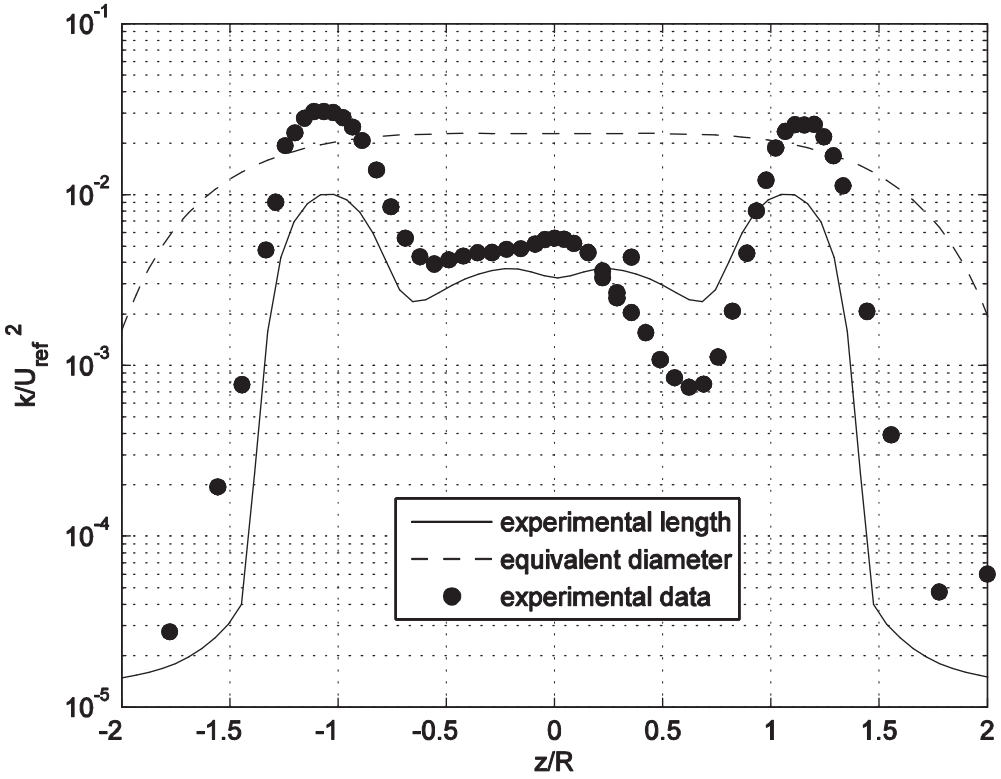

Fig.4.18 Turbulent kinetic energy profiles along a horizontal line X/D=3, l dependence

As for the turbulence, the agreement of the profile with experimental TLS and the wind tunnel data is quite good. Obviously the asymmetry at the centerline cannot be reproduced, but our model is able to predict the peaks position at the edges of the disk. In the experiment, the presence of these peaks is due to the tip vortices and partly to the turbulent kinetic energy produced in the shear layer between the wake and the undisturbed flow. The height of the peak is underestimated by 3 times. Again the model with calculated outputs completely wrong TKE values, far too high across the disc, meaning a high degree of turbulent diffusion which explains the Gaussian mean velocity profile shape.

From these two plot it is clear that a more precise inlet flow description (supported by experimental results) yields in a more accurate prediction.

In the following analysis, the simulations will be run the turbulent boundary condition deriving from experimental data ($l = 0.035$ m), which guarantees a more precise velocity distribution and a lower amount of diffusion.

4.2.3 Disk thickness influence

In the following graphs two velocity profiles are reported, one obtained using a disk with thickness of 5 cm and the other with a thickness of 10 cm.

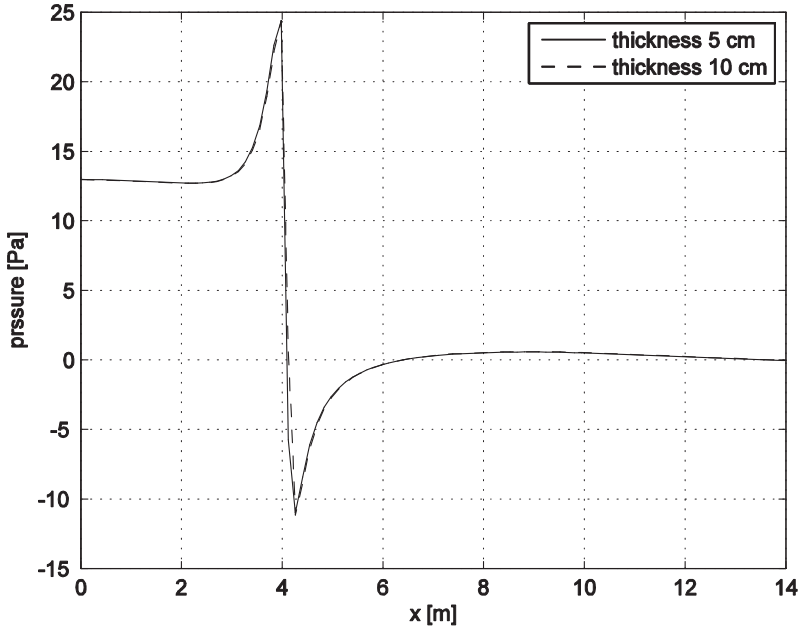

Fig.4.19 Pressure profiles along the centerline, thickness disc dependence

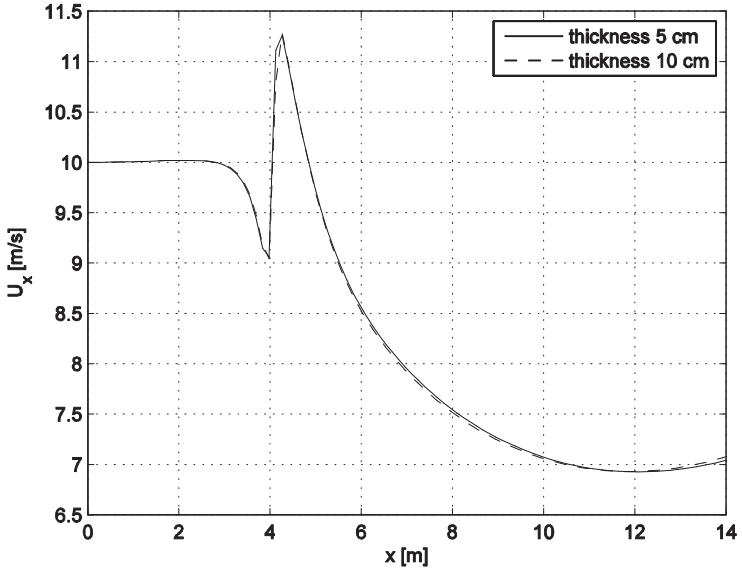

Fig.4.20 Axial velocity profiles along the centerline, thickness disc dependence

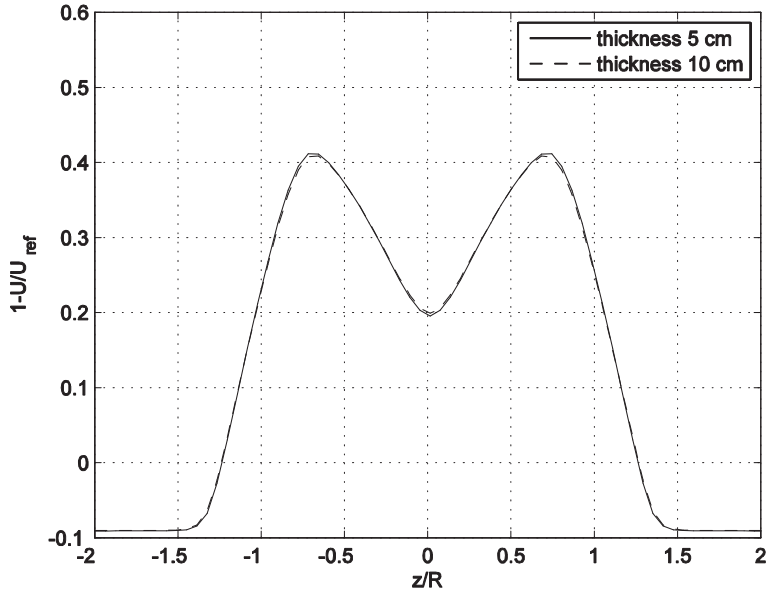

Fig.4.21 **Mean velocity profiles along a horizontal line X/D=3, thickness disc dependence**

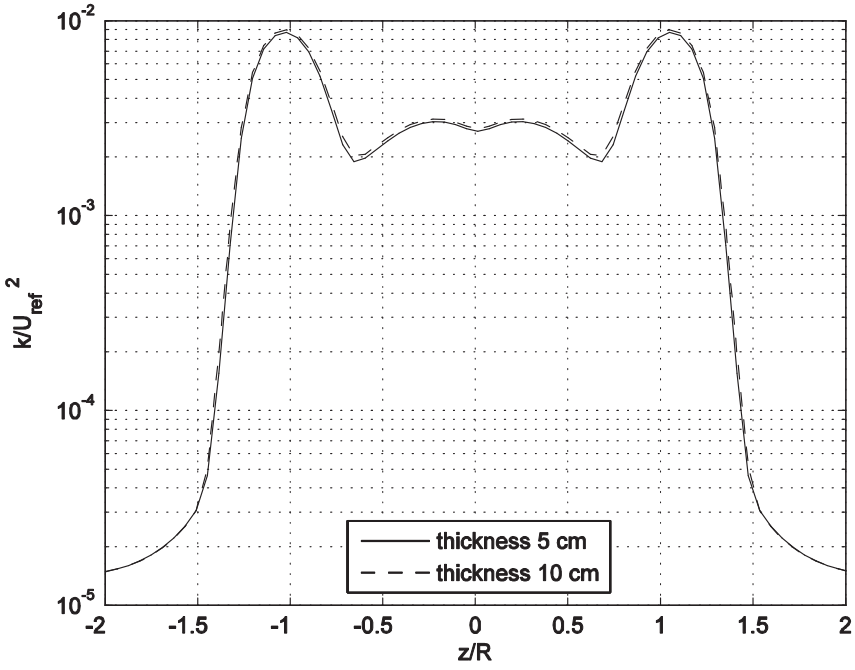

Fig.4.22 **Turbulent kinetic energy profiles along a horizontal line X/D=3, thickness disc dependence**

From Fig.4.19, Fig.4.20, Fig.4.21, Fig.4.22 we can note that there is a negligible influence of the disk thickness on all velocity profiles. Although the average value of the blade chord projection on the axial direction is closer to 5 cm, in the following

analysis a disk of 10 cm of thickness will be used, since a lower thickness gives some velocity discontinuity across the disk boundary (picture not reported) that are to some extent unphysical.

4.3 Influence of the number of elements that divided the blade

In the following graphs we report on the difference between profiles obtained using 20 elements, 30 elements and the reference experimental data. The size of the employed mesh is the same, 2 cm.

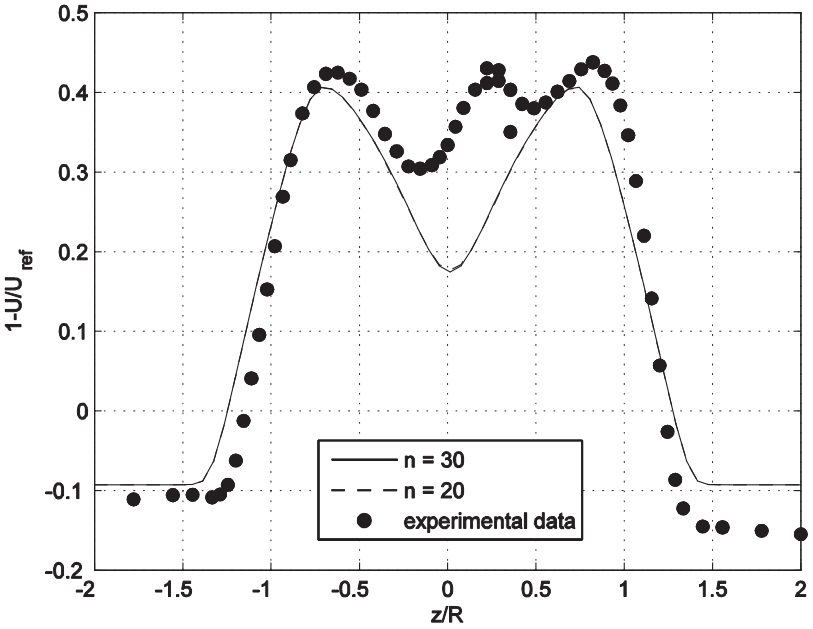

Fig.4.23 Mean velocity profiles along a horizontal line X/D=3, number blade stations dependence

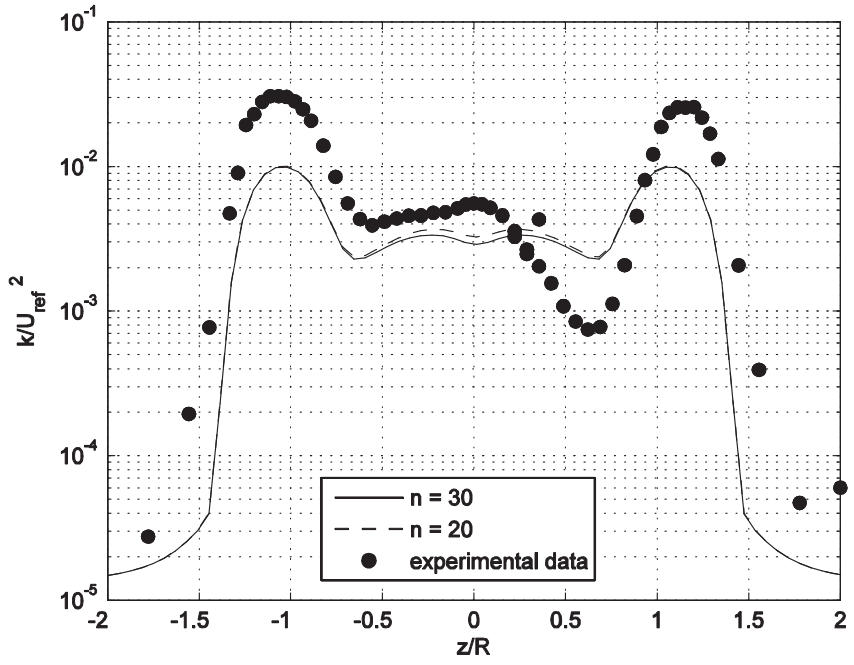

Fig.4.24 Turbulent kinetic energy profiles along a horizontal line X/D=3, number blade stations dependence

We can note that the wake is only slightly influenced by the number of blade elements. The differences are observable only in the turbulent kinetic energy graph, since the y-axis is in logarithmic scale. As previously reported, using 20 or 30 elements does not have a significant influence on the C_P and C_T values. For this reason also in the wake the differences are low. However the difference there are, so in the simulation I used 30 elements for a greater accuracy.

4.4 The blade discretized by 30 elements

All the following analysis are executed with 30 element.

4.4.1 Mesh dependence

In the next graph the mesh dependence is illustrated. The cases have mesh sizes of 2 cm and 1.5 cm. The mesh dependence is evaluated on the On-design condition (TSR=6).

The pressure and the velocity, in Fig.4.25 and Fig.4.26, are plotted along the wind tunnel centerline.

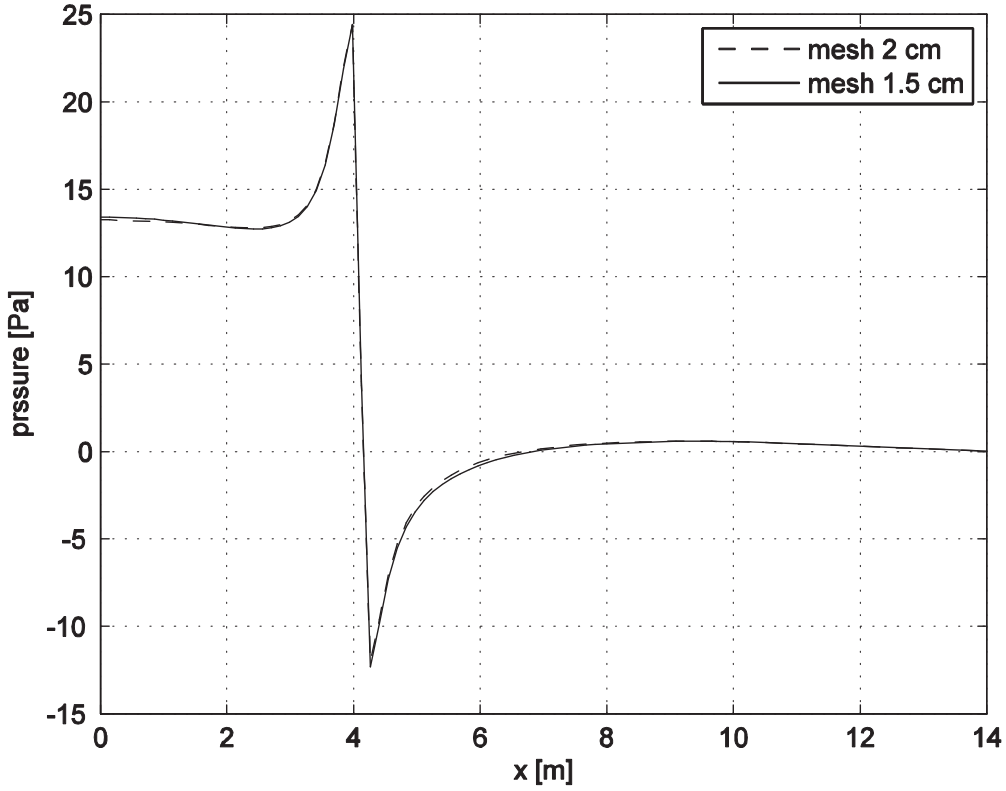

Fig.4.25 Pressure profiles along the centerline, TSR=6, mesh dependence, n 30

In Fig.4.25 we can observe that with a 2 cm mesh we already have reached a good asymptotic condition, and that there is virtually no variation with the 1.5 cm case. The step at the disk level is obviously due to the force assigned to the mesh elements making up the disc. From $x = 9$ the pressure starts to slightly decrease. This is probably due to the boundary layer developing on the wind tunnel walls, which creates a friction. This is the typical phenomenon that can be observed in any pipe, with the name of friction loss: the wind tunnel can be considered as a large and short pipe characterized by a small friction loss, which needs a pressure gradient to be overcome.

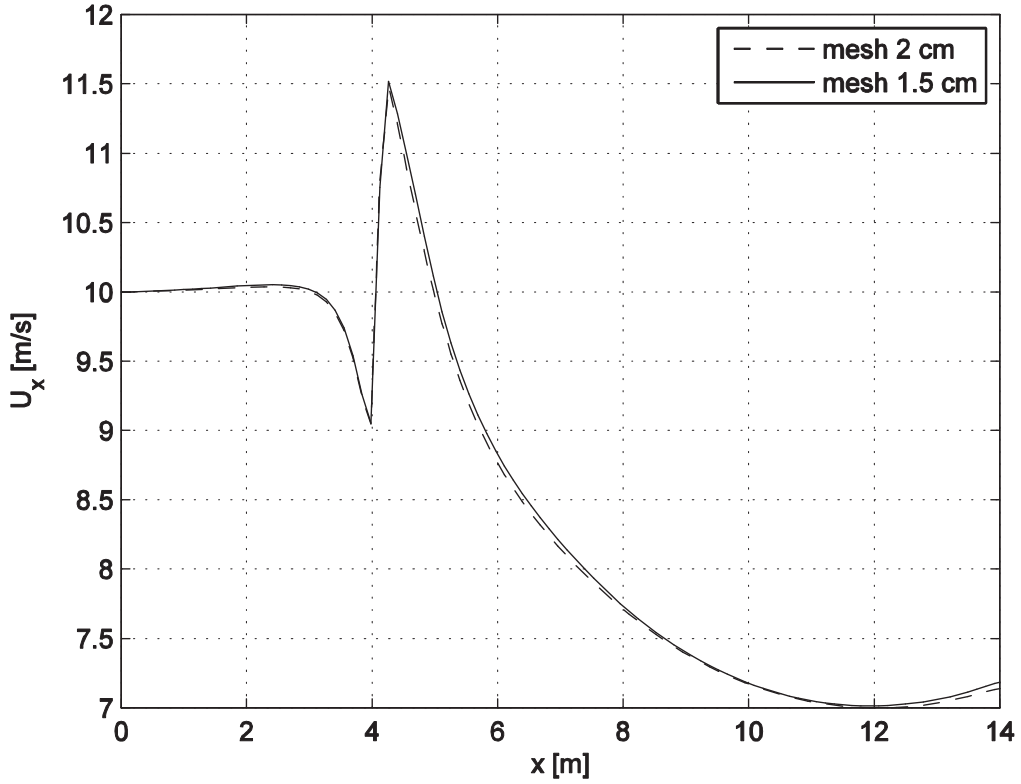

Fig.4.26 **Axial speed profiles along the centerline, TSR=6, mesh dependence, n 30**

In Fig.4.26, the 2cm mesh has already reached the asymptotic condition, as also observed in Fig.4.25. The flow slows down for the presence of the disk but at the disk level it has a sudden acceleration because the centerline flow does not meet the blades and the nacelle is not modeled. The nearby flow meets the blades and must slow down, so the flow at the turbine centerline accelerates. After the disk, for the effect of the turbulent diffusion, the wake spreads and the flow on the centerline slows down. After $x = 12\,m$, we can note that the flow starts to accelerate, this is probably due to the wake spread.

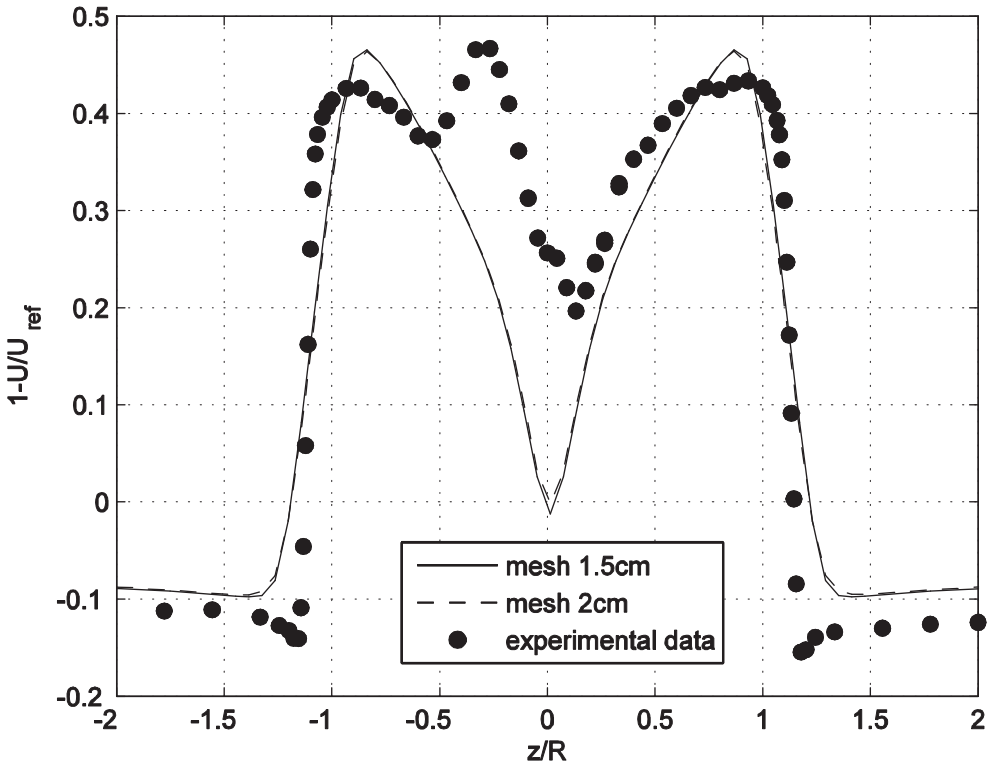

Fig.4.27 Mean velocity profiles along a horizontal line X/D=1, TSR=6, mesh dependence, n 30

As for the non-dimensional velocity on a horizontal diagonal, from Fig.4.27, the 2cm mesh is sufficiently accurate. The central dip reaches 0 because the line is very close to the disk and the wake has not diffused, yet. Obviously the experimental dip is less deep because of the presence of the nacelle. We can also note that the numerical model slightly overestimates the peaks.

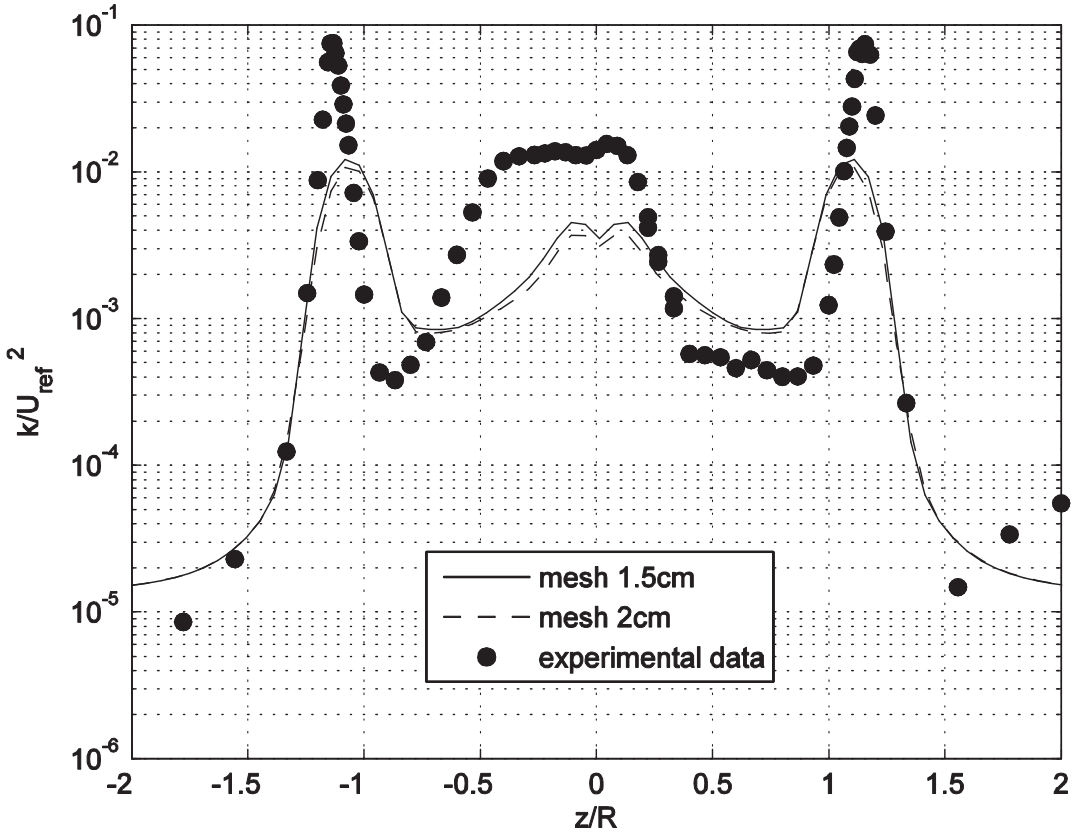

Fig.4.28 Turbulent kinetic energy profiles along a horizontal line X/D=1, TSR=6, mesh dependence, n 30

Also for Fig.4.28 the 2 cm mesh is enough accurate: The peaks are predicted in the right position, but their height is underestimated.

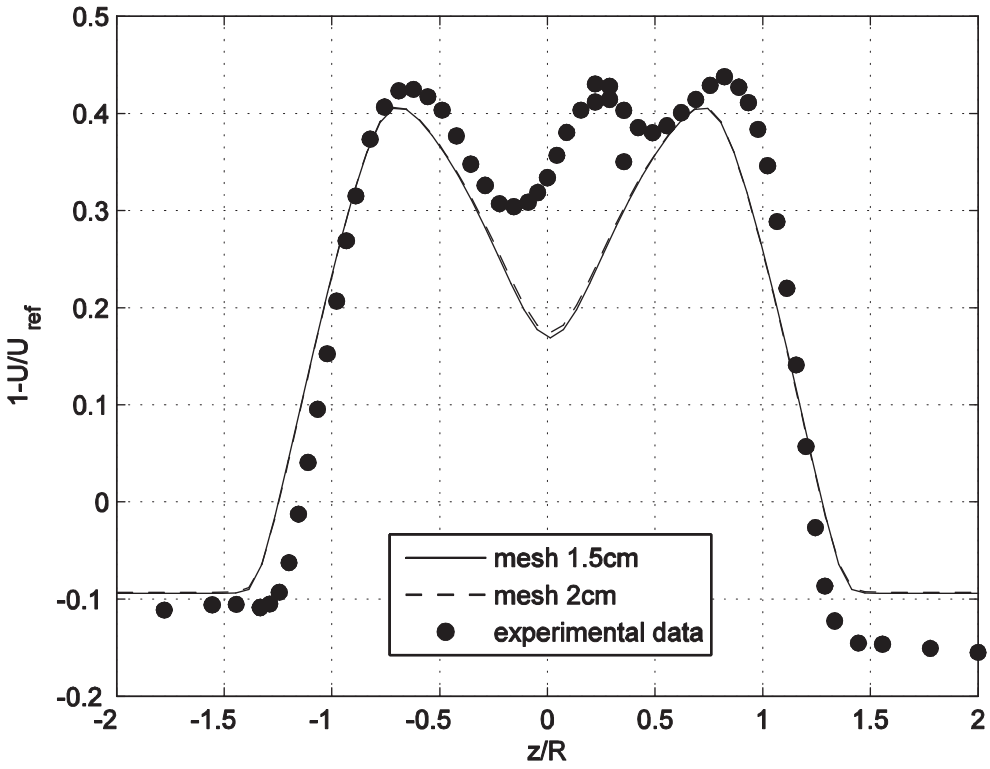

Fig.4.29 Mean velocity profiles along a horizontal line X/D=3, TSR=6, mesh dependence, n 30

Also Fig.4.29 the 2 cm mesh is enough accurate. At 3 diameters the wake is starting to diffuse more intensely: the two peaks drop to 0.4 while the centerline velocity increases to 0.7.

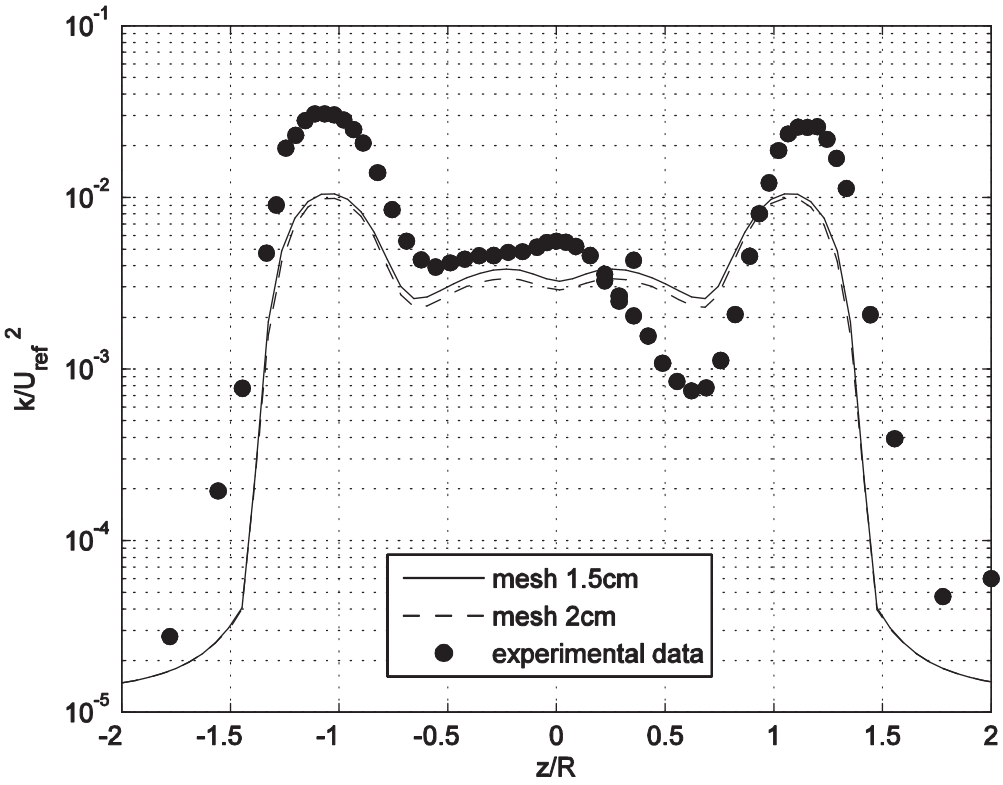

Fig.4.30 Turbulent kinetic energy profiles along a horizontal line X/D=3, TSR=6, mesh dependence, n 30

Also in Fig.4.30 the 2 cm mesh results sufficiently accurate. The diffusion reduces the height of the turbulence peaks size , and the error by the simulation is reduced. The central part of the wake is well simulated except for the asymmetry that the code is not able to predict.

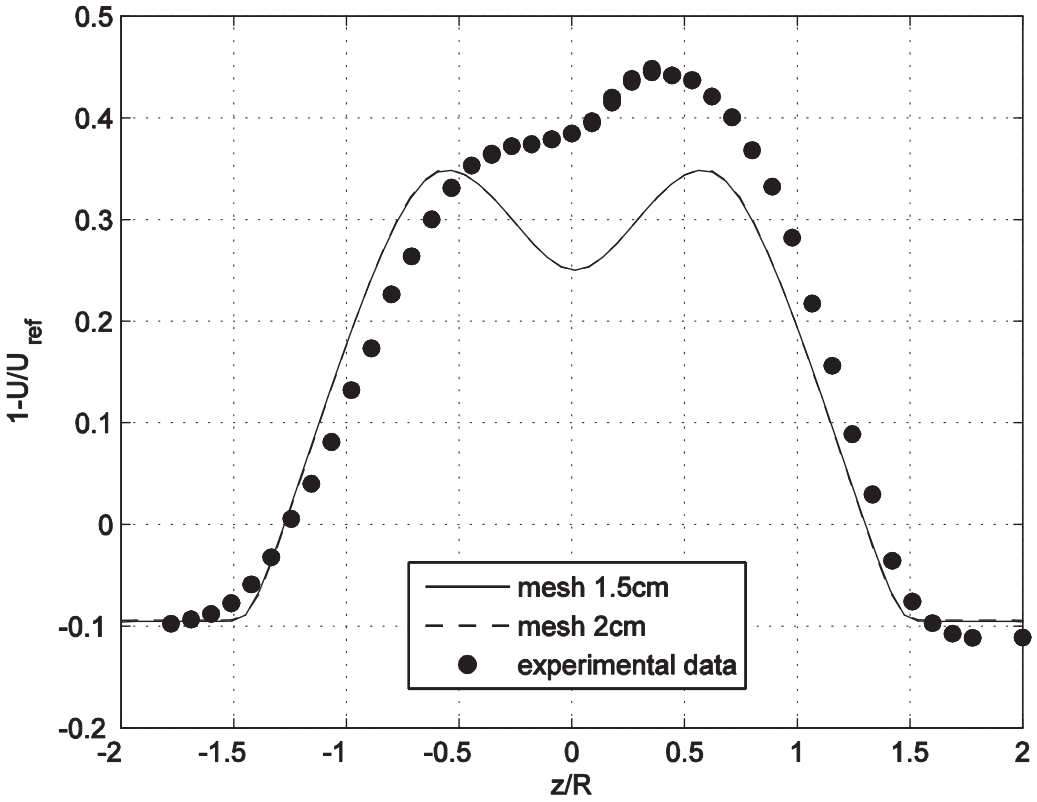

Fig.4.31 Mean velocity profiles along a horizontal line X/D=5, TSR=6, mesh dependence, n 30

Also in Fig.4.31, the experimental data shows that at 5 diameter distance the wake turbulent diffusion merges the two peaks in one. Even though the computational model shows a good agreement, it still features two peaks instead of a smooth profile. This difference is probably due to the nacelle presence that increases the centerline velocity deficit with respect to the numerical simulations.

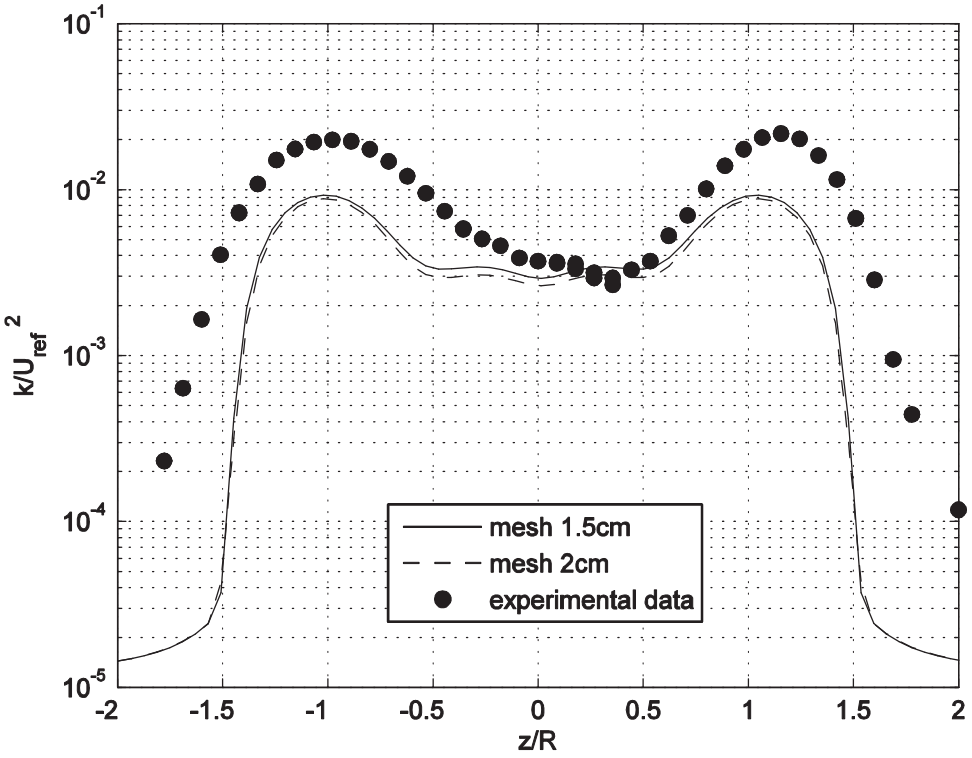

Fig.4.32 Turbulent kinetic energy profiles along a horizontal line X/D=5, TSR=6, mesh dependence, n 30

The peaks continue to decrease and together also the error: the numerical peaks are half of the real peaks. However at this disk distance my model underestimates the wake width: the numerical width is around 3R whereas the experimental data show a wake around 3.5 R.

In conclusion the 2 cm mesh can be consider enough accurate, hence in the next analysis we will use a 2 cm mesh.

4.4.2 Off-design condition

Now we will focus on the off-design behavior predictions, and compare them with wind tunnel experimental data.

4.4.2.1 TSR 3

In this condition the intersection of the blades are stalled, while the outer regions work at high angle of attack, see for example the analysis from Krogstad and Lund [20].

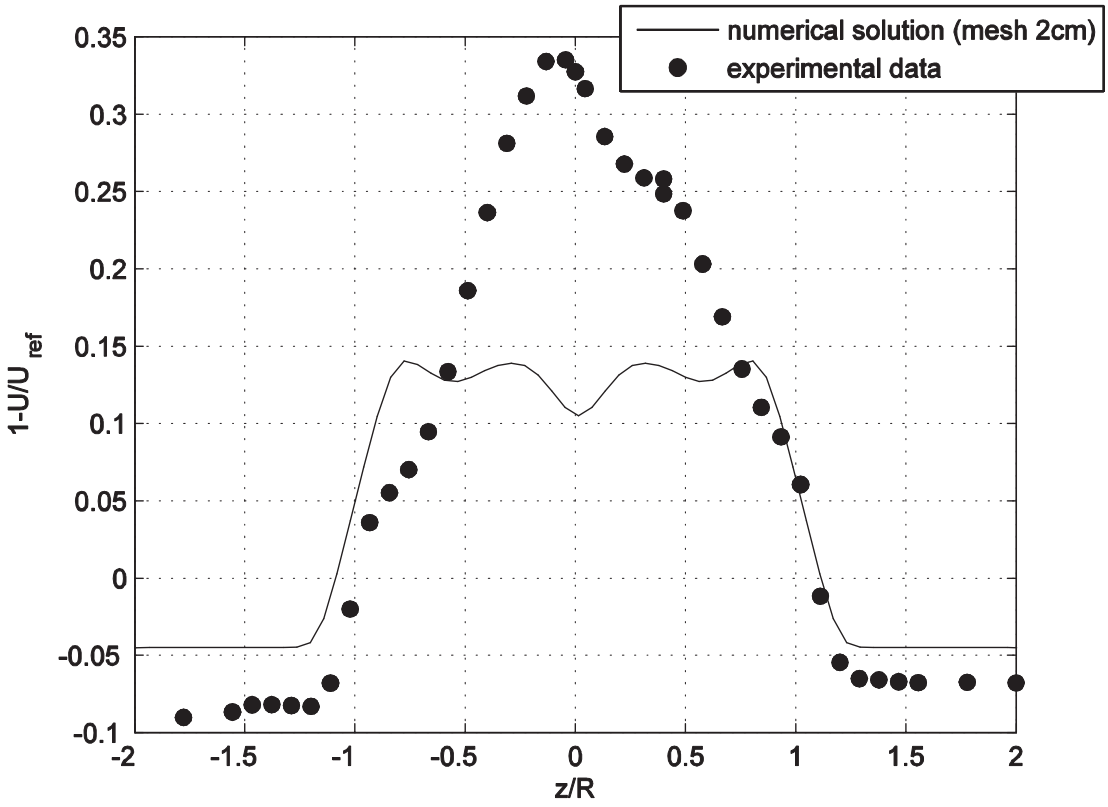

Fig.4.33 Mean velocity profiles along a horizontal line X/D=3, TSR=3

From Fig.4.33 we can note that the numerical model is not able to predict the wake at the rotor centre, meaning that the stall is overpredicted. Also, at low TSR, the contribution of the tower drag in the wake generation is quite relevant, due to the low thrust on the turbine rotor. The thrust of the rotor is underestimated, the blockage is lower than the reality and hence the flow around the disc is slower.

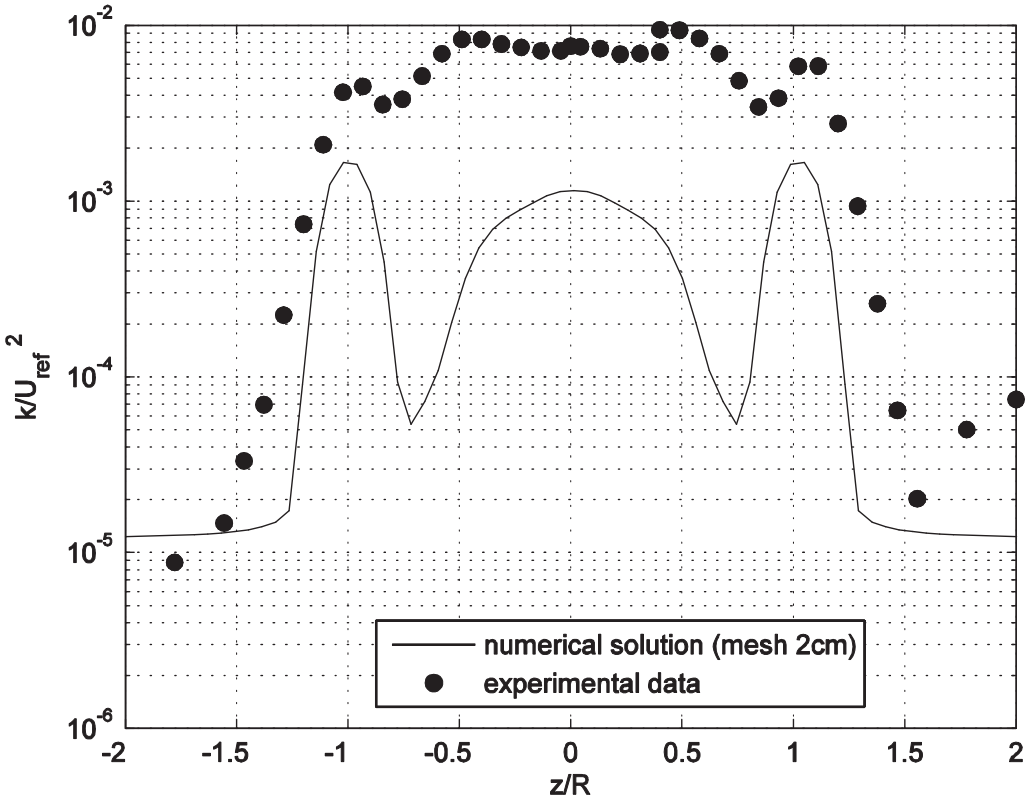

Fig.4.34 Turbulent kinetic energy profiles along a horizontal line X/D=3, TSR=3

We can observe from Fig.4.34 that the experimental data show an almost constant level of turbulent kinetic energy in the wake. This is due to the boundary layer that is separated along the blade, which produces a remarkable amount of kinetic energy. The peaks due to the tip vortices and to the turbulence in the shear layer are reduced than at design conditions. The profile obtained by the numerical code is not able to give a correct prediction.

4.4.2.2 TSR 10

In this conditions, the tangential velocity becomes predominant, so the outer regions of the blades work a low angle of attack. The airfoils located at low radii work at negative angles of attack, implying that these sections do not extract energy from the flow but work like a propeller.

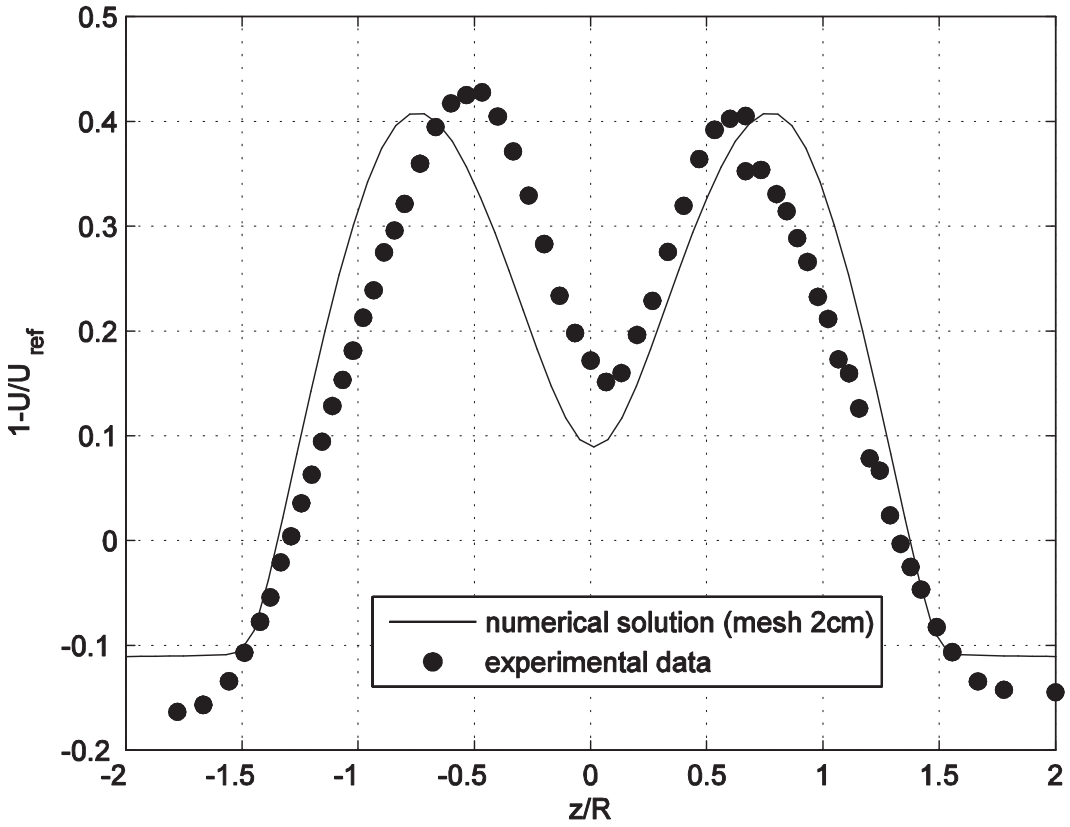

Fig.4.35 Mean velocity profiles along a horizontal line X/D=3, TSR=10

The numerical model is able to give a very good prediction. The central dip is deeper than at TSR 6, due to the energy being transferred to the flow in the central part of the disk. On the velocity profile (here not reported) for X/D=1 the centerline velocity deficit reaches a negative value. At the distance of X/D=3 the turbulent diffusion reduces the negative peak depth. Also for the experimental data the acceleration given by the inner sections of the rotor implies that the central peak, which was present at TSR=6, disappears.

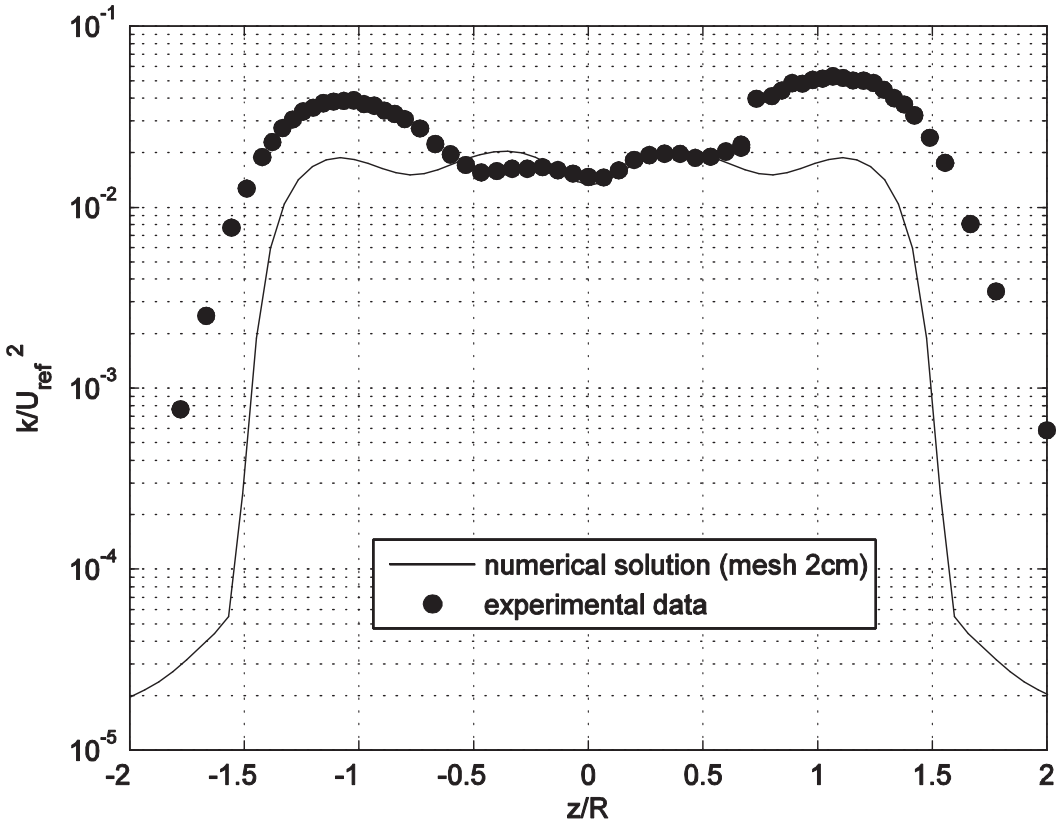

Fig.4.36 Turbulent kinetic energy profiles along a horizontal line X/D=3, TSR=10

Also the turbulent kinetic energy profile at TSR=10 agrees quite well with the experimental results. The production of turbulent kinetic energy from the tip vortices become comparable to that produced for boundary layer effect, there is a little difference of TKE between the centre and the edges of the wake. the turbulent kinetic energy reaches high values $5 \cdot 10^{-2}$. However the numerical model underestimates the wake width.

4.4.3 Horizontal vs Vertical

So far the characteristic (speed and turbulent kinetic energy) were plotted on a horizontal line. In the next graphs we overlap the profiles along a horizontal line with the profile along a vertical line. For the numerical solution we expect a symmetric profile also along the vertical line, since the disk center is placed exactly in the middle of the wind tunnel. For the experimental profile we expect a slight asymmetry for the presence of the nacelle and the tower and because in reality the turbine hub height is slightly below the wind tunnel centerline.

The plots are related to design condition, for three downstream distances: X/D=1, X/D=3, X/D=5

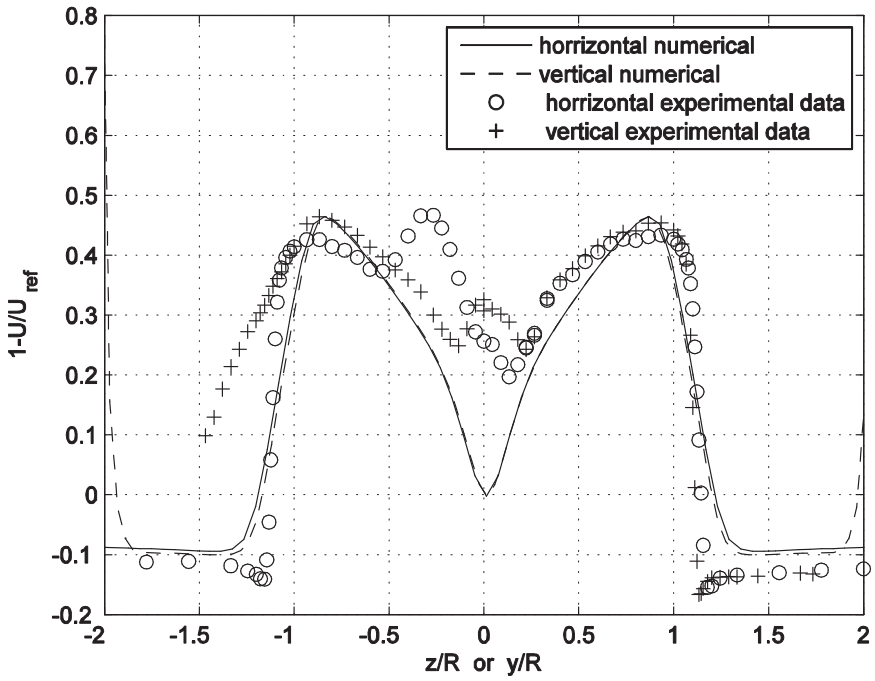

Fig.4.37 Mean velocity profiles at X/D=1, along a horizontal line and along a vertical line

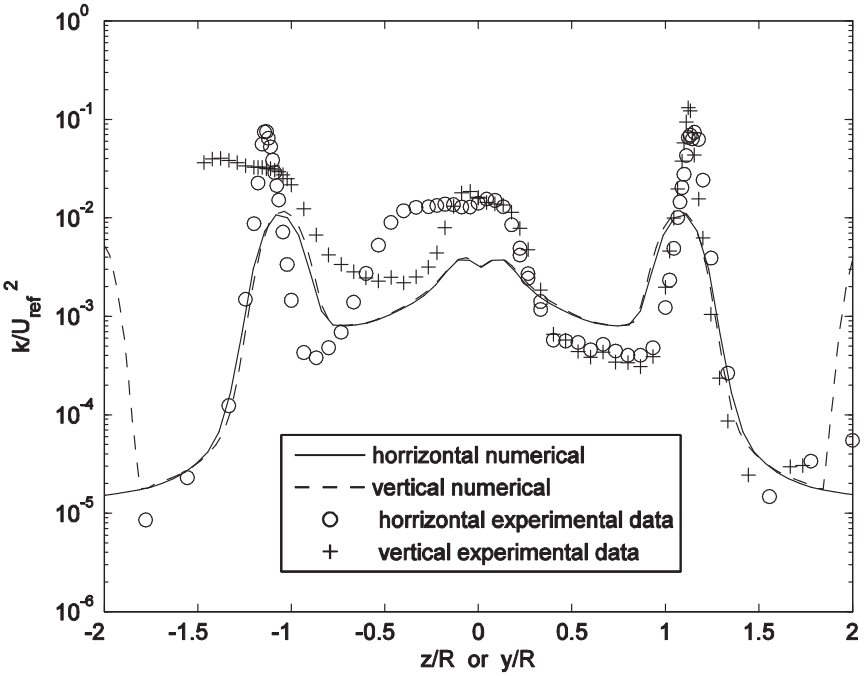

Fig.4.38 **Turbulent kinetic energy profiles at X/D=1, along a horizontal line and along a vertical line**

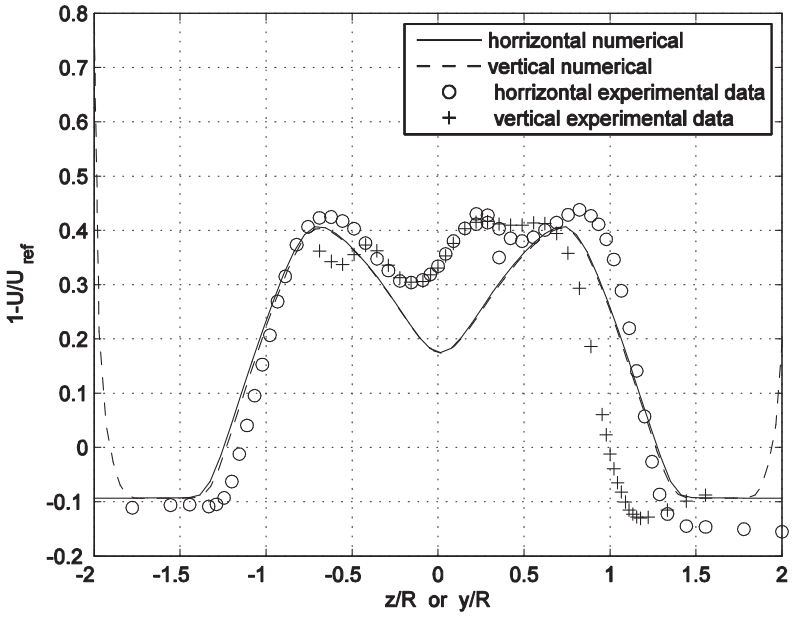

Fig.4.39 **Mean velocity profiles at X/D=3, along a horizontal line and along a vertical line**

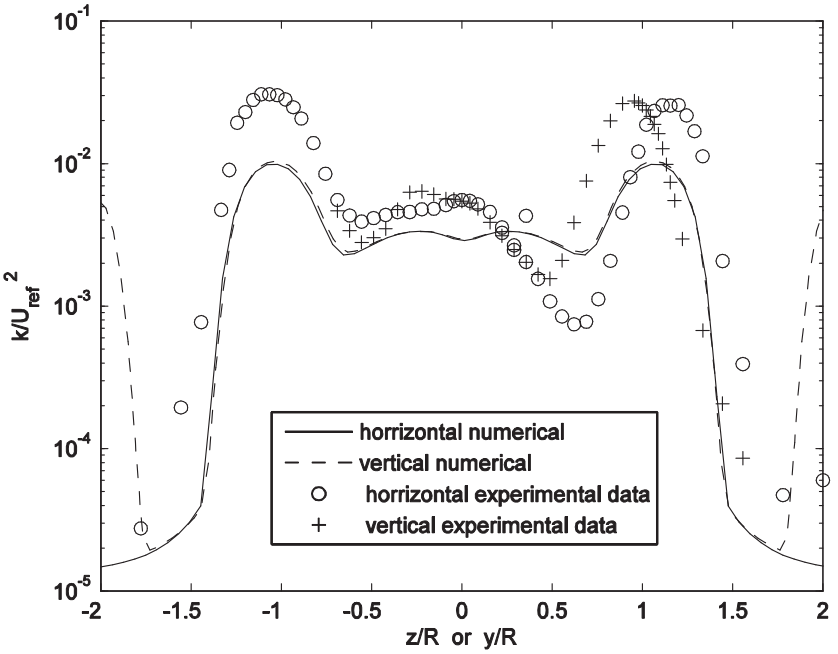

Fig.4.40 **Turbulent kinetic energy profiles at X/D=3, along a horizontal line and along a vertical line**

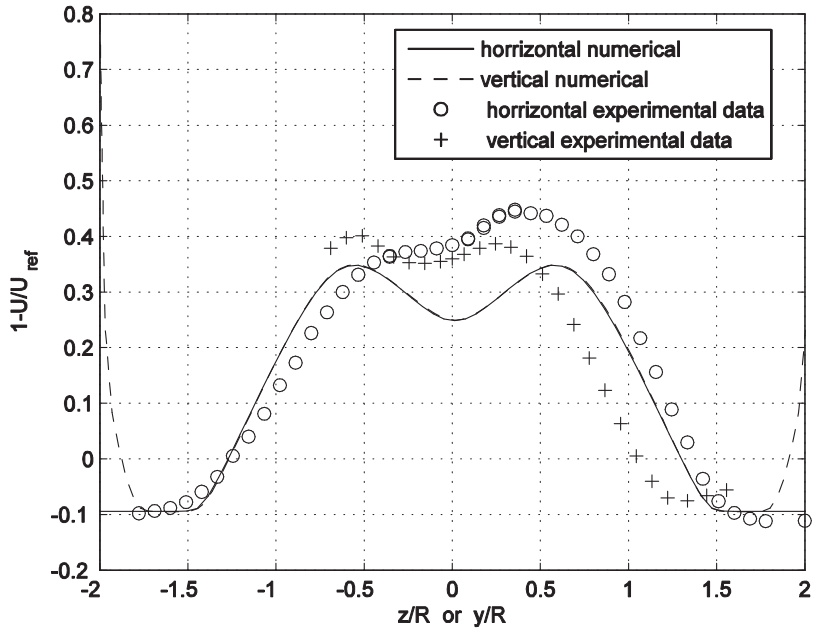

Fig.4.41 **Mean velocity profiles at X/D=5, along a horizontal line and along a vertical line**

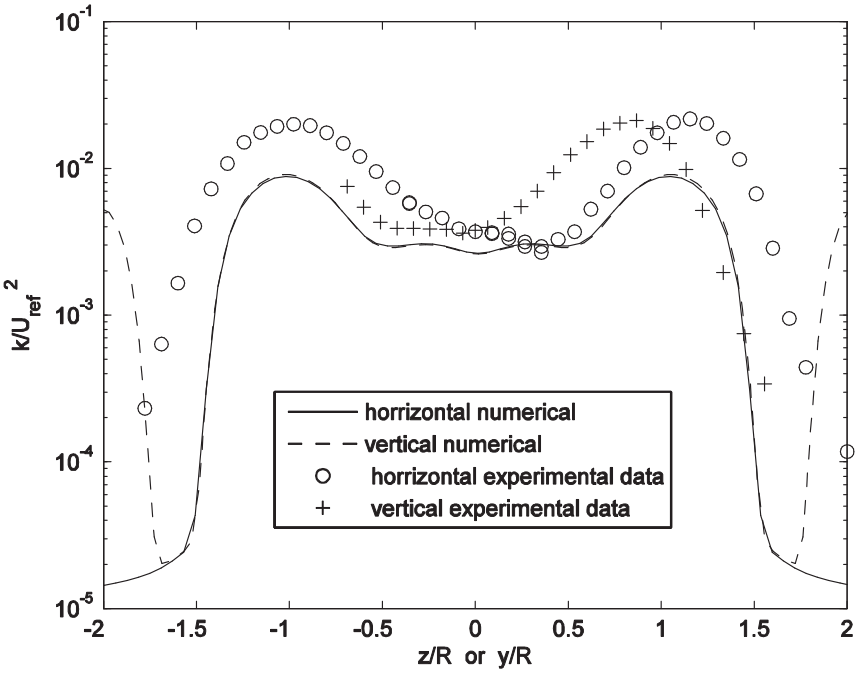

Fig.4.42 Turbulent kinetic energy profiles at X/D=5, along a horizontal line and along a vertical line

From Fig.4.37, Fig.4.38, Fig.4.39, Fig.4.40, Fig.4.41, Fig.4.42 we note that the horizontal and vertical profile of the numerical code are almost superimposed, while the experimental profiles are quite different. The lateral peaks of the vertical numerical profile are due to the top and ground walls presence. If the z-axis was extended, also the horizontal numerical results would have similar peaks. Furthermore we note that the difference between the horizontal and the vertical profile obtained with the code is greater near the disc and it decreases far from the disc.

From the experimental data we can note that the horizontal profiles are characterized by a greater symmetry than the vertical profiles because the rotor is placed in the centre of the horizontal direction but it is not placed in the centre of the wind tunnel height. The profile along the vertical line shows asymmetry also in the position of the principals peaks, this asymmetry is greater far from the disc. From Fig.4.37 we note that for negative y/R the vertical profile obtained from experimental data shows a lower velocity, this is probably due to the presence of the tower.

The case tested with the numerical code places the rotor in the centre of the wind tunnel height, this geometrical difference, between real case and simulation, is probably the reason of the worse matching between experimental data and numerical data along the vertical lines than along the horizontal lines.

4.5 TSR constant vs Ω constant

In this section we compared the result so far obtained with the code version at TSR constant with those obtained with the code version at Ω constant. All the following analyses are executed with 30 blade elements and a 2 cm mesh.

We started by showing the outputs of the turbine performance that we obtained with the version with constant TSR and with the constant Ω version.

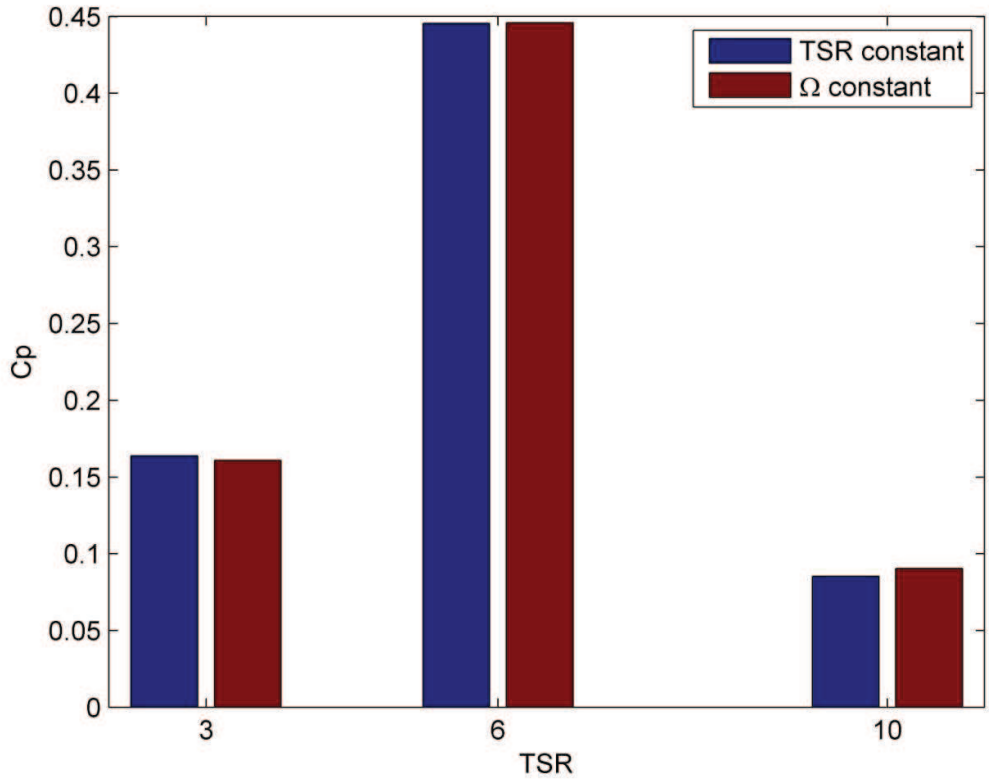

Fig.4.43 Power coefficient on-design and off-design, TSR constant and Ω constant

From Fig.4.43 we can see that the influence on the C_P is very low. For on-design conditions the difference is negligible, while for low TSR the with constant TSR gives a slightly higher C_P. For high TSR the constant Ω version gives a greater value of the C_P.

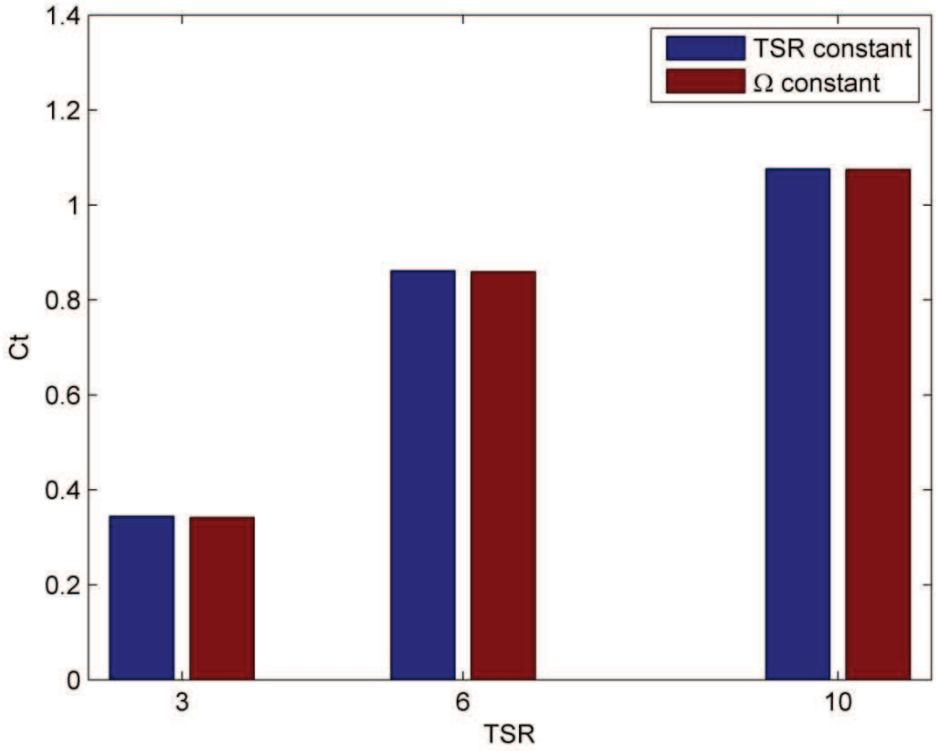

Fig.4.44 Thrust coefficient on-design and off-design, TSR constant and Ω constant

For the thrust coefficient the choice of the version is non influential in on-design as well as off- design condition.

Before analyzing the wake, we show the velocity profile at the centerline, which is important to understand the difference in the two code versions.

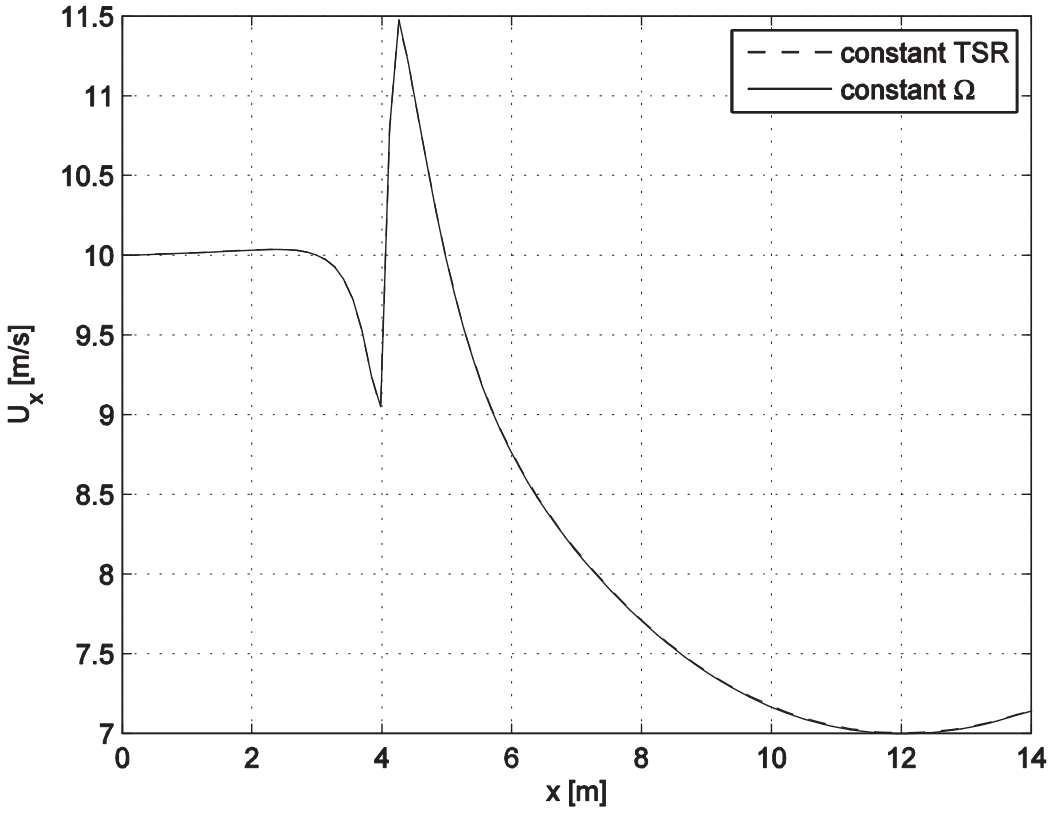

Fig.4.45 Axial speed profiles along the centerline, TSR=6, TSR constant and Ω constant

From Fig.4.45 we can note that the velocity at the wind tunnel inlet, fixed by boundary condition to 10 m/s, is different from the velocity used by the BEM algorithm to calculate the upstream velocity, for which OpenFOAM takes the velocity at $x = 2\,m$. This velocity is slightly higher because of the centerline velocity increase due to the boundary layer developing on the wind tunnel walls: the flow is incompressible so the velocity at the centerline must increase. From this plots we can anyway note that this speed difference is almost imperceptible, hence the results obtained with the two versions are almost the same.

In the next graphs we compared the profile obtained with the constant TSR version with those obtained with constant Ω.

4.5.1 TSR 6

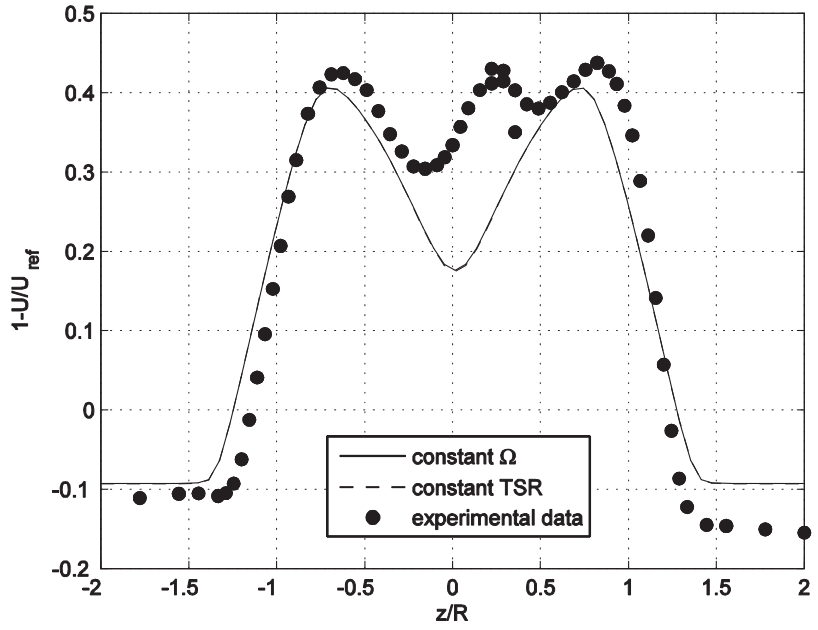

Fig.4.46 Mean velocity profiles along a horizontal line X/D=3, TSR=6, TSR constant and Ω constant

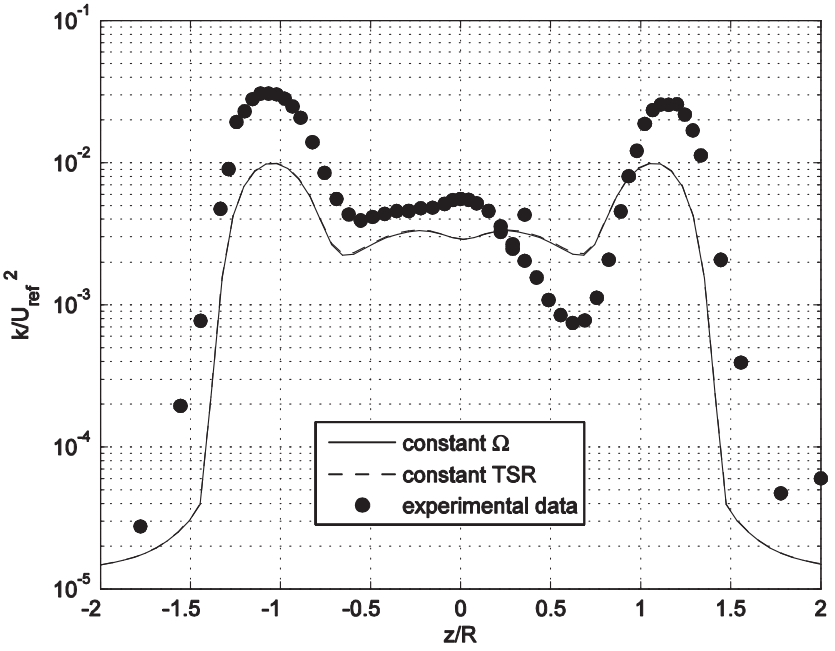

Fig.4.47 Turbulent kinetic energy profiles along a horizontal line X/D=3, TSR=6, TSR constant and Ω constant

4.5.2 TSR 3

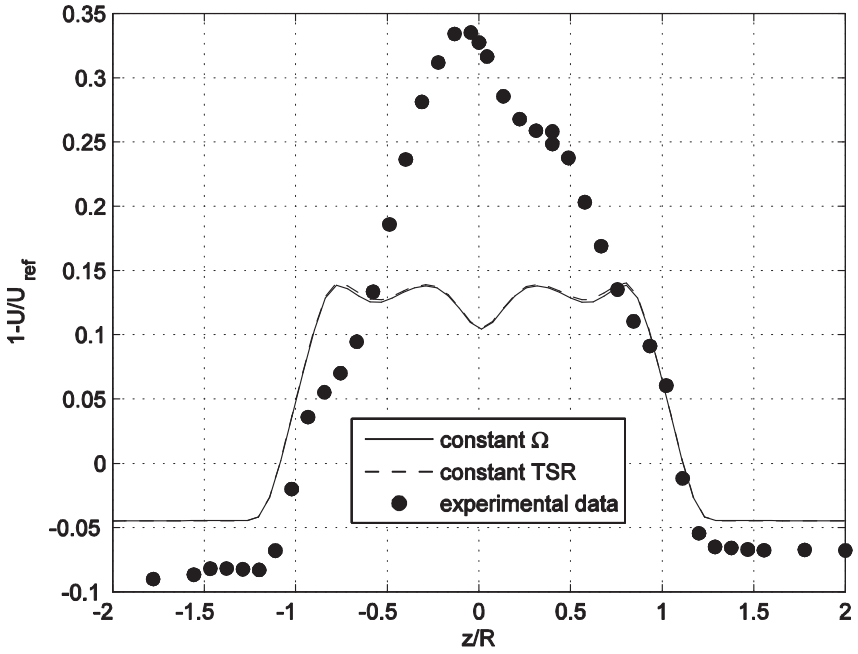

Fig.4.48 **Mean velocity profiles along a horizontal line X/D=3, TSR=3, TSR constant and Ω constant**

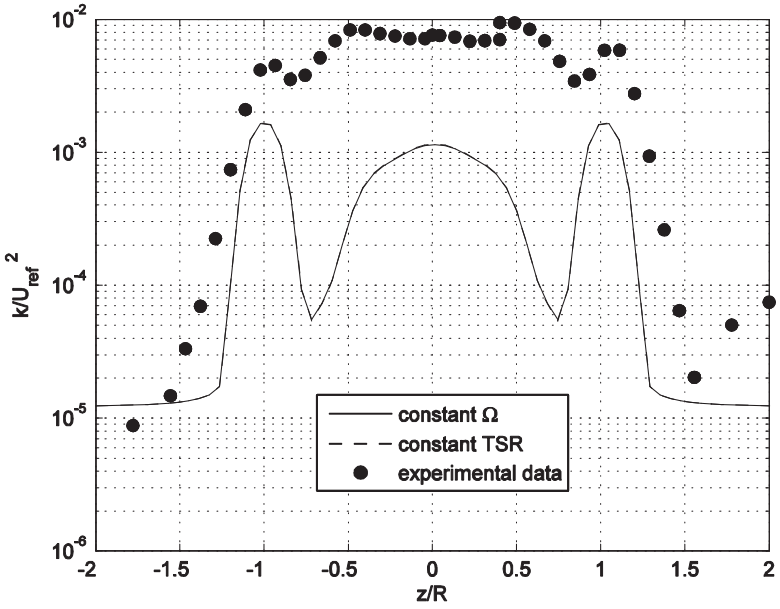

Fig.4.49 **Turbulent kinetic energy profiles along a horizontal line X/D=3, TSR=3, TSR constant and Ω constant**

4.5.3 TSR 10

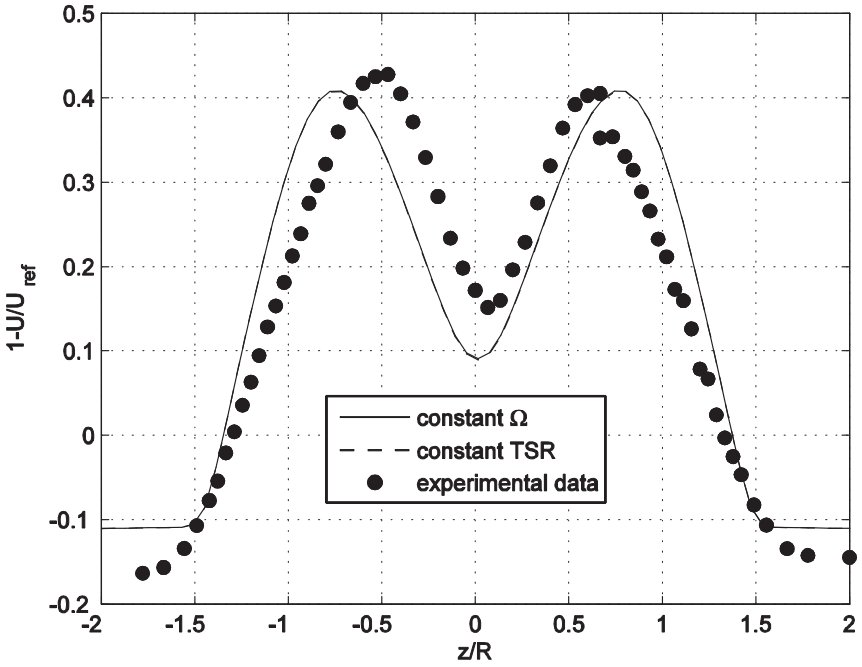

Fig.4.50 **Mean velocity profiles along a horizontal line X/D=3, TSR=10, TSR constant and Ω constant**

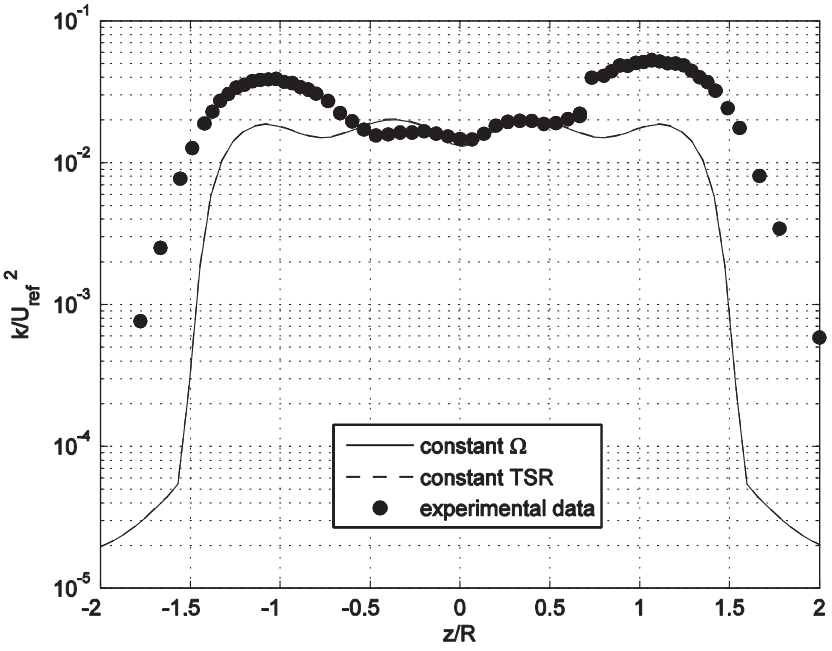

Fig.4.51 **Turbulent kinetic energy profiles along a horizontal line X/D=3, TSR=10, TSR constant and Ω constant**

In all the analyzed setups, there is a very little change in the two program versions. We aspect more difference for the off-design cases because they are characterized by a greater difference of the C_P obtained with the two versions, in fact the only graph where we can note a slightly difference in the profiles is Fig.4.48 (TSR=3).

4.6 Actuator Disk with BEM vs simple Actuator Disk

In section 3.2 and 3.3 we illustrated how the simple Actuator Disk and the Actuator Disk with BEM work, highlighting the greater complexity of the Actuator Disk with BEM. Moreover, at the beginning of this section, we noted the necessity for a fine enough mesh which is able to keep up with the blade discretization, hence the actuator disk with BEM is characterized by greater computational cost. In the light of this greater complexity and computational cost, we expect more accurate results. In this section we compared the wake profiles obtained with the simple actuator disk with the actuator disk with BEM and the experimental data.

As input in the simple actuator disk, we used the C_P and C_T evaluated with the BEM code (see section4.1).

The 2 cm mesh was used for both simulations, while in the actuator disk with BEM the blade was divided into 30 elements.

4.6.1 TSR 6

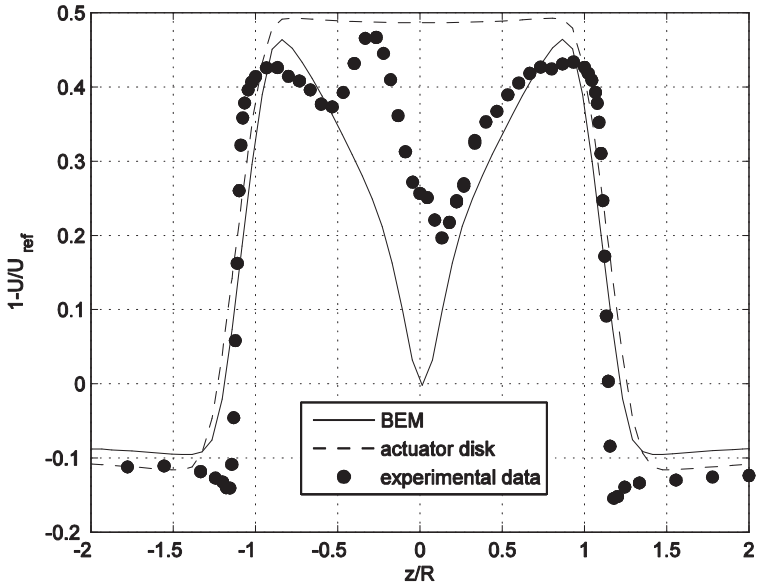

Fig.4.52 Mean velocity profiles along a horizontal line X/D=1, TSR=6, by simple actuator disk, BEM and experimental data

From Fig.4.52 we can note that the simple actuator disk is not able to predict the typical V-shape of the wake, but is characterized by an almost constant value for the all wake

width. This velocity profile is characteristic of the simple actuator disk for all distances and all for working condition. From this figure we can note that the peaks at the disk edge are overestimated by both the actuator disk models, but the one with BEM is closer to the experimental data.

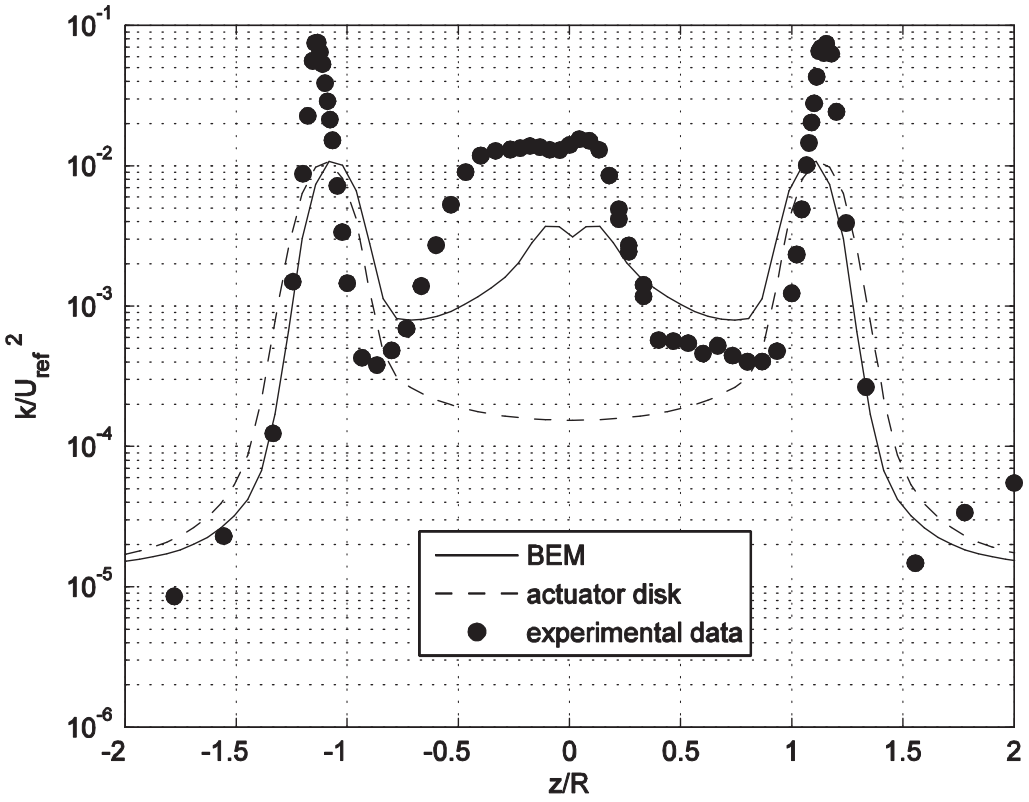

Fig.4.53 Turbulent kinetic energy profiles along a horizontal line X/D=1, TSR=6, by simple actuator disk, BEM and experimental data

From Fig.4.53, describing the turbulent kinetic energy at X/D=1 at TSR=6, we note that the two peaks on the disk edges are equally captured by the two actuator disk models, and both underestimate them. The velocity profile predicted by the simple actuator disk presents a deep dip between the two peaks. The turbulent kinetic energy is in fact zero where there are no velocity gradients: inside the wake of the simple actuator disk the velocity (as we saw in figure Fig.4.53) is almost constant and so the turbulent kinetic energy is only approximately $1.5 \cdot 10^{-4}$.

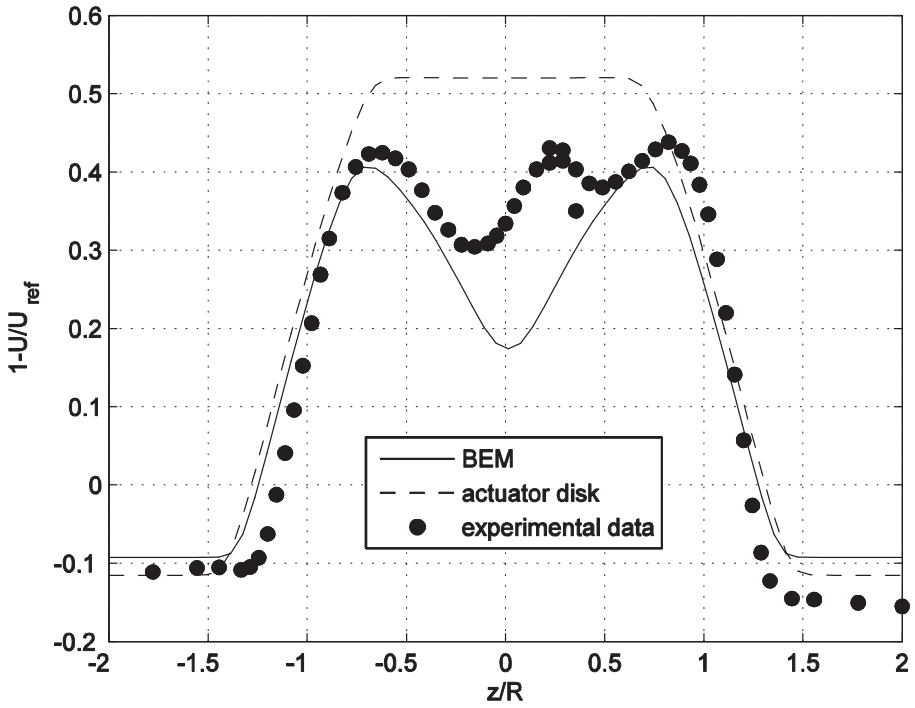

Fig.4.54 Mean velocity profiles along a horizontal line X/D=3, TSR=6, by simple actuator disk, BEM and experimental data

From Fig.4.54 we note the constant shape for the simple actuator disk, different from X/D=1 because now the profile is completely constant, because close to the disk the streamlines are curved and this implies a changing in the velocity whereas far from the disk the streamline are parallel. Furthermore error on the peak height is bigger. The wake width is anyway very well captured by both models.

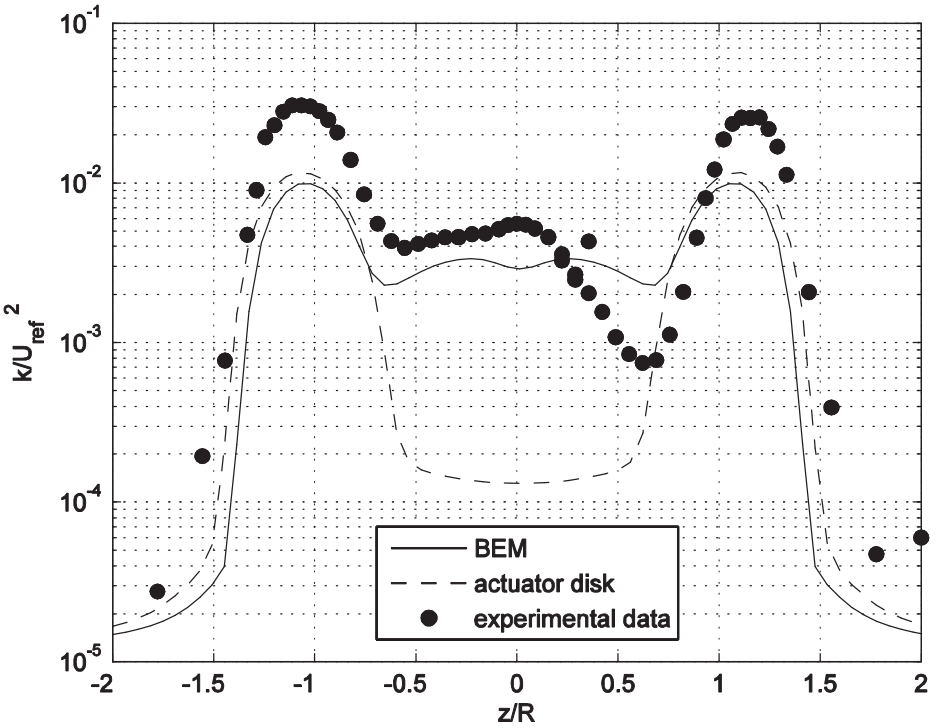

Fig.4.55 Turbulent kinetic energy profiles along a horizontal line X/D=3, TSR=6, by simple actuator disk, BEM and experimental data

The more constant speed profile at X/D=3 implies lower turbulent kinetic energy values for the simple actuator disk ($1.3 \cdot 10^{-4}$ in the center). The two lateral peaks are slightly better captured by the simple actuator disk (around +15 % the increase of the peaks height), it also give a more correct wake width (approximately +5 % the increase of width).

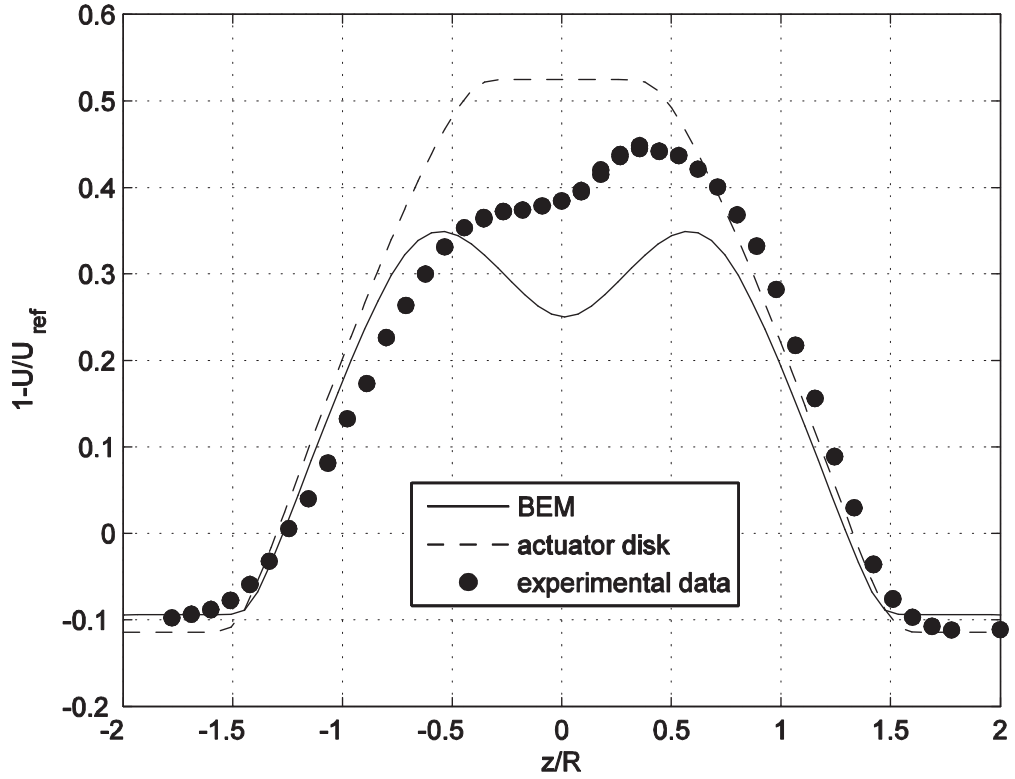

Fig.4.56 Mean velocity profiles along a horizontal line X/D=5, TSR=6, by simple actuator disk, BEM and experimental data

At this distance from the disk we note that the turbulent diffusion reduced the size of the zone with constant velocity, characterizing the center of the wake predicted by the simple actuator disk profile.

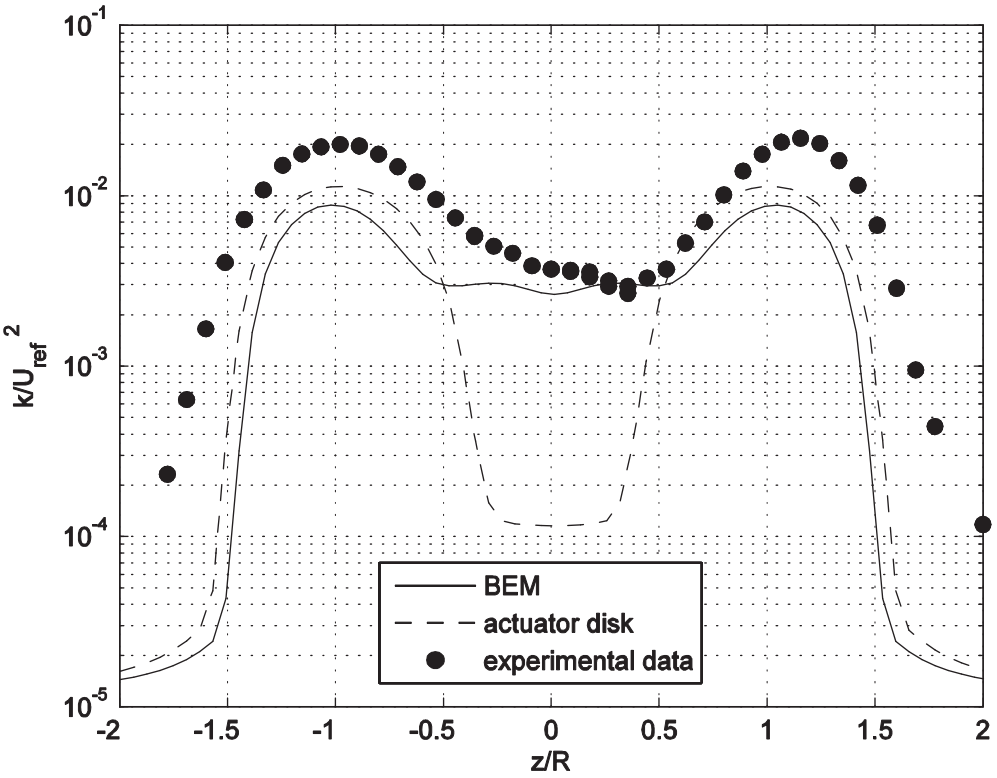

Fig.4.57 Turbulent kinetic energy profiles along a horizontal line X/D=5, TSR=6, by simple actuator disk, BEM and experimental data

At exception of the central dip the simple actuator disk predict slightly better the peaks height and the wake width. The central dip is due to the constant velocity profile in the centre of the wake, that continue to be in spite of the diffusion.

4.6.2 Off-design condition

As reported in the section dedicated on the methodology, we know that the simple actuator disk does not use the input C_T but recalculates a new C_T using also the input C_P. The recalculation is done using relations based on the simple momentum model without rotation, without Pradtl's correction and without the correction for high axial induction factor. In the analysis at design conditions this relations are quite good, but at off-design conditions they do not fit. Hence we expect that the thrust that the simple actuator disk assigns to the cells inside the cylinder is incorrect, so the wake that we obtain is also very different from the real wake.

4.6.2.1 TSR 3

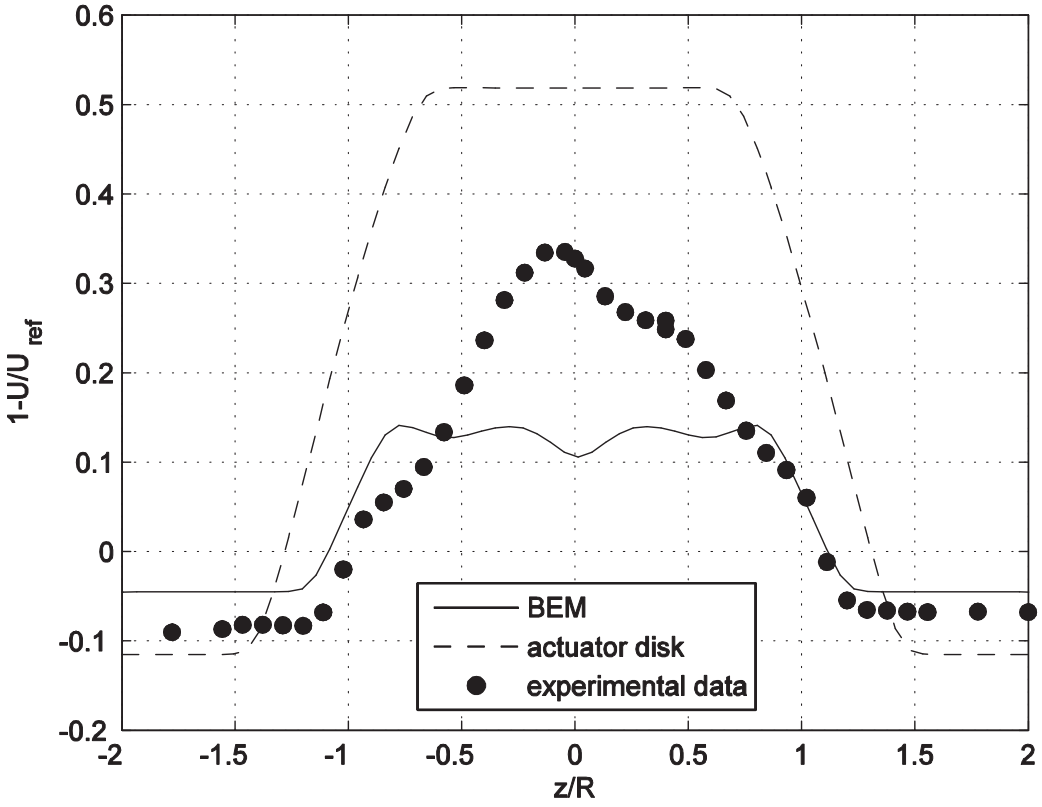

Fig.4.58 Mean velocity profiles along a horizontal line X/D=3, TSR=3, by simple actuator disk, BEM and experimental data

The simple actuator disk produces a velocity profile which completely different from reality, the lateral peaks height (they exceed 0.5) and the wake width are wrong (approximately 3).

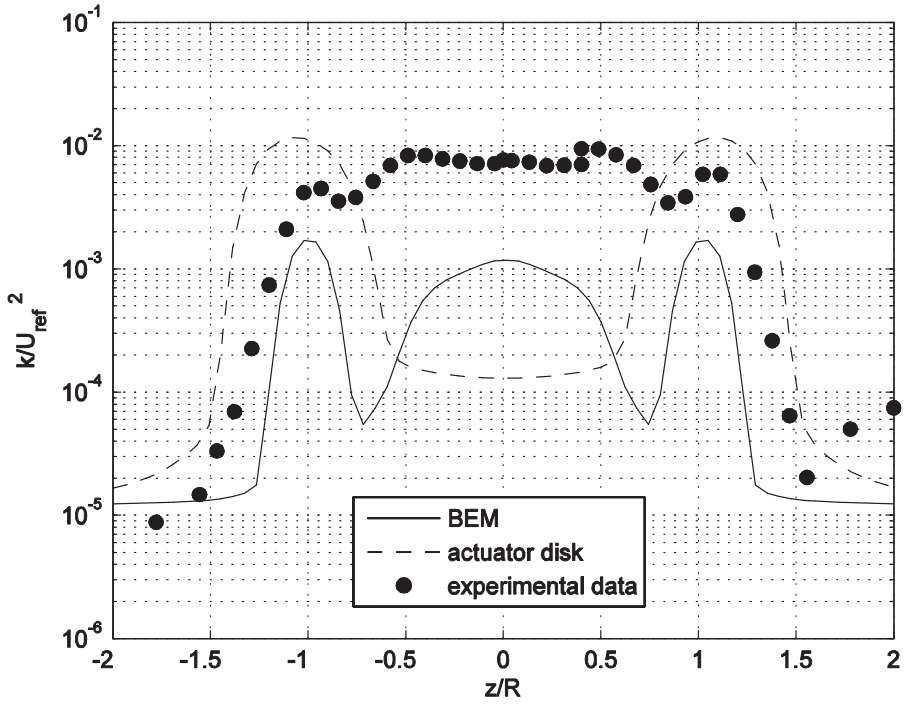

Fig.4.59 Turbulent kinetic energy profiles along a horizontal line X/D=3, TSR=3, by simple actuator disk, BEM and experimental data

Both the actuator disk are not able to predict the turbulent kinetic energy profile for low TSR. The simple actuator disc overestimates the peaks heights (approximately the double) and underestimates the central wake of almost two orders of magnitude. The actuator disc with BEM underestimates everywhere.

4.6.2.2 TSR 10

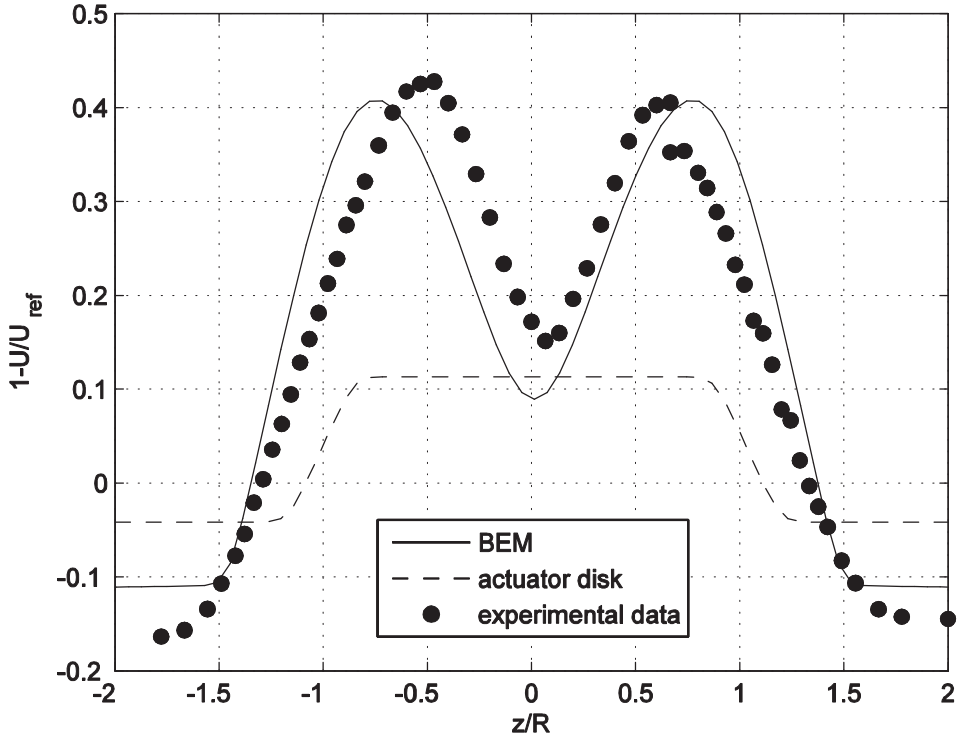

Fig.4.60 Mean velocity profiles along a horizontal line X/D=3, TSR=10, by simple actuator disk, BEM and experimental data

From Fig.4.60 we can note that the actuator disk underestimates completely the wake intensity. With a low blockage effect due to a low thrust, the flow around the wake accelerates less. We expected a considerable error for the simple actuator disc at TSR=10, because for high values of axial induction factor the simple actuator disc model is no longer valid, it requires a empirical correction that in the simple actuator disc, presented in OpenFOAM, is not implemented.

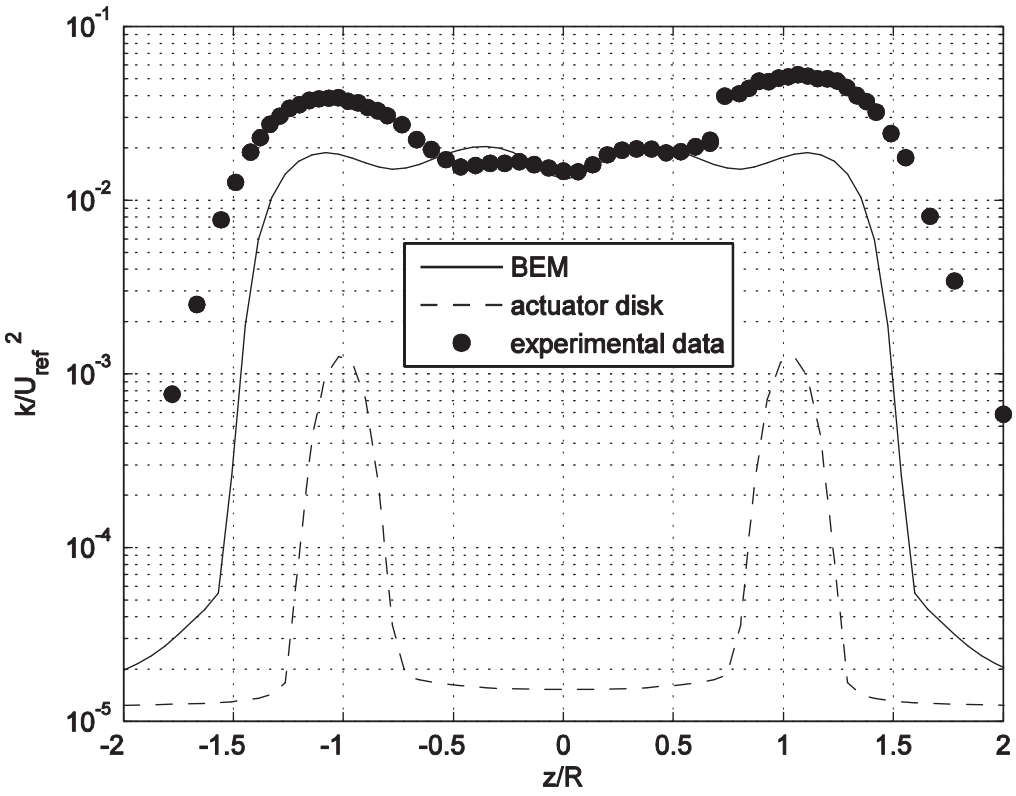

Fig.4.61 Turbulent kinetic energy profiles along a horizontal line X/D=3, TSR=10, by simple actuator disk, BEM and experimental data

Our models generally underestimate the turbulent kinetic energy level, maybe for effect of the turbulent model used. In this case the simple actuator disk underestimates severely (approximately 3 order of magnitude in the centre and approximately 13 times the peaks values) the speed profile, due to a wrong assignment of the thrust: the result is a strong underestimation of the turbulent kinetic energy.

These last four figures show us what we mentioned before: the simple actuator disk is completely inappropriate to describe a wind turbine in off-design conditions. The simple actuator disk gives us better result at design conditions. However also in this condition the actuator disk with BEM offers us a better wake description.

4.7 Turbine vs Drag disc

In the previous section the simple actuator disc and the actuator disc model were compared with the experimental data obtained from a wind turbine. In this section we want to analyze whether the computational model is more close to predict a wind turbine or a Drag Disc.

In this section we compare the wake profiles obtained with the simple actuator disk, with the actuator disk with BEM, the simple Jensen model, the experimental data by the wind turbine and the experimental data in the wake of the Drag disc. These comparisons are performed at TSR=6 because in this condition the wind turbine has the same C_T of the Drag Disc, as we can observe from Fig.4.8. A 2 cm mesh was used for both simulations, where the blade, in the actuator disk with BEM, was divided into 30 elements. The profile are relative to two positions, X/D=1 and X/D=3 downstream from the turbine.

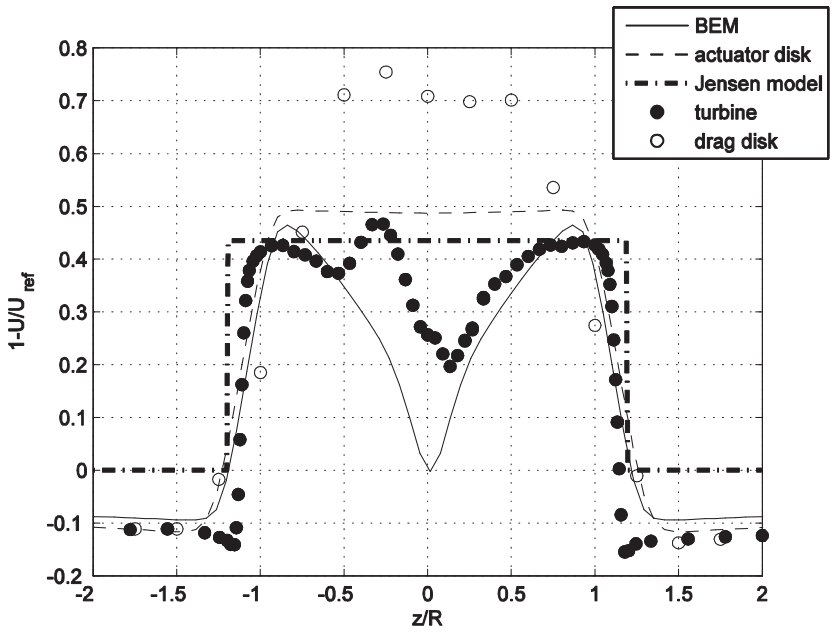

Fig.4.62 Mean velocity profiles along a horizontal line X/D=1, TSR 6, by simple actuator disk, BEM, Jensen model, turbine experimental data and drag disc experimental data

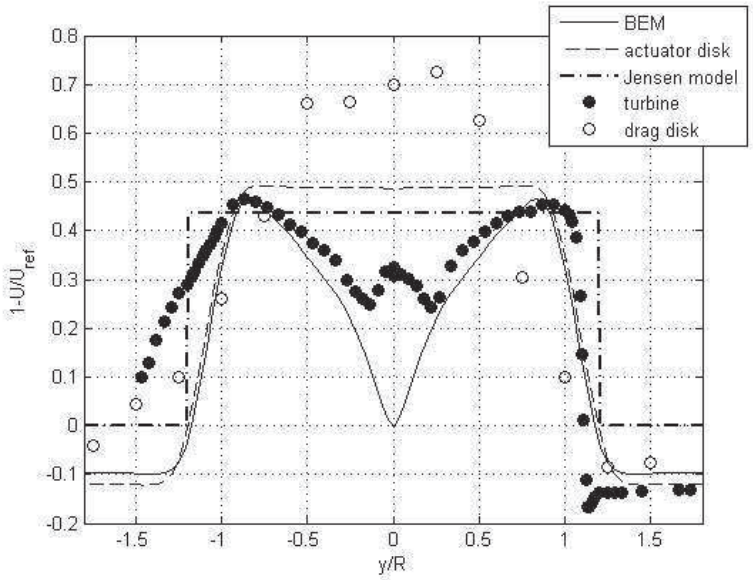

Fig.4.63 **Mean velocity profiles along a vertical line X/D=1, TSR 6, by simple actuator disk, BEM, Jensen model, turbine experimental data and drag disc experimental data**

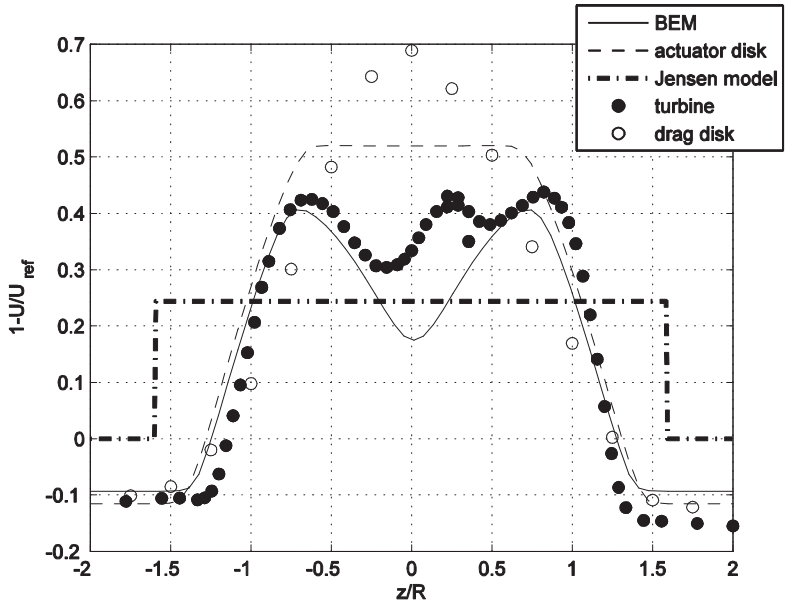

Fig.4.64 **Mean velocity profiles along a horizontal line X/D=3, TSR 6, by simple actuator disk, BEM, Jensen model, turbine experimental data and drag disc experimental data**

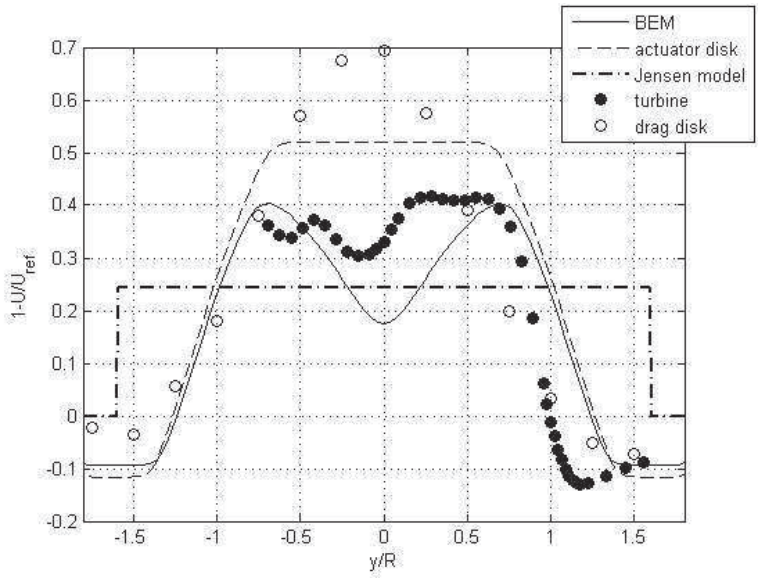

Fig.4.65 Mean velocity profiles along a vertical line X/D=3, TSR 6, by simple actuator disk, BEM, Jensen model, turbine experimental data and drag disc experimental data

From Fig.4.62, Fig.4.63, Fig.4.64, Fig.4.65 we can note that in general both the computational solutions are closer to the turbine. The actuator disc with BEM simulates very well the turbine and the velocity profile is completely different from the drag disc data: the actuator disc with BEM predict a central dip surrounded by two peak in correspondence of the disc edge whereas the drag disc wake has only one central peak. The model predicts a smaller velocity deficit than the turbine. The simple actuator disk overestimates the wake and the correspondence profile are limited by the turbine data and the drag disc data. In Fig.4.63 we can note that the simulations predict a profile close to the ground wall different from the turbine and the drag disc profile whereas turbine and drag disc are characterized by a similar profile in this zone, which is probably due to the tower presence.

The Jensen model is the method that produce the worst results, this was predictable because it is thought to analyse a real wind turbine whereas in my work is used to analyse a model in a wind tunnel. In the Jensen model the α coefficient have to be calibrated with experimental data, so the value used ($\alpha = 0.1$) is quite accurate for a real case and not for a model. Furthermore this model does not consider the blockage effect and do not respect the conservation of the mass: it does not see the flow acceleration around the disk. The Jensen profile is squared because the Jensen model is an analytic model and it has not terms that take account of the velocity profile diffusion.

5 Conclusion

In this thesis the wake behind a wind turbine, modeled by an actuator disk with BEM, was analyzed, both at on-design and off-design conditions. As a general comment, the model results match quite well the experimental data. At TSR=6, while the matching is particularly good for the velocity profiles, the estimated turbulent kinetic energy is twice as low. At on-design condition and for high TSR the agreement between simulations and experiments is better than for low TSR, probably due to errors in the estimation of the stall. The computational model is not able to predict the asymmetry in the experimental wake velocity profiles , which was due to the presence of nacelle and the tower, which were not included in the computational model. Despite the little discrepancies, we can use the actuator disc with BEM to analyzed the turbine wake and it can be a good tool to design a wind farm.

The actuator disc model coupled with a BEM approach is more complex and requests more computational resources than the simple actuator disk. Despite that, the wake predictions are significantly better. When comparing the computations with experimental results from wind tunnel tests, the simple actuator disk is not able to predict the mean velocity of the flow at the center of the wake, while the actuator disk with BEM reproduces the wake more accurately. At off-design conditions, the simple actuator disk model outputs completely wrong results especially for what concerns the mean velocity profiles.

The computations were also compared to the experimental results obtained with a porous disc, used as an experimental static simulator of a wind turbine. The porous disc wake was markedly different from the model turbine wake, being deeper and featuring much higher turbulence levels. While the actuator disc with BEM was in better agreement with the model turbine results, the simple actuator disc outputted velocity profiles which were featuring equally high errors both with respect to the turbine and the drag disc.

The Jensen model, which is still the standard model for wake analysis in industrial environments, was outperformed by both actuator disc models, both for what concerns the agreement with the model turbine and the porous disc. This is due to the rather crude approximations of the Jensen model, especially for what concerns the wake spreading and evolution. Both the Jensen model and the actuator disc require the same input for the rotor simulation (i.e. only the turbine C_T) and are equally crude for what concerns the rotor representation. Nevertheless, using a CFD model to simulate the wake spreading greatly improves the simulation, especially since the reference experiments were performed in a wind tunnel, where the low turbulence levels limit the spreading rate of the wake. As a general comment, the actuator disc with rotation is to be preferred over the Jensen model if the details of the wake want to be resolved.

The performance of the computational models is strictly linked with the accuracy of the input data, like the aerodynamic characteristics of the airfoil and the background wind tunnel turbulence. When experimental aerodynamics characteristics of the airfoil are used, and when the experimental value for the inlet turbulent length scale is employed, the results have a better agreement with the experiments. The turbulent length scale has a strong influence: if we use a relation used to calculate the turbulent length scale in a pipe the results are completely wrong, and the wake recovery is greatly overestimated.

Although the analyzed model has proved to output good result, it can be surely improved in three key areas:

- Mesh refinement
- Including a model for nacelle and tower
- Using Reynolds dependent airfoil characteristics

The mesh used is a simple hexahedral mesh, where the cells have a regular hexahedron shape. The mesh had the same size in the whole computational domain exception made for the disc region, where the mesh is more refined. A possible improvement would be to increase the mesh refinement in the disc area and in the disc wake, to improve the precision in the wake resolution. In order to avoid that a cell is split between two adjacent annular rings, the usage of cells with a curved surface would be beneficial.

The nacelle and the tower could be represented via simple actuator disks, even though the simple actuator disk library should be modified in order to include the empirical law which takes into account momentum theory breakdown.

In the current analysis the aerodynamic characteristics of the airfoil for $Re = 1.2 \cdot 10^5$ were used for all calculations. An important improvement would be to insert the possibility of Reynolds dependent calculation of the airfoil characteristics, in order to take into account the variability of the blade performance at different TSR and for different radiuses of the analyzed blade section.

References

[1] Manwell, J. F., McGowan, J. G. and Rogers, A. L. (2009) Wind Energy Explained: Theory, Design and Application, Second Edition. John Wiley & Sons, Ltd. pp 1-22.

[2] Dahlberg, J.-Å., (2009) Assessment of the Lillgrund Wind Farm: Power Performance Wake Effects, [online report] Vattenfall Vindkraft AB, 6_1 LG Pilot Report.

[3] Krogstad , P.-Å. and Eriksen, P. E. (2012) "Blind test" calculations of the performance and wake development for a model wind turbine. Renewable energy, 50 (2013), pp 325-333.

[4] Manwell, J. F., McGowan, J. G. and Rogers, A. L. (2009) Wind Energy Explained: Theory, Design and Application, Second Edition. John Wiley & Sons, Ltd. pp 91-155.

[5] Burton, T., Sharpe, D., Jenkins, N. and Bossanyi, E. (2001) Wind Energy Handbook. John Wiley & Sons, Ltd. pp 41-77.

[6]Martin O. L. Hansen (2008) Aerodynamics of Wind Turbines, Second Edition. Earthscan. pp 27-40 and pp 45-62.

[7] Martin O. L. Hansen (2008) Aerodynamics of Wind Turbines, Second Edition. Earthscan. pp 53-55.

[8] Versteeg, H. K. and Malalasekera, W. (2007) An Introduction to Computational Fluid Dynamics, the finite volume method, Second Edition. Pearson Education Limited. pp 40-114.

[9] Krogstad , P-Å and Eriksen, P. E. (2012) "Blind test" calculations of the performance and wake development for a model wind turbine. Renewable energy, 50 (2013), pp 325-333.

[10]Krogstad , P.-Å. and Eriksen, P. E. (2012) "Blind test" calculations of the performance and wake development for a model wind turbine. Renewable energy, 50 (2013), pp 325-333.

[11] Sarmast, S. and Mikkelsen, R. F. The experimental results of the NREL S826 Airfoils at low Reynolds numbers. Linné Flow Centre, KTH Mechanics, SE-100 44 Stockholm, Sweden. DTU wind energy, Lyngby, Denmark. Internal report.

[12] Sarmast, S. and Mikkelsen, R. F. The experimental results of the NREL S826 Airfoils at low Reynolds numbers. Linné Flow Centre, KTH Mechanics, SE-100 44 Stockholm, Sweden. DTU wind energy, Lyngby, Denmark. Internal report.

[13] Versteeg, H. K. and Malalasekera, W. (2007) An Introduction to Computational Fluid Dynamics, the finite volume method, Second Edition. Pearson Education Limited.

[14] Krogstad , P.-Å. and Sætran, L. Invitation to the 2013 "Blind test 3" Workshop Two in-line wind turbines with spanwise offset. Department of Energy and Process Engineering, NTNU, Trondheim, Norway.

[15] Pierella, F., Sætran, L. (2010) Effect of initial conditions on flow past grids of finite extension. 17th Australasian Fluid Mechanics Conference Auckland, New Zealand, 5-9 December 2010.

[16] Jensen, N. O. (1983) A Note on Wind Generator Interaction. Risø-M-2411

[17] Choi, J. and Sham, M. (2013) Advancement of Jensen (Park) model. Proceedings of the EWEA 2013 Conference, Wien.

[18] Krogstad , P.-Å. and Eriksen, P. E. (2012) "Blind test" calculations of the performance and wake development for a model wind turbine. Renewable energy, 50 (2013), pp 325-333.

[19] Krogstad , P.-Å. and Eriksen, P. E. (2012) "Blind test" calculations of the performance and wake development for a model wind turbine. Renewable energy, 50 (2013), pp 325-333.

[20] Krogstad, P.-Å. and Lund, J A (2012) An experimental and numerical study of the performance of a model turbine. Wind Energy 2012; 15:443-457.